Emissions, diurnal variability and modelling of biogenic volatile organic compounds

ABHISHEK KUMAR MISHRA

A thesis submitted for the partial fulfillment of

the degree of Doctor of Philosophy

Department of Earth and Environmental Sciences

Indian Institute of Science Education and Research Mohali

Knowledge city, Sector 81, SAS Nagar, Manauli PO, Mohali 140306, Punjab, India.

September 2020

Dedicated

to

my parents

Declaration

The work presented in this thesis has been carried out by me under the guidance of Dr. Vinayak Sinha at the Indian Institute of Science Education and Research Mohali. This work has not been submitted in part or in full for a degree, a diploma, or a fellowship to any other university or institute. Whenever contributions of others are involved, every effort is made to indicate this clearly, with due acknowledgement of collaborative research and discussions. This thesis is a bona fide record of original work done by me and all sources listed within have been detailed in the bibliography.

Abhishek Kumar Mishra

In my capacity as the supervisor of the candidate's thesis work, I certify that the above statements by the candidate are true to the best of my knowledge.

Dr. Vinayak Sinha

Acknowledgement

I take this opportunity to express my deep respect and gratitude to my supervisor Dr. Vinayak Sinha: - a great teacher and mentor, who has been an inspiration to me ever since I have known him. I thank him for his unwavering guidance, support, supervision and constant encouragement. He has always motivated me to give one's best effort in any work. Without his guidance this dissertation would not have been possible. I also thank him for giving me an opportunity to work with the best resources and access to best training in the field of atmospheric science.

I express my sincere gratitude to Dr. Baerbel Sinha for her constant motivation, invaluable suggestions, mentoring and support during different stages of this thesis work. I am also thankful to my monitoring committee members Dr. Baerbel Sinha and Dr. N.G. Prasad for their insightful suggestions and motivation.

I express my sincere gratitude to Dr. Rajesh Kumar and Dr. Mary Barth from National Center for Atmospheric Research (NCAR, Boulder) for helping setting up WRF-Chem model and gratefully providing access to Cheyenne supercomputing facilities at NCAR. I specially thank Dr. Rajesh Kumar for his invaluable suggestions, mentoring and support during different stages of this thesis work. I express my sincere thanks to Dr. Alex Guenther from the University of California, Irvine for sharing his invaluable insights and discussions on MEGAN biogenic model. I also express my sincere thanks to Dr. Thomas Wagner from Max Planck Institute for Chemistry, Mainz and Dr. Sachin Ghude from Indian Institute of Tropical Meteorology, Pune for their support and guidance during CINDI-II and Delhi winter fog campaigns.

I thank all my present and past group members from Atmospheric Chemistry and Emissions Group and Aerosol Research Group at IISER Mohali- Harshita, Vinod, Gaurav, Praphulla, Haseeb, Ashish, Pooja, Chinmoy, Saryu, Pallavi and Savita for their constant support and help. I would like to express my gratitude to Vinod, Praphulla and Chinmoy to help me learnt the basic concepts about different instrumental techniques at our group. I would sincerely thank Haseeb, Harshita and Ashish for being such fantastic colleagues during different group experiments and source samplings where I got an opportunity to learn a lot about field experimental work. Talking about field experimental work I find myself extremely lucky to have been a part of Delhi winter fog

campaign where I learned a lot from the winter fog team about challenges of field campaigns and acquiring measurements in remote locations. I specially thank Vinod for sharing his insights on data analysis and helping me a lot in understanding programming and data analysis. I also thank him for sharing his insights and help me learnt the basic concepts on DOAS measurement technique at Mohali and Cabauw during CINDI-II campaign. I would also like to thank final year thesis students from our lab: Bharti, Abhishek, Adarsh and others for all the support and help. I would like to say that I have thoroughly enjoyed my academic and research activities at our group.

I would also like to thank Harshita, Vinod, Gaurav, Praphulla, Haseeb, Ashish, Anup, Satyam, Pooja, Ritika, Arnob, Sudhanshu, Mayank for providing company and making life enjoyable in and out of the campus. They have been like a family away from home. I am grateful to my friends Aakash Gupta, Merul Fauzdar, Kishore Kushwaha, Anurag Sinha for their love and support during my journey.

I would like to place on record, my gratitude to IISER Mohali (IISERM) and the Ministry of Human Resource Development (MHRD), Government of India for my Junior and Senior Research fellowships. I also thank Atmospheric Composition and the Asian Monsoon (ACAM), National Center for Atmospheric Research, Boulder (NCAR), Max Plank Institute for Chemistry, Mainz (MPIC) and IISERM Travel Support for funding my travel to international and national conferences. I also express thanks to the administrative, library, hostel, mess, canteen, house-keeping, maintenance, health center and security staff of IISER Mohali who made my stay here comfortable and safe.

I express my gratitude to my grandfather, late Shri. Chandra Bhushan Mishra and my grandmother late Smt. Katyani Devi for shaping my personality at a young age. They have always been an influence in various spheres of my life. If they were alive today, they would have been happy to see the path I pursued. Finally, and also most importantly, I would like to thank my mother Mrs. Usha Kiran Mishra, my father Dr. Shri Pal Mishra, my brother Amit Kumar and my Sister in Law Vandana Mishra. I consider myself to be extremely fortunate to have born to such great parents and family. I thank them from the bottom of my heart, for letting me pursue my dreams and patiently supporting me in my endeavors all these years. I express my thanks to my cute loving nephews Kartikey and Avighna who are my biggest motivation in life.

Abhishek Mishra

Synopsis

Thesis Title: Emissions, diurnal variability and modelling of biogenic volatile organic compounds

Candidate: Mr. Abhishek Kumar Mishra

Biogenic volatile organic compounds (BVOCs) are emitted from vegetation and play a pivotal role in atmospheric chemistry. Isoprene which is mainly emitted from trees and shrubs as a by-product of photosynthesis is the major contributor to the global biogenic budget. Once released into the atmosphere isoprene rapidly reacts with hydroxyl radicals (OH) forming oxygenated VOCs such as methyl vinyl ketone, methacrolein as well as formaldehyde and acetaldehyde in varying amounts. Formaldehyde and acetaldehyde are mainly formed photochemically by oxidation of other precursor hydrocarbons such as alkenes and alkanes. These oxygenated VOCs also play an important role in determining oxidizing capacity of troposphere.

The production of these oxygenated VOCs from isoprene oxidation proceeds through differing mechanisms in high nitrogen oxides ($NO_x = NO + NO_2$) regime (urban environment) and low NOx regime (forested environment). Additionally, in an urban environment isoprene oxidation can further lead to formation of ground level ozone due to catalytic action of NOx. While in a pristine environment it can lead to recycling of OH radical and sustaining the oxidation capacity. Additionally, isoprene also acts as a major precursor of peroxyacetyl nitrate (PAN) and organic aerosols, which makes it very important from the stand point of both air quality and Earth's climate.

Isoprene is produced within the chloroplast of plant cell by the action of isoprene synthesase enzyme (IpS) on the substrate dimethylallyl phosphate (DMAPP) along the mevalonate metabolic pathway (MEP pathway). It is released in response to heat stress or drought and is often considered as a metabolite relief valve contributing to the thermoregulation in plants. The experimental evidence from different lab and field based studies conducted over the past three decades has helped establish that isoprene emission rates are higher on sunny and warmer days in comparison to colder and sunny days. The experiments have also established that isoprene

emission is also a strong function of past 24-hour temperature, the isoprene emissions begin at approximately 285 K and start to level off in the range of 310-320 K due to degradation of enzymatic processes and stomatal closure. Both the above factors are present in abundance in the rainforest and likewise they contribute more than 75% of global isoprene emissions. Therefore, tropical rainforests have been the hotspot of ground based measurements of isoprene and its oxidation products. These studies have helped identify and evaluate the lab based estimates of isoprene oxidation yields. The laboratory studies have demonstrated methyl vinyl ketone, methacrolein yield of around 0.1 under low NO_x conditions (< 70 ppt NO) and under high NO_x conditions its yield can range from 0.5 to 0.8. The ratio of methyl vinyl ketone, methacrolein to isoprene can be used as a proxy to investigate isoprene oxidation and is reported to exhibit a value close to 0.5 in forested environments in Amazon basin. While values close to 0.45 has been reported from southeastern USA and close to ~ 1 in urban centers of China.

The north-west Indo-Gangetic Plain is the agricultural “bread basket” of South Asia and is one of the most under-studied regions of the world in terms of atmospheric composition and in particular biogenic emissions. Till date only a few studies have reported measurements of isoprene and its oxidation products in summer and in winter season. These periods are also associated with other dominant anthropogenic emission sources for example crop residue burning (May, September to November), wildfire (March-June) landfill fire (March-June) and winter season is associated with fog and cooler conditions which are not conducive to biogenic activity. In addition, during the harsh summer season isoprene temperature can reach up to 40-45 ℃, beyond which enzymatic processes and stomatal closure occurs which are not favorable to biogenic emission.

The monsoon season over the region provides a unique window with maximum signal to noise ratio to study the biogenic emissions and land atmosphere-interactions. During this season vegetation throughout the region is not moisture limited while many anthropogenic fire sources such as crop residue burning and forest fires are absent. Further in monsoon, Indo-Gangetic Plain is a major rice growing region of the world and daytime hourly ozone can frequently exceed phytotoxic dose of 40 ppb O_3 while the strong convective activity causes surface emissions to be transported to upper atmosphere. Therefore, during this season biogenic emissions can significantly impact the remote upper atmosphere, climate and ozone affecting, rice yields.

The farmers of N.W IGP practice mixed Agroforestry due to which the croplands have large swathes of poplar and eucalyptus growing at the periphery of croplands, which are strong isoprene emitters. Trees besides biogenic emissions also impact the micrometeorology by modulating the surface sensible and latent heat flux through evaporative cooling.

To understand this complex interplay of biogenic emissions, micrometeorology and atmospheric chemistry this study for the first time utilizes ground based measurements of isoprene and its oxidation products from a sub-urban site in the foothills of the Himalayas during the monsoon season. This measurement site located in IISER Mohali (30.667° N–76.729° E, 310 m a.s.l) and is best suited to investigate the biogenic activity due to its semi-forest and semi-urban nature. To the north east of the site, lies urban agglomerates such as Chandigarh and Panchkula city, whereas the north-west fetch region consists of mainly rural and agricultural land with Agroforestry. To further investigate the impact of Agroforestry on regional atmospheric chemistry and study the land atmosphere-interactions during monsoon season. This study utilizes weather research and forecasting model coupled with chemistry (WRF-Chem) model.

The WRF-Chem model is coupled online with the Model of Emissions of Gases and Aerosol from Nature (MEGAN) model to compute regional biogenic emission. The current version of MEGAN model coupled with WRF-Chem uses an approach where each of the grid cell is divided into different PFTs (Broadleaf, Needleleaf, Shrubs and Herbs) and non-vegetative (barren) surface. In addition to the PFTs MEGAN also has defined global gridded dataset of leaf area index (LAI) and gridded emission factor (EF) to account for the geographical variability and season. The base emissions or EF are modulated utilizing different emission activity functions which account for variability in environmental conditions (temperature sensitivity, light sensitivity etc.). The base emission factor for different PFTs have been estimated through field studies and ground based measurements in different ecosystems while the activity functions have been developed from laboratory based experiments. As discussed above the WRF-Chem model utilizes MEGAN model for computing biogenic emissions, while the processes associated with land atmosphere interactions are simulated using Noah land surface model which has its own vegetation dataset.

In my thesis work, I have analyzed first monsoon time dataset of isoprene, methyl vinyl ketone, methacrolein, formaldehyde, and acetaldehyde ground based measurements from India. Next, I have evaluated the current representation of biogenic emissions and associated land use land cover

data in major intensively farmed agricultural regions of the globe. Next, I have improved the representation of vegetation in WRF-Chem coupled MEGAN model over N.W IGP which has been estimated using latest high resolution satellite imagery from MODIS, Google Earth and Landsat. Finally, the improved model setup has been used to investigate regional atmospheric chemistry and the land atmosphere-interactions during monsoon season. Specifically, the impact of Agroforestry on regional atmospheric Chemistry and micrometeorology. Next I, present overview of different chapters in my thesis.

CHAPTER-1

In the first chapter of my thesis, I present an introduction of BVOCs, their importance and global budget in the atmosphere. This is followed with discussion on importance of isoprene which dominates the global budget of BVOCs. Next, I have discussed about the significance of daytime isoprene oxidation and how the formation of oxygenated VOCs such as methyl vinyl ketone, methacrolein, formaldehyde and acetaldehyde proceeds through differing mechanisms in urban and pristine environments. Isoprene and its oxygenated products play an important role in determining oxidizing capacity of troposphere and very important from the stand point of both air quality and Earth's climate. Apart from isoprene oxidation oxygenated organic compounds such as acetaldehyde and formaldehyde have strong photochemical sources and are formed by oxidation of other precursor hydrocarbons. In the case of acetaldehyde apart from photoxidation, direct biogenic emissions from poplar and mosses and lichens have also been reported. Next, a general introduction for modelling biogenic emissions and land –atmosphere interactions are presented. The chapter ends stating the motivation for my thesis work which was driven by the following scientific questions:

1- What is the ambient variability, diel profile of isoprene, formaldehyde, methyl vinyl ketone, methacrolein and acetaldehyde during monsoon season?
2- What are the major daytime sources of these compounds in the monsoon season when biogenic sources are strongest relative to other sources over the north-west Indo-Gangetic Plain?
3- What is the configuration of weather research and forecasting model coupled with chemistry and MEGAN model and how well does the model represents the ground level isoprene during the monsoon season over north-west Indo-Gangetic Plain presently?

4- What is the degree of underestimation of cropland trees in some major Agroforestry intensive regions of the world including north-west Indo-Gangetic Plain?
5- How do the missing cropland trees affect atmospheric chemistry and micrometeorology of an agricultural region like north-west Indo-Gangetic Plain?
6- What is the extent to which trees in croplands may help to reduce crop yield losses due to heat stress and ozone pollution?
7- Can expanding Agroforestry tree cover result in further crop yield gain and climate co-benefits in future?

The scientific questions were addressed using ground based observations high sensitivity proton transfer reaction mass spectrometry (PTR-MS) technique for VOC measurements, high-resolution land use land cover satellite data along with weather research and forecasting model coupled with chemistry (WRF-Chem) and Model of Emissions of Gases and Aerosol from Nature (MEGAN) model.

CHAPTER 2

In the second chapter, I report the measurements for isoprene, formaldehyde, methyl vinyl ketone, methacrolein and acetaldehyde performed in July, August and September months at a sub-urban site in north-west Indo-Gangetic Plain. In this study, I demonstrate that during the monsoon season biogenic emissions were the major source of isoprene with photo-oxidation of isoprene as the major source of methyl vinyl ketone, methacrolein. The daytime observed average ambient mixing ratios for isoprene during the monsoon season were comparable to mixing ratios observed over tropical forests (eg. Amazon rainforest, Borneo rainforest.). Additionally, formaldehyde and acetaldehyde have strong photo-chemical sources from the oxidation of hydrocarbons, including isoprene. Agroforestry cultivation of poplar, eucalyptus (high isoprene emitting trees), over the north-west Indo-Gangetic Plain were found to be the likely sources.

CHAPTER 3

In the third chapter, I configured WRF-Chem coupled MEGAN model over South Asia to study three dimensional (3D) simulations of meteorology, atmospheric chemistry and biogenic emissions over north-west Indo-Gangetic Plain during monsoon season. Modelled

isoprene showed under-prediction which was due to the missing Agroforestry trees in the croplands.

CHAPTER-4

In the fourth chapter, I estimated fractional tree cover for different types of croplands on different continents. In this study, I demonstrate that the tree cover over intensely farmed regions in Asia, Australia and South America is significantly underestimated (e.g. only 1-3% tree cover over North-India) by the current chemistry-climate models. Next, I included the actual tree cover (~10%) over the north-west Indo Gangetic Plain in WRF-Chem model. The new model setup improved agreement between the modelled and measured temperature, boundary layer height, surface ozone which were earlier overestimated. The new model setup also improved agreement between measured and modelled isoprene and its oxidation products which were earlier underestimated. In this study I found that the surface latent heat flux alone increases by 100-300% while surface sensible heat flux reduces by 50-100%, leading to a reduction in daytime boundary layer height by 200-400 m which modulates air pollution. In this study, I also show that the trees in croplands mitigate peak daytime temperatures and ozone which improves rice production by 10 -20%. Finally, I demonstrated that expanding Agroforestry practices to 50% of the cropland area could result in up to 40% yield gain regionally. Therefore, future climate mitigation and food security efforts should consider stakeholder participation for increased cropland Agroforestry because of its beneficial effects.

CHAPTER-5

In the fifth chapter, I provide the main conclusions from my thesis with an overview of future outlook from this study.

The current study focused primarily on improving the representation of vegetation in MEGAN module and Noah land surface module during the monsoon season as inconsistency was found in the vegetation data of the model. However, the current WRF-Chem set up doesn't take into account the vegetation data while computing the dry deposition of different trace gases and VOCs which can be a limitation. It is worth mentioning here that the representation of vegetation data in the current WRF-Chem modelling system is quite tricky and sometimes difficult to follow. There are three different modules which are simulating different processes are using three different

input vegetation datasets. The Noah land surface model and MEGAN model, both have their own land use dataset, similarly the biomass burning emission module has its own. In my thesis I have made the representation of vegetation data in the Noah land surface model complement with that of MEGAN model as per the latest high resolution satellite imagery over South Asia. These changes will also have to be incorporated over other parts of the globe and also to the biomass burning inventory. So that in future only a single dataset can be used seamlessly across different modules.

In future studies improved model setup described in chapter 4 should be implemented over other parts of the globe which were identified for missing trees in croplands. The improved setup should also validate the representation of other BVOCs from the model (eg. monoterpenes). Additionally, the improved model set up can also focus on high resolution simulations over urban areas to accurately estimate heat stress and air pollution over cities. It can also be implemented for studying urban heat island effect and coming up with what if scenarios for park cooling effects that is changing an urban center with vegetation just like the 50% Agroforestry study discussed in chapter 4.

The key messages from all the chapters can be visualized through the graphical abstract below.

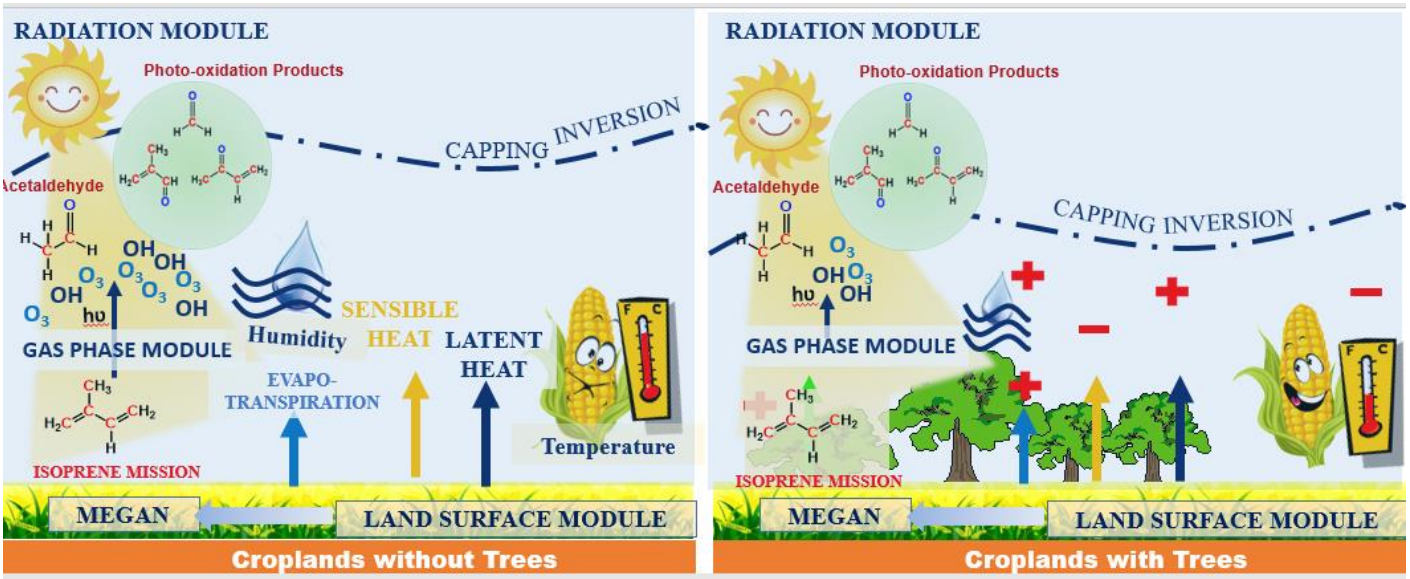

Table of Contents

 # Page

List of Publications

- ***Mishra A.K****, Sinha V.* Emission drivers and variability of ambient isoprene, formaldehyde and acetaldehyde in north-west India during monsoon season. Environmental Pollution 2020; 267: 115538.

- ***Mishra A.K****, Sinha B, Kumar R, Barth M, Hakkim H, Kumar V, Kumar A., Datta S., Guenther A., and Sinha V.* Cropland trees need to be included for accurate model simulations of land-atmosphere heat fluxes, temperature, boundary layer height, and ozone. Science of The Total Environment 2021; 751: 141728.
- *Kumar V., Beirle S., Dörner S.,* ***Mishra A.K.,*** *Donner S., Wang Y., Sinha V., and Wagner T.***:** Long term MAX-DOAS measurements of NO_2, HCHO and aerosols and evaluation of corresponding satellite data products over Mohali in the Indo-Gangetic plain, Atmos. Chem. Phys. Discuss (Under review, 2020)
- *Kreher, K., Roozendael, M. V., Hendrick,.L., Donner, S., Drosoglou, T., Fayt, C., Finkenzeller, H., Garcia-Nieto, D., Gielen, C., Gómez-Martín, L., Hao, N., Herman, J. R., Hermans, C., Hoque, S., Irie, H., Jin, J., Johnston, P., Butt, J. K., Khokhar, F., Koenig, T. K., Kuhn, J., Kumar, V., Lampel, J., Liu, C., Ma, J., Merlaud, A.,* ***Mishra, A. K.****, Müller, M., Navarro-Comas, M., Ostendorf, M.,Pazmino, A., Peters, E., Pinardi, G., Pinharanda, M., Piters, A., Platt, U., Postylyakov, O., Prados-Roman, C., Puentedura, O., Querel, R., Saiz-Lopez, A., Schönhardt, A., Schreier, S. F., Seyler, A., Sinha, V.****,*** *Spinei, E., Strong, K., Tack, Tian, X., Tiefengraber, M., Tirpitz, J., Gent J. V., Volkameri, and Zhao, X.,* Intercomparison of NO_2, O_4, O_3 and HCHO slant column measurements by MAX-DOAS and zenith-sky UV-Visible spectrometers during the CINDI-2 campaign, Atmos. Meas. Tech. 13, 2169–2208, 2020.
- *Hakkim H, Sinha V, Chandra BP, Kumar A,* ***Mishra A.K****, Sinha B, Sharma, G., Pawar, H., Sohpaul, B., Ghude, S. D., Pithani, P., Kulkarni, R., Jenamani, R. K., Rajeevan,* M Volatile organic compound measurements point to fog-induced biomass burning feedback to air quality in the megacity of Delhi. Science of The Total Environment 2019; 689: 295-304.
- *Chandra, B. P., Sinha, V., Hakkim, H., Kumar, A., Pawar, H.,* ***Mishra, A. K.****, Sharma, G., Pallavi, Garg, S., Ghude, S. D., Chate, D. M, Pithani, P., Kulkarni, R., Jenamani, R. K., and Rajeevan, M.,* Odd-even traffic rule implementation during winter 2016 in Delhi did not reduce traffic emissions of VOCs, carbon dioxide, methane and carbon monoxide, Current Science, 114, 6, 1318-1325, 2018.
- *Ghude, S. D., Bhat, G. S., Prabhakaran, T., Jenamani, R. K., Chate, D. M., Safai, P. D., Karipot, A. K., Konwar M., Pithani, P., Sinha, V., Rao, P. S. P., Dixit, S. A., Tiwari, S., Todekar, K., Varpe, S., Srivastava, A. K., Bisht, D. S., Murugavel, P., Ali, K., Mina, U., Dharua, M., Jaya Rao, Y., Padmakumari, B., Hazra, A., Nigam, N., Shende, U., Lal, D. M., Chandra, B. P.,* ***Mishra, A. K.****, Kumar, A., Hakkim, H., Pawar, H., Acharja, P., Kulkarni, R., Subharthi, C., Balaji, B., Varghese, M., Bera, S. and Rajeevan, M.,* Winter fog experiment over the Indo-Gangetic plains of India, Current Science, vol. 112, no. 4, 2017.

Chapter: 1

Introduction

1.1 Biogenic volatile organic compounds: Importance of biogenic emissions and trees for local microclimate

Biogenic volatile organic compounds (BVOCs) are defined as a family of volatile organic compounds (VOCs) emitted from a variety of sources in the terrestrial ecosystem. They account for more than 90% of total VOC emissions (Goldstein and Galbally, 2007; Palmer et al., 2006) and play a significant role in atmospheric chemistry. These terrestrial sources include emissions from flowers, stems, trunks, soil microbes etc. nonetheless total global biogenic emission is mainly dominated from foliage which is estimated to be 815-1530 Tg y^{-1} (Baghi et al., 2012; Goldstein and Galbally, 2007; Guenther et al., 2012).

These terrestrial ecosystems release thousands of BVOCs showing a strong chemical diversity (Knudsen et al., 2006) but out of these compounds, only a few are emitted at such emission rates which can impact atmospheric composition (Guenther et al., 2012). These suites of chemical compounds emitted from terrestrial ecosystem include terpenoid compounds (Rasmussen, 1972), methanol (MacDonald and Fall, 1993b), acetone (Jacob et al., 2002), acetaldehyde (Jardine et al., 2009), formaldehyde (DiGangi et al., 2011), ethanol and organic acids (Dudareva et al., 2013), alkanes (Kirstine et al., 1998), organic halides (Khan et al., 2011) and organic sulfur compounds (Bates et al., 1992).

The terpenoid compounds dominate the total BVOC budget and can be further classified into different groups as hemiterpenoids (C-5 species), monoterpenoids (C-10 species) sesquiterpenoides (C-15 species), homoterpenes (C-11 and C-16 species) and diterpenoids (C-20 species). Isoprene which is a hemiterpenoid is the major contributor to the global BVOC budget (Guenther et al., 2006; Guenther et al., 2012), the factors controlling its emission process will be discussed in section 1.1.1.

Atmospheric oxidation dominates the global budget of methanol and acetone. In addition, methanol and acetaldehyde are also emitted from young expanding leaves and conifer buds

respectively (Jacob et al., 2002, MacDonald and Fall, 1993b, Macdonald and Fall, 1993a). Similarly, for acetaldehyde emissions from terrestrial ecosystem source amounts to 11 % of the global budget (Millet et al., 2010) mainly from alcoholic fermentation in leaves and roots of plants under anoxic conditions (Kesselmeier and Staudt, 1999). Formaldehyde which is mainly formed by oxidation of precursor hydrocarbons such as alkenes and alkanes (Fortems-Cheiney et al., 2012; Millet et al., 2010) also have been reported to be emitted from various tree species (Kesselmeier, 2001).

The BVOCs once emitted into the lower atmosphere undergo transport and mixing in the planetary boundary layer. Further, they undergo photochemical oxidation along with the other removal processes such as surface deposition (vegetation/aerosol) or washout in rainwater (wet deposition) (Seinfeld and Pandis, (1998)). During the daytime, the BVOCs undergo photochemical oxidation by atmospheric oxidants such as hydroxyl radicals (Park et al., 2013). The daytime reactions with hydroxyl radical (OH) represent the dominant sink for the BVOCs (Lelieveld et al., 2016). Additionally, reactions with ozone, photolysis and reactions with nitrate radical (NO_3) during nighttime also act as sinks for BVOCs (Atkinson and Arey, 2003). The photo-oxidized products/intermediates can also get transported (advection and convection) due to the meteorological noise/wind.

The biogenic emissions in urban areas enhance tropospheric ozone formation also known as ‘bad ozone’ when present more than few tens of ppb it is known to harm human health, air quality, and health of crops (Haagen-Smit, 1952; Sinha et al., 2015). Besides, biogenic emissions also contribute to the formation of secondary organic aerosols (Xavier et al., 2019), which is very important from the standpoint of urban air pollution and climate.

Trees are the strongest source of BVOCs (Guenther et al., 2006) and are therefore very important from an atmospheric chemistry perspective. Besides, trees also impact the micrometeorology by modulating the surface sensible and latent heat flux through evaporative cooling. Due to the evapotranspiration cooling and reduction in sensible heat, they reduce the environmental temperature which can have multiple benefits (Campi et al., 2009, Nature Clim. Change., 2019, Wang et al., 2015). For example, in croplands, it can lead to a reduction in heat stress enhancing crop productivity a practice known as Agroforestry. Agroforestry is a collective nomenclature given to land-use systems and practices where woody perennials (eg. Poplar, Eucalyptus, Bamboos

etc.) are planted on the same land units on which crops are growing with a particular temporal sequence or spatial arrangement.

In the next sections, I discuss the factors which influence BVOC emissions with the main focus on the emission of biogenic isoprene. This would be followed up with a discussion on the impact of BVOCs on tropospheric chemistry.

1.1.1 Causes and environmental factors that influence biogenic isoprene emission

The formation and emission of BVOCs is mainly dependent on physiological, biochemical and physiochemical processes inside plants which are a function of environmental conditions (Sharkey and Singsaas, 1995).

As discussed in the previous section isoprene emissions dominate the total global BVOC budget. Its emission was first reported from plants that were being grown in the greenhouse environment in 1957 from a team of researchers who were analyzing the emissions of volatile products from different tree species eg. Poplar (*Populus nigra L.*), Acacia (*Robina pseudo acacia L.*) etc. The research team was led by Guivi Sanadze who was the first one to report and identify isoprene emission characterized as temperature and light-dependent process (Sanadze, 1957; Sanadze, 2004). The schematic in Figure 1.1 shows the steps of isoprene formation within the plant. Isoprene is produced within the chloroplast of plant cells by the action of isoprene synthesase enzyme (IpS) on the substrate dimethylallyl phosphate (DMAPP) along the mevalonate metabolic pathway (MEP pathway) (Sharkey et al., 2008) which makes around 2% of total photosynthetic activity.

The experimental evidence of the past three decades has indicated that several physical and biological factors modify the capacity of plants to emit isoprene (Guenther et al., 2006). The main factors influencing the isoprene emissions include leaf temperature, incident photosynthetic photon flux density (PPFD) (Guenther et al., 2006). These factors influence isoprene emissions over time scales of seconds to weeks (Monson and Holland, 2001; Sharkey, 2001). A leaf's ability to emit isoprene is influenced by numerous factors, leaf phenology plays a very important role. Generally, young leaves do not emit isoprene, the emission is maximum in mature leaves while it reduces in case of senescence (Dani et al., 2014; Harley et al., 1994). Soil moisture also affects the isoprene emission capacity (Pegoraro et al., 2004), additionally, there is growing evidence that

increasing carbon dioxide levels and ozone episodes may also affect isoprene emission capacity (Velikova et al., 2008).

Increasing carbon dioxide levels and ozone episodes may affect isoprene emission capacity. The affect has been discussed in following points:

- Sensitivity to carbon dioxide levels: Some chamber experiments have demonstrated that when grown in environmentally controlled chambers *Populus deltoides* (A high isoprene emitter) showed a 30–40% reduction in isoprene emission rate when grown at 800 ppmv CO_2, compared to 400 ppmv CO_2. Similarly, *Populus tremuloides* exhibited a 33% reduction when grown at 1200 ppmv CO_2, compared with 600 ppmv CO_2. Using insights developed from similar experiments discussed above, empirical models have been developed which has been incorporated into Community Atmospheric Model-Community Land Model (CAM-CLM) (Heald et al., 2009). By accounting CO_2 inhibition shows little impact on predictions of present-day global isoprene emission (increase from 508 to 523 Tg Cyr-1) while the projected global isoprene emissions in 2100 showed a drop from 696 to 479 Tg Cyr-1 when this effect was included. The future projections suggest a compensatory balance between effect of temperature and CO_2 (Heald et al., 2009).
- Sensitivity to ozone pollution levels: To understand the effect of ozone on isoprene emission, chamber studies are conducted under controlled laboratory conditions. In these experiments different plant species are exposed to different scenarios like exposed to clean air and fumigated with ozone rich air (environmentally relevant ozone concentration levels) (Tani et al., 2017). The above chamber experiment was conducted for two *Quercus* species wherein the isoprene emission rate and DMAPP content were significantly decreased by enriched ozone. This suggests that the reduction in the production of substrate DMAPP is a cause of the decreased isoprene emission.

Plants release isoprene to protect the leaves against thermal stress as isoprene emission contributes to the thermoregulation by plants. Isoprene emission can be related to as metabolic relief valve which releases phosphate stuck in DMAPP as protection from ozone and heat damage (Sharkey and Singsaas, 1995; Sharkey et al., 2008; Vickers et al., 2009).

The three graphs in Figure 1.1 elucidate the relationship between isoprene and environmental conditions which have been developed with different field and modelling studies (Guenther et al., 1996; Guenther et al., 2006; Guenther et al., 1991; Guenther et al., 1993; Lamb et al., 1996). The substrate concentration (DMAPP) directly affects isoprene emissions by influencing the rate of reaction of the isoprene synthesase enzyme on the substrate. Additionally, isoprene emission rates have been observed to be higher on sunny (higher PPFD) and warmer days in comparison to colder and sunny days (Petron et al., 2001). Isoprene emission is also a strong function of past 24-hour temperature (directly proportional), the isoprene emissions begin at approximately 285 K and start to level off in the range of 310-320 K (Guenther et al., 2006) depending on the past 24-hour temperature. In the next section, I discuss the role of BVOCs on tropospheric chemistry with the main focus on the chemistry of isoprene, acetaldehyde, and formaldehyde.

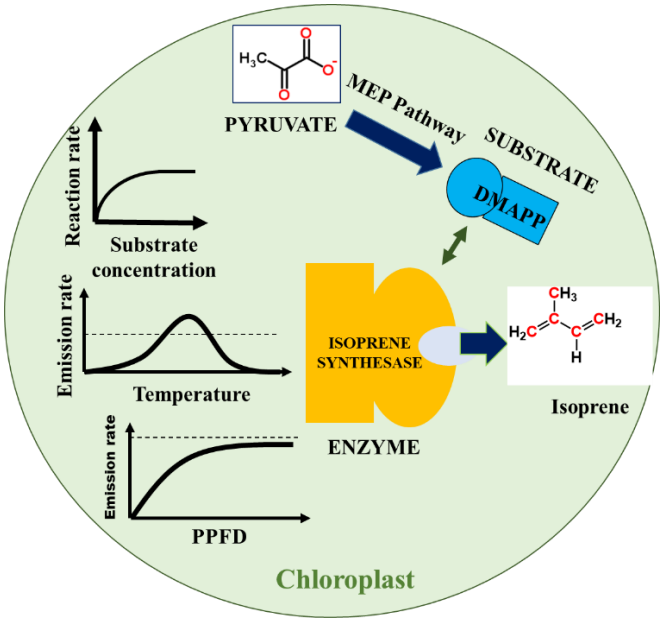

Figure 1.1 Schematic showing the pathway for isoprene synthesis in plants and factors controlling it. Figure was created by author using Office 2016.

1.2 Importance of isoprene, acetaldehyde and formaldehyde in atmosphere

The quantitative estimation of global BVOC emissions to better understand implications on atmospheric composition started with Went's (Went, 1960) pioneering work along with (Rasmussen, 1970) in which enclosure based measurements of monoterpenes from a single plant species were used to estimate the global biogenic emission. Although the global estimates were off by a factor of three which was later accurately estimated by using the same enclosure based measurements coupled with accurate land use data for different ecosystems (Guenther et al., 1995; Lamb et al., 1996). One of the main challenges associated with the enclosures based studies is to access all the mature parts of a canopy to quantify the canopy level flux. Therefore, a more recent estimation of canopy flux was performed using micrometeorology and eddy flux technique (Misztal et al., 2011).

Over the past few decades, different ground-based measurements have been performed in types of different ecosystems to better understand and quantify the magnitude, diel and seasonal patterns for BVOCs (Eerdekens et al., 2009; Kuhn et al., 2007; Lamb et al., 1996; Langford et al., 2010; Rinne et al., 2002; Winters et al., 2009). These pioneering studies have helped identify tropical forested areas as the major biogenic source along with identifying the hardwood vegetation trees namely eucalyptus, poplar, oaks as the most dominant source (Finlayson-Pitts and Pitts, 1997). Currently, the total BVOC budget estimated by coupling the ground-based measurements with global atmospheric chemistry models comprises of ~50% isoprene, 11% monoterpenes, 22.5 % other reactive VOCs (eg. Acetaldehyde, Formaldehyde) and 22.5 % other VOCs (eg. Methanol, and acetone) (Eerdekens et al., 2009). Therefore, next I discuss the importance of isoprene, acetaldehyde, and formaldehyde on atmospheric chemistry.

Isoprene dominates the total global budget of biogenic emissions (400-600 Tg y^{-1}) (Guenther et al., 2006) and is emitted from trees as a by-product of photosynthesis. Plants being a natural system exhibit a circadian rhythm (Hewitt et al., 2011) which gives a diurnal pattern to the observed isoprene concentration. The isoprene emissions begin in the morning after the sunrise, peaks around the noontime and finally ceases at sunset. Different studies have shown a strong variability in the observed average isoprene concentration for eg. Surinam (Tropical rainforest: 2.39 ppb), OHP France (Mediterranean forest:2.80 ppb), Shanghai China (Deciduous forest: 2.47 ppb),

(Danum Valley Malaysia: 1.10 ppb) (Jones et al., 2011; Williams et al., 2001; Zannoni et al., 2015).

Once released into the atmosphere isoprene oxidation plays a very critical role in both urban and rural environments throughout the globe. The discovery of its significance in the urban environment was mainly driven by understanding its role as a precursor leading to the formation of secondary pollutants such as ozone back in the 1970s. The city planners in Atlanta, USA were informed that they will have to spend money to reduce a pollutant in the atmosphere which no one was emitting and no one knew where it came from (Jeffries et al., 2013). This was later identified as a case of local air pollution as the city was being influenced by isoprene emissions from surrounding forests (Chameides et al., 1988).

Isoprene is a short-lived species with an atmospheric lifetime of approximately ~1.5 hours (Williams and Warneck, 2012), due to its high chemical reactivity isoprene plays a critical role in the oxidative cycles of the troposphere (Atkinson and Arey, 2003). During the daytime isoprene rapidly reacts with hydroxyl radical (OH radical) [($k_{(isop+OH)}$) 1×10^{-10} cm^3 $molecule^{-1}s^{-1}$] (Carter and Atkinson, 1996) to form peroxy radicals (RO_2) (Pugh et al., 2011). RO_2 in presence of nitric oxide (NO) leads to the formation of oxygenated VOCs such as methyl vinyl ketone (MVK), methacrolein (MACR) as major products of its oxidation as well as formaldehyde and acetaldehyde in varying amounts (Sprengnether et al., 2002). Additionally, in an urban environment isoprene oxidation can lead to noxious oxidant build-up leading to the formation of ground-level ozone due to the catalytic action of nitrogen oxides ($NO_x = NO + NO_2$) (Lelieveld et al., 2008). While in a pristine environment it can lead to the recycling of OH radical and sustaining the oxidation capacity (Lelieveld et al., 2008).

Isoprene in an urban environment is also a precursor of peroxyacetyl nitrate (PAN) which is also a component of urban smog (Seinfeld and Pandis, 1998) and it has been estimated through modelling studies and constrained through measurement data that isoprene is responsible for 37% of global PAN budget (Fischer et al., 2014). Additionally, isoprene in a low NO_x environment can be a precursor to secondary organic aerosol (SOA). This is mainly due to the absence of NO_x, which slows down the reaction rates of the first-degree product which gives more time to particle formation (Kroll et al., 2006). Although the homogeneous nucleation of isoprene yields a low level

of SOA from the original mass (Carlton et al., 2009) but catalyzing the reaction with acidic seed yields aerosol growth (Czoschke et al., 2003).

Oxygenated organic compounds such as acetaldehyde and formaldehyde have strong photochemical sources and are formed by oxidation of precursor hydrocarbons such as alkenes and alkanes (Fortems-Cheiney et al., 2012; Millet et al., 2010). In the case of acetaldehyde direct biogenic emissions from poplar and mosses and lichens have also been reported and account for approximately 23 Tg y^{-1}. Acetaldehyde has a typical lifetime in the order of 1 day (Atkinson et al., 2006) with major sinks as reaction with OH radical (Atkinson et al., 2006), photolysis (Sander et al., 2006), as well as dry deposition and wet deposition, represent minor sinks (Karl et al., 2004). Formaldehyde has a typical lifetime of ~10 hours with major sink as photolysis and reaction with OH radical and photolysis (Williams and Warneck, 2012). In the next section, I discuss modelling biogenic emissions and land-atmosphere interactions in mesoscale modelling.

1.3 Modelling biogenic emissions and land-atmosphere interactions

As per the discussion in previous sections recognition of the important role of BVOCs in air quality and climate has made biogenic emissions an indispensable part of earth system models. Biogenic emissions are studied through emission models which try to represent the emission pattern through mathematical equations on a global scale. The mathematical emission model fits together the physical and chemical processes to present a detailed and cohesive picture of atmospheric conditions and biogenic emissions to predict future conditions and emissions.

Biogenic models may be classified as either a big leaf model or a multi-layer canopy model. Multi-layer models provide detailed leaf-level information and intra-canopy behavior which makes it computationally very expensive and reduces its scope of the study (Dai et al., 2004). An alternate big-leaf model incorporates all the properties of the canopy into a single leaf along with lumping multiple parameters in coupled equations to compute flux values which makes it computationally less expensive (Dickinson et al., 1998).

Currently, BVOC emission models are routinely used in air quality and climate models and the most widely used model is used multi-layer model is the Model of Emissions of Gases and Aerosol from Nature (MEGAN) model (Guenther et al., 2006; Guenther et al., 2012) which uses the base emissions computed from different ecosystems named as plant functional types (PFTs). MEGAN

is further constrained with local environmental factors by using certain parametrizations which will be discussed in much greater detail in chapter 3. MEGAN is embedded in some on-line models and can also run as a stand-alone model.

The base emissions from MEGAN for different PFTs are derived from different field studies and are extrapolated or computed from formaldehyde satellite measurements (Barkley et al., 2013) where no ground-based measurements exist.

The weather research and forecasting model coupled with chemistry (WRF-Chem) (Grell et al., 2005; Skamarock et al., 2008) is a state of the art regional chemical transport model which is widely used as a tool in modelling atmospheric chemistry. It incorporates MEGAN (v 2.04) for the online calculation of biogenic emission. The current version MEGAN model uses an approach where each of the grid cells is divided into different PFTs (Broadleaf, Needleleaf, Shrubs and Herbs) and non-vegetative (Barren) surface. In addition to the PFTs, MEGAN also has defined global gridded dataset of leaf area index (LAI) and gridded emission factor (EF) to account for the geographical variability and season.

The WRF-Chem simulates the key land-atmosphere interaction processes through the Noah land surface model (Chen and Dudhia, 2001). Any land surface model in weather or a climate model must provide at least 4 key parameters to the parent model namely surface sensible heat flux, surface latent heat flux, surface emissivity and surface albedo. This is achieved primarily by providing some key inputs to the land surface model namely land-use/vegetation data, soil texture data, slope, or elevation. Additionally, specifying secondary parameters as a function of the above three through a lookup table. This discussion concerning both the biogenic module and land surface module underscores the fact the land-use data, vegetation data, or the PFTs hold the key to accurately model both atmospheric chemistry and land-atmosphere interactions. The WRF-Chem coupled MEGAN model represents vegetation, water, natural surface, and other features on the land surface using land use landcover data. This thesis has utilized three different vegetation datasets including GlobCover, MOD44B and Landsat vegetation cover fraction dataset. GlobCover provides global composite and land cover maps using input observation from ENVISAT satellite (Arino et al., E.S.A 2012 GlobCover Dataset). MOD44B provides global tree cover percentage at 250m resolution (Dimiceli et al., J.R.G. 2015 . Accessed 2019-06-09).

Landsat vegetation continuous fields provides tree canopy cover data at 30m resolution using input observation from different bands of Landsat-5 (Sexton et al., 2013).

In the next subsequent sections, I discuss the current status of biogenic measurement and modelling research over South Asia followed by the thesis plan.

1.4 Status of biogenic modelling and measurement research over South Asia

MEGAN model has been extensively used over South Asia coupled with chemical transport models (WRF-Chem) to simulate regional atmospheric chemistry (Ghude et al., 2013; Kumar et al., 2014a) and biogenic emissions. However, the base emissions from MEGAN are derived from different field studies and are extrapolated or inverted by constraining formaldehyde satellite measurements (Barkley et al., 2013; Chaliyakunnel et al., 2019) were no ground-based measurements exist. These studies have been found to predict less accurate ground-based measured isoprene flux values especially over the tropical latitudes in comparison to the top-down approach using inversion of satellite data (Stavrakou et al., 2014) as satellite retrieval can be at times difficult especially during the monsoon season over South Asia due the presence of deep convective clouds (Lawrence and Lelieveld, 2010). Recently, a study showed that the isoprene spectral signatures are detectable from space using the satellite-borne Cross-track Infrared Sounder (CrIS) and emphasized on ground-based validation for the algorithm (Fu et al., 2019). Therefore, ground-based isoprene measurements are necessary to validate the current representation of biogenic emissions in the MEGAN model over South Asia.

Till date, only a few studies have reported measurements of these biogenic compounds in summer and the winter season from the South Asian atmospheric environment (Chandra and Sinha, 2016; Hakkim et al., 2019; Sarkar et al., 2016; Sinha et al., 2014). Additionally, Varshney and Singh (2003) have reported isoprene emissions from 40 tree species and estimated the isoprene emissions from forests over India. But no measurements of biogenic isoprene have been reported for the monsoon season from any region in India which is one of the most important seasons of the year over this region as it represents a period characterized by convective activity that can uplift surface emissions to the upper atmosphere (Lawrence and Lelieveld, 2010). During the monsoon season,

one would expect stronger biogenic emissions as the vegetation is no longer limited by the availability of moisture.

Finally, it is imperative to evaluate the model with continuous online ground-based measurements to assess the representation of different input parameters (For eg. land use land cover) and parametrizations in the existing model setup which is currently widely used by the atmospheric chemistry modelling community.

1.5 Research motivation and thesis structure

As discussed in previous sections BVOCs are emitted from vegetation and play a pivotal role in atmospheric chemistry. Isoprene dominates the total global budget of biogenic emissions and is primarily emitted from trees as a by-product of photosynthesis. Trees also significantly impact land-atmosphere feedbacks to influence the local microclimate and air quality. The N.W IGP is the agricultural "bread basket" of South Asia and mixed agroforestry practices are prevalent over the region. The monsoon season over the region provides a unique window to investigate the impact of vegetation on atmospheric chemistry and land atmosphere-interactions with the maximum signal to noise ratio. During this season vegetation throughout the region is not moisture limited while many anthropogenic fire sources such as crop residue burning and forest fires are absent. This period presents a complex interplay of biogenic emissions, micrometeorology, atmospheric chemistry.

Thus through this thesis, I would like to address the following questions:

1- What is the ambient variability, diel profile of isoprene, formaldehyde, methyl vinyl ketone, methacrolein and acetaldehyde during monsoon season?
2- What are the major daytime sources of these compounds in the monsoon season when biogenic sources are strongest relative to other sources over the north-west Indo-Gangetic Plain?
3- What is the degree of underestimation of cropland trees in some major agroforestry intensive regions of the world including north-west Indo-Gangetic Plain?
4- How do the missing cropland trees affect atmospheric chemistry and micrometeorology of an agricultural region like north-west Indo-Gangetic Plain?

5- What is the extent to which trees in croplands may help to reduce crop yield losses due to heat stress and ozone pollution?
6- Can expanding agroforestry tree cover result in further crop yield gain and climate co-benefits in the future?

The first two questions are addressed in chapter 2 where first in-situ measured dataset of isoprene, formaldehyde, MVK+MACR and acetaldehyde from India is presented during the monsoon season with evidence of a strong biogenic isoprene emission. The chapter also discusses the main sources of formaldehyde and acetaldehyde over the N.W IGP during the monsoon season and how it is different from the summer season. Chapter 3 discusses the details of different processes and datasets used by the WRF-Chem model. The chapter ends with details on how realistic the WRF-Chem coupled MEGAN model can represent ground-based measurements over N.W IGP. The fourth, fifth and sixth question is addressed in chapter 4 where it discussed the potential impacts of omitting trees in croplands in WRF-Chem land surface and MEGAN model which hampers the ability accurately simulate energy and chemical fluxes in agricultural regions. Finally, the chapter presents a 'what if scenario' simulation where it is shown that expanding the agroforestry tree in the cropland areas can help mitigate climate change along with increasing crop yield gain.

Chapter: 2

Emission drivers and variability of ambient isoprene, formaldehyde and acetaldehyde in north-west India during monsoon season

The contents of this chapter have been published in the international peer reviewed journal Environmental Pollution as (Mishra and Sinha, 2020)

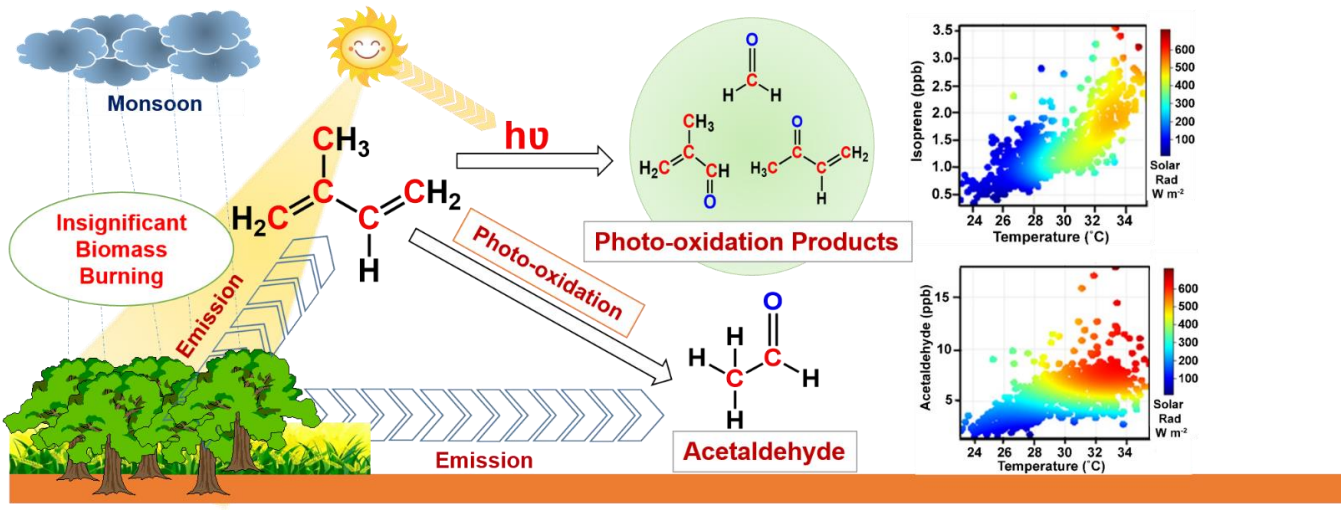

Figure 2.1: Graphical abstract of the chapter.

2.1 Abstract

Isoprene, formaldehyde and acetaldehyde are important reactive organic compounds which strongly impact atmospheric oxidation processes and formation of tropospheric ozone. Monsoon meteorology and the topography of Himalayan foothills cause surface emissions to get rapidly transported both horizontally and vertically, thereby influencing atmospheric processes in distant regions. Further in monsoon, Indo-Gangetic Plain is a major rice growing region of the world and daytime hourly ozone can frequently exceed phytotoxic dose of 40 ppb O_3. However, the sources and ambient variability of these compounds which are potent ozone precursors are unknown. Here, I investigate the sources and photochemical processes driving their emission/formation during monsoon season from a sub-urban site at the foothills of the Himalayas. The measurements were performed in July, August and September using a high sensitivity mass spectrometer. Average ambient mixing ratios ($\pm 1\sigma$ variability) of isoprene, formaldehyde, acetaldehyde, and the sum of methyl vinyl ketone and methacrolein (MVK+MACR), were 1.40 ± 0.30 ppb, 5.70 ± 0.90 ppb, 4.50 ± 2.00 ppb, 0.75 ± 0.30 ppb, respectively, and much higher than summertime values in May. For isoprene these values were comparable to mixing ratios observed over tropical forests. Surprisingly, despite occurrence of anthropogenic emissions, biogenic emissions were found to be the major source of isoprene with peak daytime isoprene driven by temperature ($r \geq 0.8$) and solar radiation. Photo-oxidation of precursor hydrocarbons were the main sources of acetaldehyde, formaldehyde and MVK+MACR. Ambient mixing ratios of all the compounds correlated poorly with acetonitrile ($r \leq 0.2$), a chemical tracer for biomass burning suggesting negligible influence of biomass burning during monsoon season. Our results suggest that during monsoon season when radiation and rain are no longer limiting factors and convective activity causes surface emissions to be transported to upper atmosphere, biogenic emissions can significantly impact the remote upper atmosphere, climate and ozone affecting, rice yields.

2.2 Introduction

Isoprene is the most abundant hydrocarbon emission into the atmosphere after methane (Goldstein and Galbally, 2007; Palmer et al., 2006). Owing to its high chemical reactivity (daytime atmospheric lifetime typically < 90 minutes) isoprene plays a critical role in global oxidant chemistry (Lelieveld et al., 2008) and is a major hydrocarbon precursor of tropospheric ozone (Chameides et al., 1988; Fuentes et al., 2000; Pierce et al., 1998) and organic aerosols (Andreae and Crutzen, 1997; Claeys et al., 2004), which influence the Earth's climate and are atmospheric pollutants.

During the daytime isoprene oxidation is driven by hydroxyl radicals (OH) forming oxygenated VOCs such as methyl vinyl ketone (MVK), methacrolein (MACR) as major products of its oxidation as well as formaldehyde and acetaldehyde in varying amounts (Atkinson et al., 1989; Sprengnether et al., 2002). It has been reported that plants synthesize isoprene using the Methylerythritol 4-phosphate pathway (MEP) using carbon pools of photosynthesis which is mainly dependent on enzymatic activities (Bamberger et al., 2017; Sharkey and Singsaas, 1995; Sharkey et al., 2008). As a consequence, the biogenic isoprene emissions are strongly dependent on environmental and physiological conditions (i.e., temperature and radiation, soil moisture, leaf area index (LAI), and leaf age) (Guenther et al., 2012; Guenther et al., 1993; Niinemets et al., 1999; Stavrakou et al., 2014), and type of vegetation (i.e., grassland, forest, shrubland) (Guenther et al., 1995).

Oxygenated organic compounds such as acetaldehyde and formaldehyde have strong photochemical sources and are formed by oxidation of precursor hydrocarbons such as alkenes and alkanes (Fortems-Cheiney et al., 2012; Millet et al., 2010). In the case of acetaldehyde direct biogenic emissions from poplar and mosses and lichens have also been reported. These oxygenated volatile organic compounds are among the most reactive and abundant ambient oxygenated compounds. In addition to fueling formation of surface ozone in combination with nitrogen oxides, they also act as a tropospheric source of hydroxyl and hydroperoxy radicals. By forming peroxy acetyl nitrates (PAN) they move reactive nitrogen far away from its emission sources to the upper troposphere and downwind regions, playing significant roles in regional oxidant chemistry.

In addition to the biogenic sources of isoprene and photochemical sources of acetaldehyde, formaldehyde, MVK+MACR, all of these compounds can also be emitted from biomass burning

sources (Andreae, 2019; Sinha et al., 2019; Sinha et al., 2014). The northern Indo-Gangetic plains are one of the world's highly populated (~400 million people) and productive rice growing regions. It therefore has potentially significant biomass burning sources in addition to biogenic sources. In addition, during most of the year the temperature and radiation (Kumar et al., 2016b) are sufficient for photochemically forming acetaldehyde, formaldehyde, methacrolein and methyl vinyl ketone. Thus, this densely populated region of the world with large anthropogenic and natural sources can be a significant source of isoprene through biogenic and biomass burning sources and for formaldehyde, acetaldehyde, MVK+MACR additionally through photochemical sources. In fact, hourly daytime ozone mixing ratios frequently exceed the phytotoxic dose of 40 ppb (Mills et al., 2018) during monsoon season from July to September (see Figure S3, of Kumar et al., 2016), when paddy crops cover a vast part of the land use in the region.

Though not as reactive as acetaldehyde and isoprene, methanol and acetone are also among the most abundant compounds in ambient air and can have biogenic and photochemical sources in addition to strong anthropogenic sources (Schade and Goldstein, 2006). Based on a quantitative source apportionment study carried out during summer in the north-west Indo-Gangetic plain (Pallavi et al., 2019), anthropogenic sources such as industrial emissions and solvent use as well as biofuel use and waste disposal and traffic (cars and two-wheelers) were the main drivers controlling the ambient mixing ratios of these compounds in the region, with both biogenic and photochemical sources contributing less than 25%. The industrial and traffic sources are expected to be as active during the monsoon season as well. Hence in this study where our main focus is to examine biogenic and photochemically formed compounds during the monsoon season, I did not consider them further.

Unfortunately, due to paucity of in-situ measurements of these compounds from the region, there is a lack of understanding concerning the major seasonal processes that control the ambient variability of these compounds, which can act as potent ozone precursors. Till date only a few studies have reported measurements of these compounds in summer and in winter season from the South Asian atmospheric environment (Chandra and Sinha, 2016; Hakkim et al., 2019; Sarkar et al., 2016; Sinha et al., 2014). To the best of our knowledge no measurements of isoprene and acetaldehyde have been reported for the monsoon season from any region in India. The monsoon season is one of the most important seasons of the year over this region as it represents a period

characterized by convective activity that can uplift surface emissions to the upper atmosphere (Lawrence and Lelieveld, 2010), facilitating long range transport of surface emissions. Furthermore, from the point of view of biogenic emissions from vegetation and oxidation chemistry, in contrast to the summer season, this a period when one would expect stronger biogenic emissions as the vegetation is no longer limited by availability of moisture.

Here, I report and analyze a two-month long dataset to investigate the emission processes and ambient variability of isoprene, acetaldehyde, formaldehyde, MVK+MACR, at a sub-urban site in the foothills of the Himalayas during the monsoon season. By use of a chemical marker compound for biomass burning namely acetonitrile, which was measured simultaneously, I first examined the relative importance of biomass burning sources and biogenic sources during the monsoon season. Next I examined the temperature and radiation dependence in addition to tracer data, for investigating the biogenic and photochemical sources of these compounds. Finally, I analyzed the daytime variability of the compounds and influence of boundary layer growth to assess the role of atmospheric dilution on the observed variability during monsoon and summer seasons. After comparison of the meteorological and emission drivers of these compounds I discuss the larger implications of our findings.

2.3 Materials and Methods

The site and climatology of air masses for different seasons at the site has been described in detail in previous published works (Kumar et al., 2016b; Pawar et al., 2015). The study was conducted at a sub-urban site called IISER Mohali (Pawar et al., 2015; Sinha et al., 2015) which is located in the Himalayan foothills (Figure 2.2 a). To its north-east, lie urban agglomerates such as Chandigarh and Panchkula city, whereas the north-west fetch region consists of mainly rural and agricultural land. The south-east fetch region consists of rural and industrial regions from the more densely populated part of the Indo-Gangetic Plain (Figure 2.2 b). Delhi is 300 km south of the measurement site. The rural and agricultural areas have large area under poplar and eucalyptus planted typically at the periphery of agricultural fields (India-FRI, 2019). During the monsoon season, the main fetch region as shown in the wind rose plot (Figure 2.2 c) was the region south-east of the site advecting air masses to the measurement site at wind speeds frequently exceeding 5 m s^{-1}. In other seasons including summer, the predominant fetch region is from the north-west (Kumar et al., 2016b). The meteorological data presented in this study were acquired at a temporal

resolution of 1 minute using an automatic weather station from 21st July -19th September 2012 (Met One Instruments Inc., Rowlett, USA) and details about these sensors are available in Sinha et al., 2014.

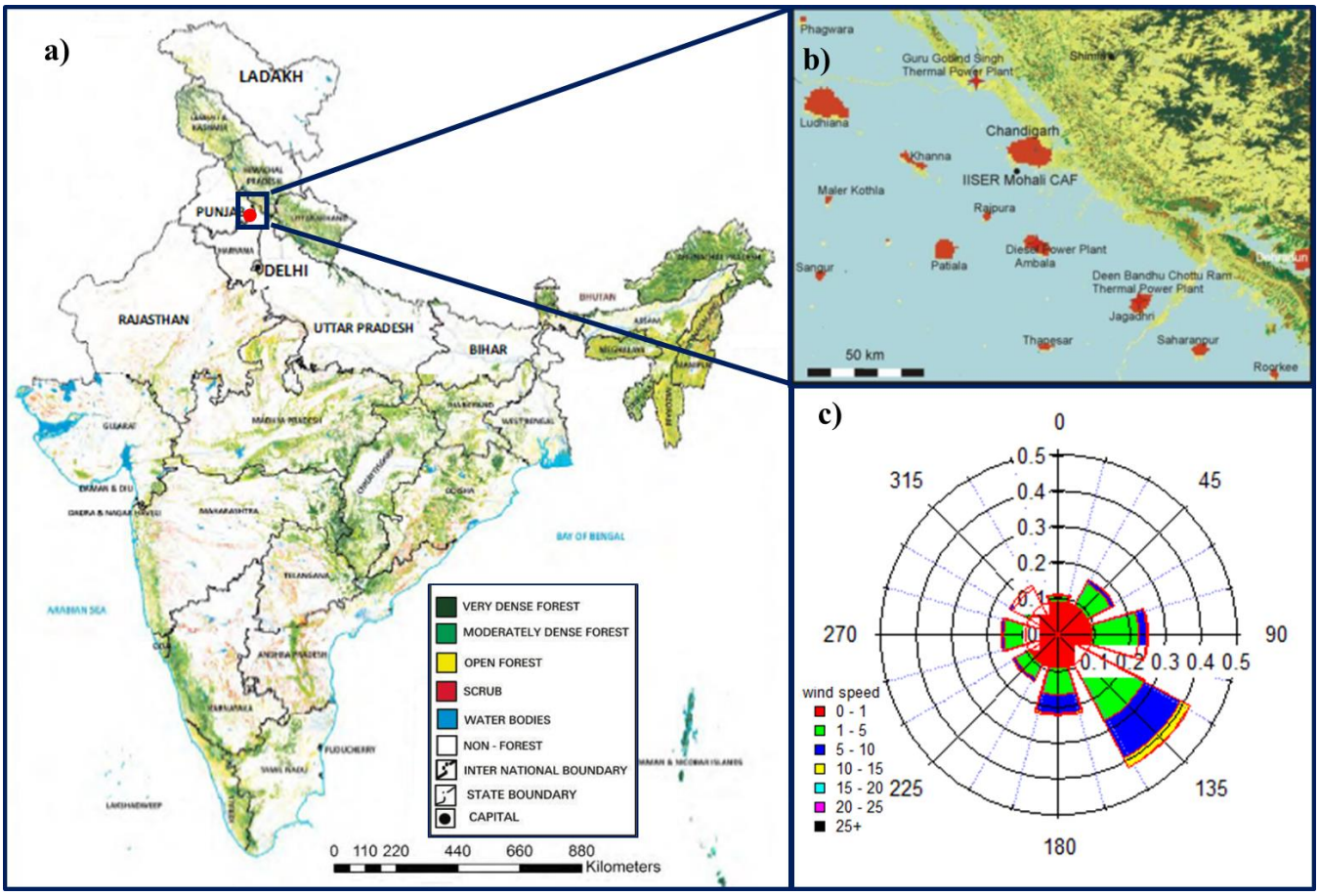

Figure 2.2. (a) Location of Mohali on Land classification map (adapted from Indian State of Forest report-2019, Ministry of Environment, forest and climate change, India) (b) Exact location of measurement facility (adapted from ESA globe cover 2009) (c) wind rose plot derived from one-minute wind speed and wind direction data at the measurement site (30.667° N, 76.729° E) from 21st July – 19th September 2012.

Measurements of isoprene, sum of methyl vinyl ketone and methacrolein (MVK+MACR), acetaldehyde, formaldehyde and acetonitrile were carried out using a proton-transfer reaction quadrupole mass spectrometer (PTR-QMS; Model 11-07HS-088; Ionicon Analytik Gesellschaft, Austria). Specific analytical details of the PTR-MS system and operational details, calibration experiments as well as the data and quality control protocols have already been provided for the same instrument in detail when it was operated in May 2012 to measure isoprene, MVK+MACR as well as acetaldehyde and acetonitrile previously (Sinha et al., 2014). Additional details relevant for long term measurements have also been provided elsewhere (Chandra and Sinha, 2016; Sinha

et al., 2014). Hence only brief description is provided here for these compounds and more detailed description concerning the quantification of formaldehyde, which requires humidity dependent correction for accurate quantification. The instrument was operated at 135 Td in selected ion monitoring mode. Isoprene (C_5H_8; M.W: 68.12 g/mol) was detected at m/z = 69 (Blake et al., 2009; de Gouw and Warneke, 2007) after chemical ionization with hydronium reagent ions. Previous PTR-MS studies have reported that m/z 69 can have nominal isobaric contributions from furan too which is emitted from combustion and biomass burning sources (Akagi et al., 2011; Christian et al., 2004; Yokelson et al., 2013). In the work by (Sarkar et al., 2016) in Nepal in the winter of December 2012-January 2013 using a time of flight mass spectrometer (PTR-TOF –MS), which could distinguish between furan and isoprene, we found that m/z 69 was mainly due to isoprene with furan contributing a maximum of 25 % at m/z 69 even in nighttime biomass burning emission plumes. For reasons discussed in the results and discussion section in detail and based on results of previous studies from our group in this atmospheric environment (Kumar and Sinha, 2014) at the same site in summer using the VOC-OHM technique which showed that the dominant contributor to m/z 69 was isoprene, we are therefore confident that the daytime m/z 69 signal is majorly due to isoprene. The sum of MVK+MACR (C_4H_6O; M.W: 70.09 g/mol; C_4H_6O; M.W: 70.09 g/mol), acetonitrile (CH_3CN: M.W: 41.05 g/mol) and acetaldehyde (C_2H_4O; M.W: 44.05 g/mol) were detected at m/z = 71, m/z =42 and m/z =45, respectively. The specificity of PTR-MS for detection of these compounds has been validated previously (de Gouw and Warneke, 2007). However, even though methyl ethyl ketone has been detected at m/z 73 using a quadrupole PTR-MS in several previous studies, more recent studies have cautioned against attributing the measurement at m/z 73 in high isoprene and anthropogenically influenced environments, as there can be significant contribution from methylglyoxal, 2-methylpropanal and butanal in such measurements (Yáñez-Serrano et al., 2015; Michoud et al., 2018). As we could not be sure about the identity and contribution of these isobaric compounds using only quadrupole PTR-MS measurements, we are therefore not reporting them in this study. Formaldehyde (HCHO; M.W: 30.03 g/mol) was detected at m/z = 31. The proton affinity of formaldehyde (PA = 715.7 kJ mol^{-1}) is only marginally higher than that of water (PA = 691 kJ mol^{-1}) and so the sensitivity of formaldehyde decreases with increasing humidity, which is important to account for during ambient conditions characterized by high humidity (Vlasenko et al., 2010; Warneke et al., 2011), which is the case during the summer monsoon season in India. To account for the same, we

therefore applied humidity corrections to the formaldehyde data in keeping with the method proposed and validated by (Cui et al., 2016) over a wide range of humidities. The equations and method are described as following.

In PTR-MS the reaction between formaldehyde and hydronium ion takes place as shown R1. But since there is very slight difference between the proton affinity (PA) of formaldehyde (PA = 715.7 kJ mol^{-1}) and that of water (PA = 691 kJ mol^{-1}), backward reaction (R2) can take place and as a result the sensitivity of formaldehyde decreases with increasing humidity causing underestimation of the formaldehyde concentration in the ambient air.

$$HCHO + H_3O^+ \longrightarrow HCHO.H^+ + H_2O \qquad R1$$

$$HCHO.H^+ + H_2O \longrightarrow HCHO + H_3O^+ \qquad R2$$

In this study humidity correction was applied to the data following the method proposed and validated by (Cui et al., 2016), who also operated their instrument at ~135 Td and obtained a humidity based correction spanning a wind range of RH. The rate constant for the proton transfer reaction of formaldehyde was corrected by using (equation 2.1 below) using measured absolute humidity. The corrected rate constant was then used to obtained the calculated sensitivity for HCHO in ncps/ppb as described by (de Gouw and Warneke, 2007). Equation 2.1 and 2.2

$$k = 0.007\,(AH^2) - 0.0588\,AH + 1.8139 \qquad 2.1$$

Where, *k* is the rate for proton transfer reaction (HCHO with H_3O^+), AH is the absolute humidity

$$S = \frac{k\,L}{\mu_0 N_0}\; X\; \frac{N^2}{E}\; X\; \frac{T(RH^+)}{T(H_3O^+)} \qquad 2.2$$

Where, S is sensitivity (ncps/ppb), *k* is the rate constant for proton transfer, L is the length of drift tube 9.3 cm, μ_0 is the ion mobility at STP, N is the number density of gas in the drift tub, $T(RH^+)\ and\ T(H_3O^+)$ is the transmission efficiency for RH^+ and H_3O^+ respectively. We observed that the rate of reaction between formaldehyde and hydronium ion showed a linear negative dependence on absolute humidity (Figure 2.3) consistent with Cui et al. 2016.

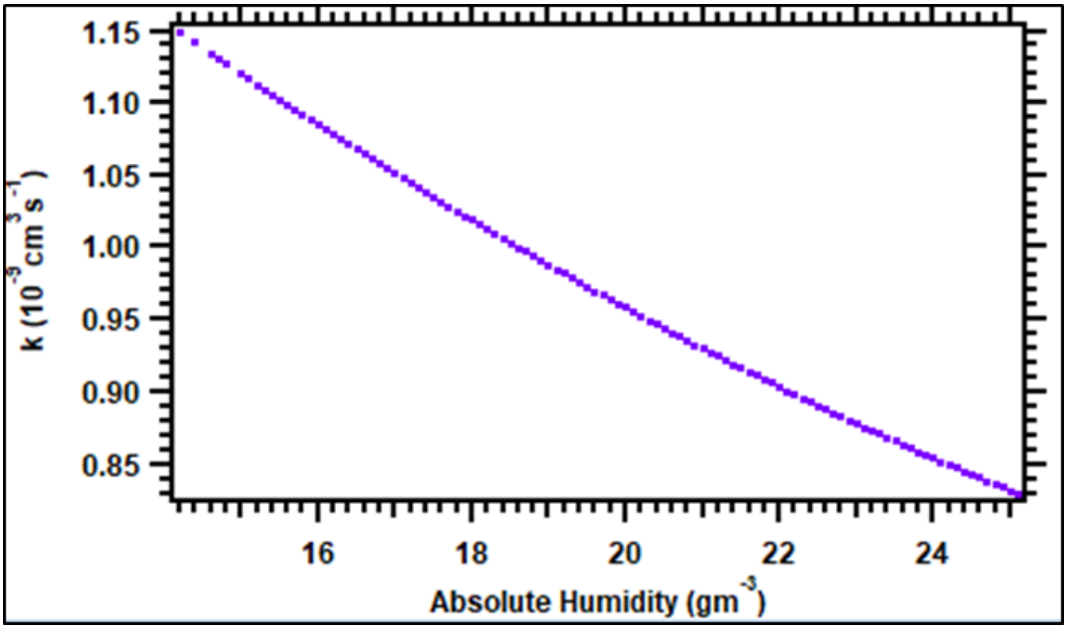

Figure 2.3. Dependence of rate constant ($k_{HCHO + H3O^+}$) of the reaction between formaldehyde with hydronium ion on absolute humidity.

Calibration experiments and ambient measurements were carried out under identical operating conditions with a dwell time of 1s at the corresponding m/z channel of the compound. Background signal at these m/z channels within the instrument were collected regularly by sampling VOC free zero air in the instrument (Kumar and Sinha, 2014; Sinha et al., 2014). The values in Table 2.1 list the sensitivity factors (ncps/ppb), measurement uncertainty, detection limit, zero background range at these mass to charge ratios (m/z). The overall uncertainty for isoprene, sum of MVK+MACR and acetaldehyde based on the calibration was less than 10% whereas for formaldehyde was estimated to be less than 30%.

Table 2.1 Results of PTR-MS calibration experiment

m/z	Compound	Sensitivity (ncps/ppbv)	Uncertainty	Zero-Background Range (ppbv)	Detection Limit (ppbv)
42	Acetonitrile	16.6 ± 1.9	9.1%	0.30	0.05
45	Acetaldehyde	17.6 ± 0.4	8.4%	0.45	0.09
69	Isoprene	8.2 ± 0.2	10%	0.51	0.12
71	MVK+MACR	18.2 ± 0.4	10%	0.32	0.10

The boundary layer heights were obtained using the ERA5 reanalysis dataset, available in the European Centre for Medium-Range Weather Forecasts (ECMWF, Data Access: December 2020). We used the reanalysis ERA5 single level data (surface level) after downloading it in network common data form (netCDF format) and the same was interpolated at Mohali (Longitude:76.729°E; Latitude:30.667°N) using the climate data operator package.

While performing the evaluation with boundary layer height, I had to take a careful decision about which reference dataset to choose. I opted for ERA-5 for the following reasons:

1. Fine spatial resolution of 0.25°×0.25°, Please note that MERRA 2 data is the only other global reanalysis dataset available at hourly temporal and at a relatively coarser resolution (0.625°-0.5° spatial resolution).
2. ERA5 uses 4D Var Advanced-Data assimilation system of ECMWF, which is much advanced in comparison to MERRA 2 global data assimilation system. This has also yielded better performance of ERA5 against the observation dataset (Hersbach et al., 2020; Olauson, 2018). The ERA5 reanalysis datasets has also been extensively validated across India to assess hydrological applications and assessment of vertical air motion against IMD dataset along with other Reanalysis products (Mahto and Mishra, 2019; Uma et al., 2020). The analysis shows that ERA-5 outperforms the other reanalysis products for the monsoon season in India (Mahto and Mishra, 2019).

2.4 Results and Discussion

2.4.1 General meteorology and temporal characteristics of isoprene, MVK+MACR, acetaldehyde, formaldehyde, acetonitrile

The measurements reported in this work were acquired from 21st July 2012 to 19th September 2012 during the monsoon season. In this season, the north-west Indo Gangetic Plain is characterized by high average daily relative humidity (~ 65%), heavy rainfall events during the wet spells, thunderstorm activity and diffused solar radiation even though the average daily temperatures are circa 30°C (Kumar et al., 2016b). During the measurement period the average hourly daytime temperature always remained above 22°C with the average day time maximum temperature even reaching ~36°C. The average maximum and minimum relative humidity ranged between ~85% at 05:00LT to 65% at 15:00LT. The average wind speed was ~ 4.5 ms^{-1} with south-west as the predominant fetch region as shown in Figure 2.2 C.

In Figure 2.4 we show the time series in the mixing ratios of VOCs and solar radiation at 1-hour temporal resolution (derived from n > 80,000 measurements). This period was marked by several major rainfall events (> 3 mm rainfall.). The top panel displays mixing ratios of isoprene and its major oxidation products, namely MVK+MACR. The second panel shows the mixing ratios of formaldehyde and acetaldehyde, that are major VOC oxidation products and can also be emitted by biomass burning and biogenic sources. The third panel shows the mixing ratios of acetonitrile, a good molecular tracer for biomass burning and the solar radiation, which is helpful to identify strongly overcast days. The bottom panel shows the ambient temperature and hourly accumulated rainfall for events exceeding 3 mm as solid blue bars (extended dashed blue lines are added for convenience to interpret VOC data in upper panels. Table 2.2 and 2.3 tabulate the average temperature, solar radiation and rainfall for days with heavy rainfall and dry conditions, respectively. The contrasts in the meteorological conditions during wet and dry spells of the monsoon were helpful for investigating photochemical sources of the oxygenated compounds. In addition, it also enabled investigation of biogenic emissions of isoprene which are dependent on the plant functional types, temperature and photosynthetic active radiation (Guenther et al., 2006). Significant variability was observed in the ambient mixing ratios of isoprene and its oxidation products on days with contrasting meteorological conditions. The days associated with cooler conditions marked with heavy rainfall and cloudy days were characterized by low mixing ratios of

isoprene and its oxidation products: isoprene (< 0.9 ppb), formaldehyde (< 5.2 ppb), acetaldehyde (< 4.1 ppb), and MVK+MACR (< 0.6 ppb) while days with warmer conditions and break in the rainfall activity were characterized by high mixing ratios of isoprene and its oxidation products: isoprene (>2 ppb), formaldehyde (>6.5 ppb), acetaldehyde (>8.1 ppb), and MVK+MACR (>0.8 ppb). The average daytime mixing ratios of isoprene and its oxidation products were higher relative to the daily average values suggesting stronger sources for these compounds in the daytime during the monsoon season. The average mixing ratios (±1σ ambient variability) of isoprene, formaldehyde, MVK + MACR, acetaldehyde and acetonitrile were 1.4 ± 0.3 ppb, 5.7 ± 0.9 ppb, 0.7 ± 0.3 ppb, 4.5 ± 2.0 ppb and 1.0 ± 0.9 ppb, respectively. The marked differences in the daytime mixing ratios of isoprene and its oxidation products between contrasting meteorological conditions, suggests significant isoprene emissions from vegetation and strong photochemical sources of acetaldehyde and formaldehyde. These are examined in more detail in the next section.

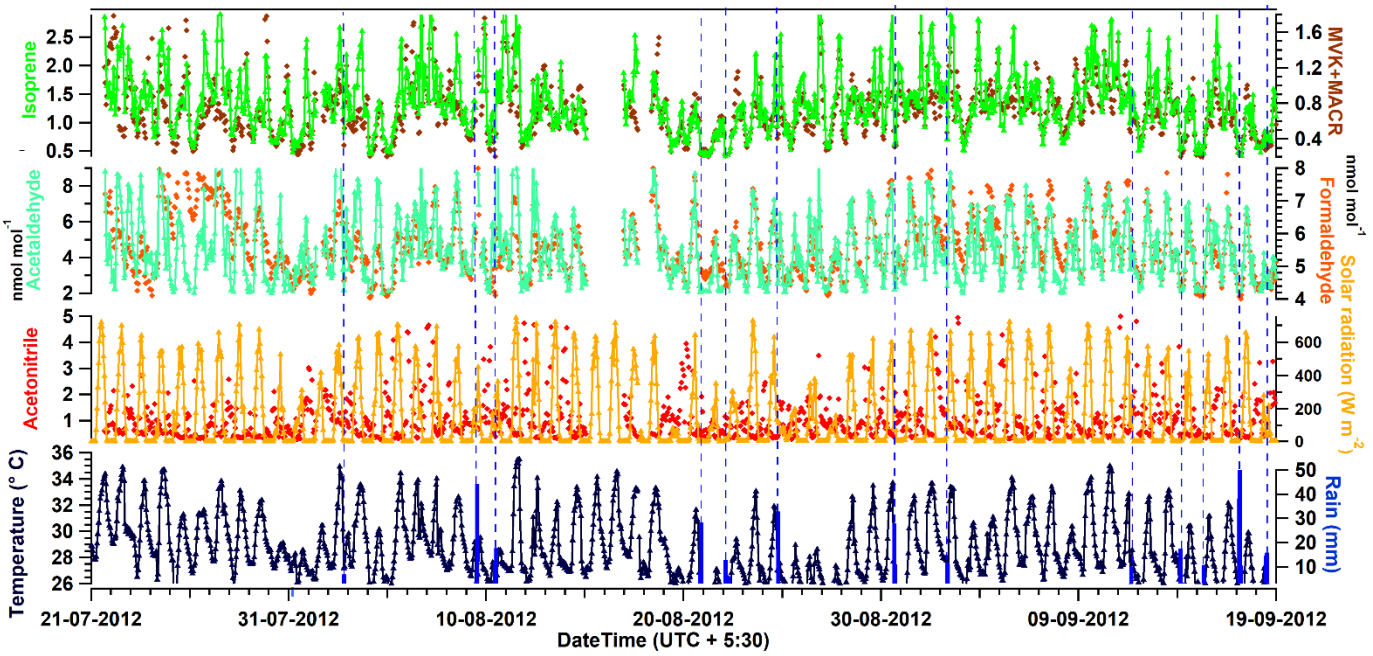

Figure 2.4 Time series of the hourly averaged measured mixing ratios of isoprene, isoprene oxidation products as MVK+MACR (top panel), formaldehyde and acetaldehyde (second panel), and acetonitrile and solar radiation (third panel), temperature bottom panel) from 21.07.2012-19.09.2012. Hourly accumulated rainfall for rain events >3 mm are shown in bottom panel as solid blue bars (extended dashed blue lines are added for convenience to interpret VOC data in upper panels)

Table 2.2: Average temperature, solar radiation and rainfall for days associated with heavy rainfall and cloudy conditions

Date	Temperature (˚C)	Solar radiation (W m^{-2})	Rainfall (mm)
09th August	27.5	175	49
20th August	25.8	138	39
22nd August	27.0	182	42
18th September	24.9	131	35

Table 2.3: Average temperature and solar radiation for days with warmer conditions and break in the rainfall activity and higher solar radiation

Date	Temperature (˚C)	Solar radiation (W m^{-2})
27th July	31.5	370
05th August	28.3	340
06th August	31.2	330
11th August	32.5	420

2.4.2 Analyses of sources of isoprene and the oxygenated VOCs during the monsoon season

It has been reported previously from the same site in summer season of 2012 during May (Sinha et al., 2014) that biomass burning for garbage disposal (Sharma et al., 2019) and from crop residue burning activity during post-harvest months of April-May and Oct-Nov (Kumar et al., 2016b) can act as a source of isoprene and several oxygenated VOCs as these compounds are emitted from such pyrogenic sources (Akagi et al., 2011; Christian et al., 2004; Yokelson et al., 2013). Biomass

burning activity can be inferred from enhancements in acetonitrile mixing ratios (emission tracer for biomass burning) (Holzinger et al., 1999) along with enhancement in daily fire counts as shown and reported by (Kumar et al., 2016b). During the monsoon season, the daily average acetonitrile mixing ratios were 40 % lower relative to the summer season (May-2012: 1.4 ppb (Sinha et al., 2014); 21st July-19th September-2012: 1.0 ppb). This was mainly due to absence of regional crop residue burning, and generally wet conditions during the monsoon season which are not conducive for open biomass burning. Correlation of day-time and night- time hourly averaged values of isoprene and acetaldehyde with acetonitrile for the monsoon season and summer season (dataset reported in Sinha et al. 2014) are presented in Figure 2.5.

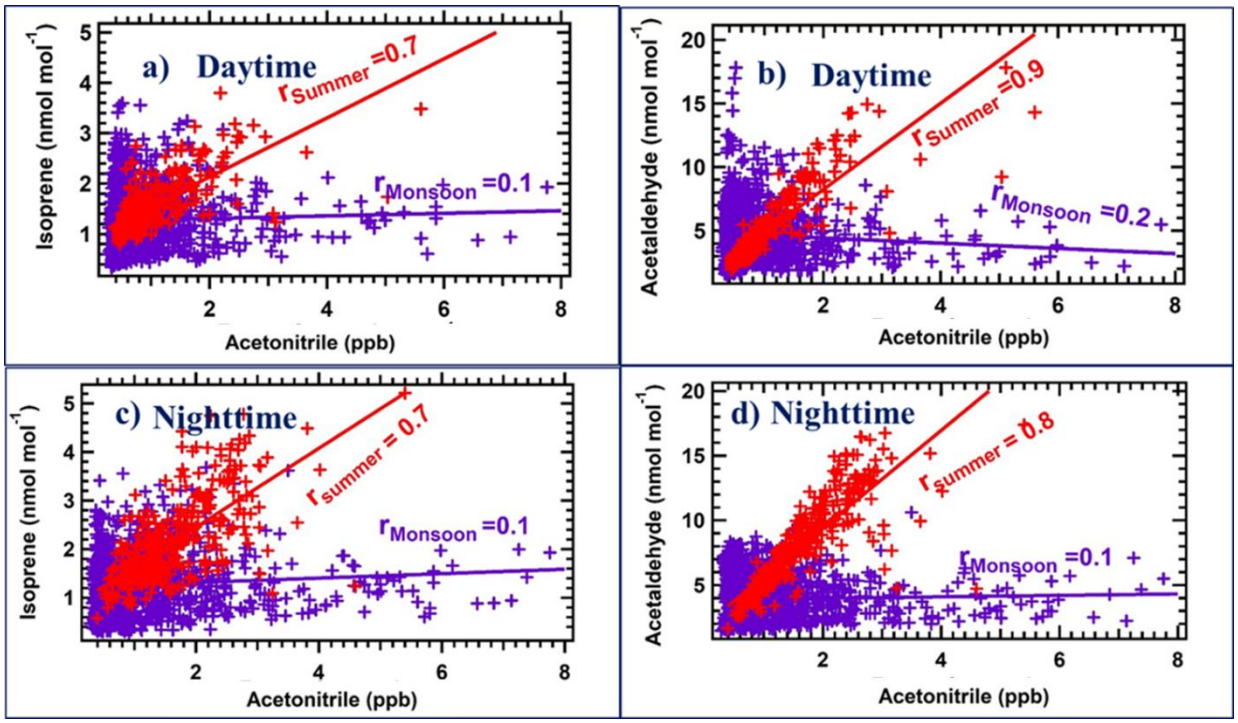

Figure 2.5 Correlation of hourly averaged mixing ratios of a) day-time isoprene with day-time acetonitrile b) day-time acetaldehyde with day-time acetonitrile c) night-time isoprene with night-time acetonitrile and d) night-time acetaldehyde with night-time acetonitrile during monsoon season (21.07.2012-19.09.2012) and summer season (01.05.2012-31.05.2012)

During the monsoon season there was hardly any correlation of isoprene and acetaldehyde with acetonitrile ($r \leq 0.2$), whereas in summertime at the same site, the hourly averaged daytime and nighttime isoprene and acetaldehyde correlated significantly with acetonitrile ($r \geq 0.7$). Similarly, for formaldehyde, and the sum of MVK+MACR there was no significant correlation with acetonitrile during the monsoon season (r=0.1 for both day and night-time), but significant

correlation during summer ($r_{day} \geq 0.6$ and $r_{night} = 0.7$; Figure 2.6). These results suggest that the biomass burning sources are not the drivers of the ambient abundance of these compounds during the monsoon season, in contrast to the summer.

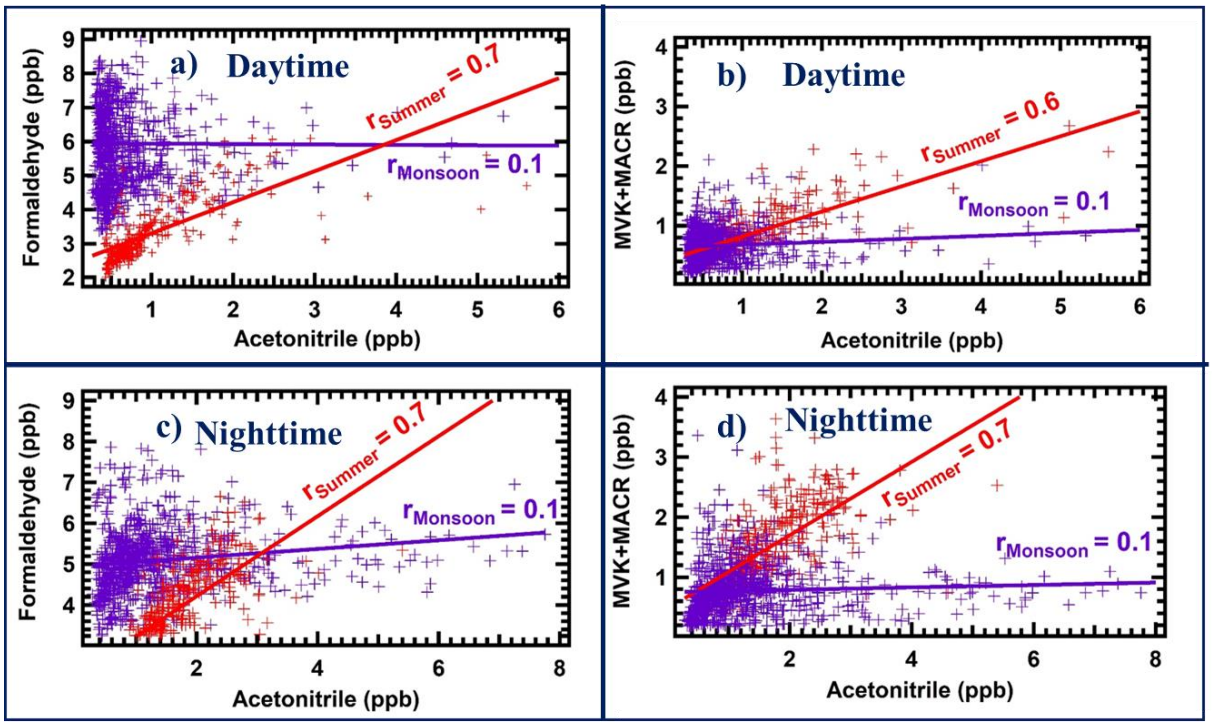

Figure 2.6 correlation of a) day-time formaldehyde with day-time acetonitrile b) day-time MVK+MACR with day-time acetonitrile c) night-time formaldehyde with night-time acetonitrile and d) night-time MVK+MACR with night-time acetonitrile using hourly averaged data for (21.07.2012-19.09.2012) and (01.05.2012-31.05.2012) at the measurement site

Further corroboration of the negligible influence of biomass burning during the monsoon season can be found in the monthly regional fire counts over the N.W IGP region (28°N to 33°N and 72°E to79°E; Figure 2.7) detected by the Moderate Resolution Imaging Spectroradiometer (MODIS) installed on two sun-synchronous polar orbiting satellites called Aqua and Terra (MODIS: https://earthdata.nasa.gov/earth-observation-data/near-real-time/firms). Thus, during the monsoon season, the biomass burning source does not seem to exert a strong control on the ambient levels of these compounds. We now analyze the role of biogenic and photochemical sources on these compounds.

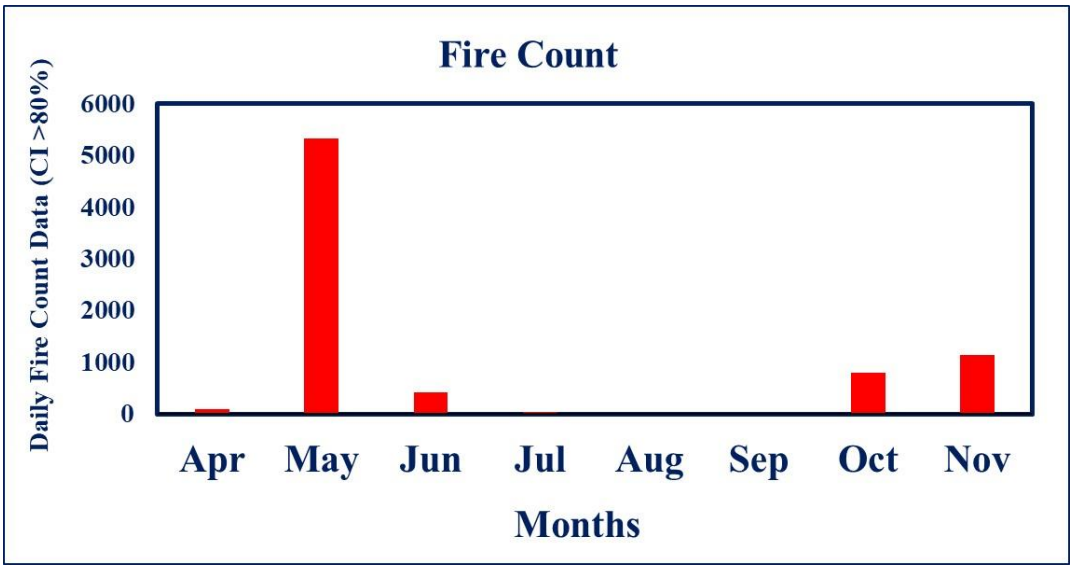

Figure 2.7 Monthly accumulated daily fire counts detected by detected by Moderate Resolution Imaging Spectroradiometer on-board Terra and Aqua satellite at confidence interval ≥ 80% over the north-west Indo-Gangetic Plain (28°N to 33°N and 72°E to79°E) during April-November 2012

Isoprene emission through enzymatic activity depends strongly on temperature, solar radiation (Sharkey, 2001) and substrate availability (Li et al., 2011; Rasulov et al., 2014). Co-synchronous variability in isoprene mixing ratios and solar radiation in the one-minute resolution data measured on 27th July 2012, with dips and peaks, spanning a range of 1.5 ppb to 5.0 ppb isoprene over the range of 300-750 W m^{-2} solar radiation, were observed during our study (Figure 2.8 a).

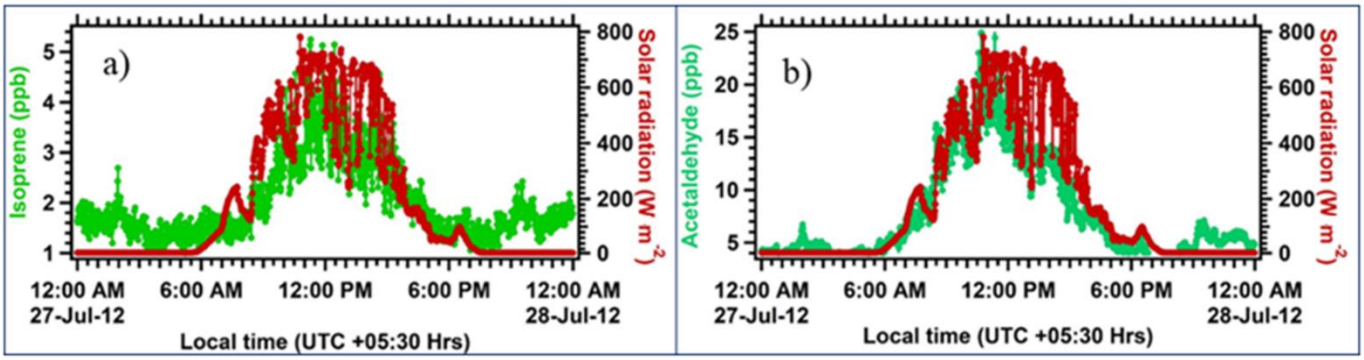

Figure 2.8 Individual events highlighting the co-synchronous variability of a) isoprene with solar radiation on 27th July 2012 b) acetaldehyde with solar radiation on 27th July 2012

Generally, isoprene emission rates increase with temperature until about 40-45 °C, beyond which the heat is no longer conducive for enzymatic processes and stomatal closure occurs to prevent

excessive water loss due to transpiration. The temperatures during the study period in monsoon were below 40 ℃ and as the soil was not moisture limited due to rains, these conditions favoured biogenic emissions. High daytime isoprene mixing ratios (>2 ppb) were frequently observed on warm and sunny days during the monsoon season. To elucidate the temperature and radiation dependence, we plotted the hourly daytime isoprene mixing ratios as a function of the ambient temperature color coded with the corresponding solar radiation. (Figure 2.9 a). The correlation analysis of isoprene with solar radiation and ambient temperature revealed that isoprene emission at our site was more strongly driven by temperature rather than solar radiation ($r_{tempisoprene}$: 0.8; $r_{solarradiationisoprene}$: 0.5), beyond radiation exceeding hourly values of 100 W m^{-2}. The plot also indicates that the most favourable conditions for isoprene emissions appear to be in the temperature and radiation range of 30-32 ˚C and 450-500 W m^{-2}, respectively.

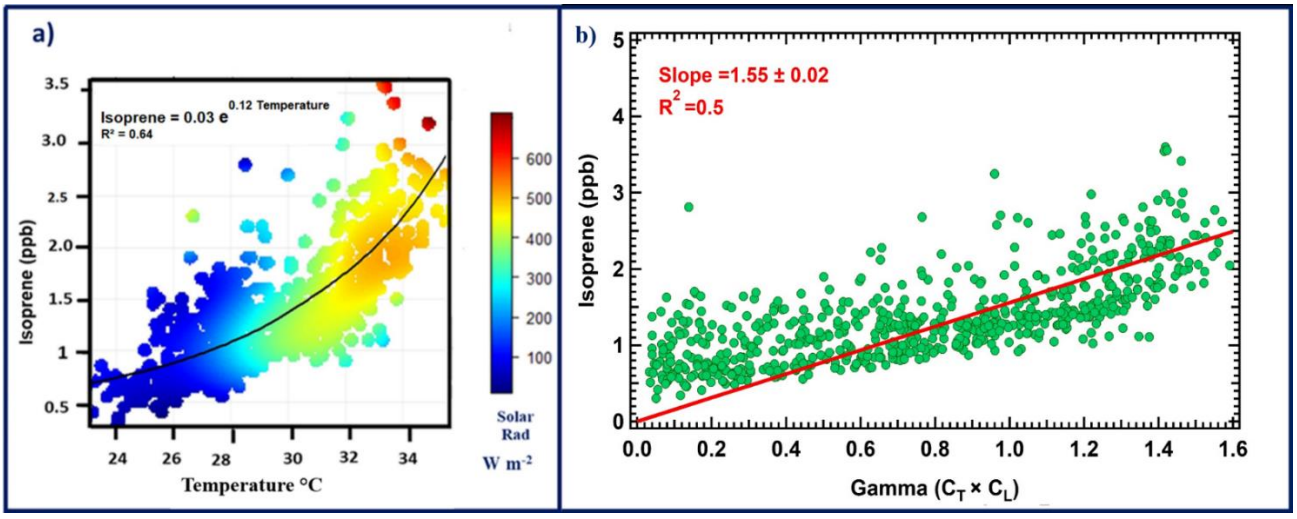

Figure 2.9 a) Correlation of daytime isoprene and ambient temperature color coded with solar radiation data b) Correlation of daytime isoprene mixing ratios with combined temperature and light dependence function (γ) using hourly averaged data (21.07.2012-19.09.2012)

The exponential dependence of isoprene mixing ratios with temperature as revealed by the log linear relationship yielding an exponent value of 0.12 and r^2 of 0.64 (see black fit line in Figure 2.9 a), is quite similar to results reported from forested sites such as Kalogridis et al., 2014 who measured isoprene inside a deciduous forest and obtained a value of 0.13 for the exponent and r^2 of 0.74 at 10 m above ground. Figure 2.9 b further shows the dependence of isoprene mixing ratios on the combined light and temperature parameter similar to the relationship proposed for isoprene fluxes and the combined light and temperature parameter (γ) in Guenther et al. 1995 and as also applied by Kalogridis et al., 2014 for isoprene fluxes, we found a moderate linear correlation even

between isoprene mixing ratios and γ. When this type of analysis is performed on mixing ratios, measurements for low γ values fall significantly above the fit line. This is to be expected, as the relationship is supposed to hold for isoprene emissions fluxes near the source or in a chamber, which would respond to changes in cloud cover rapidly and mixing ratios do not go to zero like emission fluxes. The influence of light and temperature on isoprene mixing ratios was explored by calculating the light and temperature dependence function based on the method in Guenther et al., 1995.

The influence of light and temperature on isoprene concentration was explored by calculating the light and temperature dependence function as described by equations 2.3, 2.4 and 2.5 provided in Guenther et al., 1995. The equations are as follows:

$$\gamma = C_L \times C_T \quad (2.3)$$

Where C_L is the light dependency function defined as:

$$C_L = \frac{\alpha C_{L1} Q}{\sqrt{1+\alpha^2 Q^2}} \quad (2.4)$$

Where Q is the flux of photosynthetically active radiation (PAR- µmol m^{-2} s^{-1}) and α and C_{L1} are empirical coefficients with values equal to 0.0027 and 1.066 respectively. To compute the C_L function PAR values were estimated from measured solar radiation using the conversion factor from plant growth chamber handbook (Franklin, 1998).

The temperature dependence function is defined as:

$$C_T = \frac{exp\frac{C_{T1}(T-T_S)}{RT_ST}}{1+exp\frac{C_{T2}(T-T_M)}{RT_ST}} \quad (2.5)$$

Where *T* is the leaf temperature in Kelvin, T_S is the leaf temperature at standard condition (303 K), *R* is the universal gas constant (=8.314 J K^{-1} mol^{-1}) and C_{T1}, C_{T2}, T_M are empirical coefficients with values 95000 J mol^{-1}, 230,0000 J mol^{-1} and 314 K respectively. To compute the temperature dependence function leaf temperature (T) was assumed to be same as ambient temperature.

Given that mixed agroforestry practices are prevalent over the region of N.W IGP (Sinha et al., 2014), with large area under poplar and eucalyptus, which are high isoprene emitting trees

(Schnitzler et al., 2010), in view of above evidence and analyses, the daytime isoprene therefore appears majorly due to biogenic sources during the monsoon season.

Figure 2.10 shows acetaldehyde as a function of the ambient temperature color coded with the corresponding solar radiation. In the case of acetaldehyde one can note that the high value has greater dependence on radiation (r =0.7) rather than temperature (r=0.5), which is indicative of a significant photochemical production source for acetaldehyde in addition to possible biogenic emissions. We further examine the role of biogenic and photochemical sources on acetaldehyde, formaldehyde and the sum of MVK+MACR.

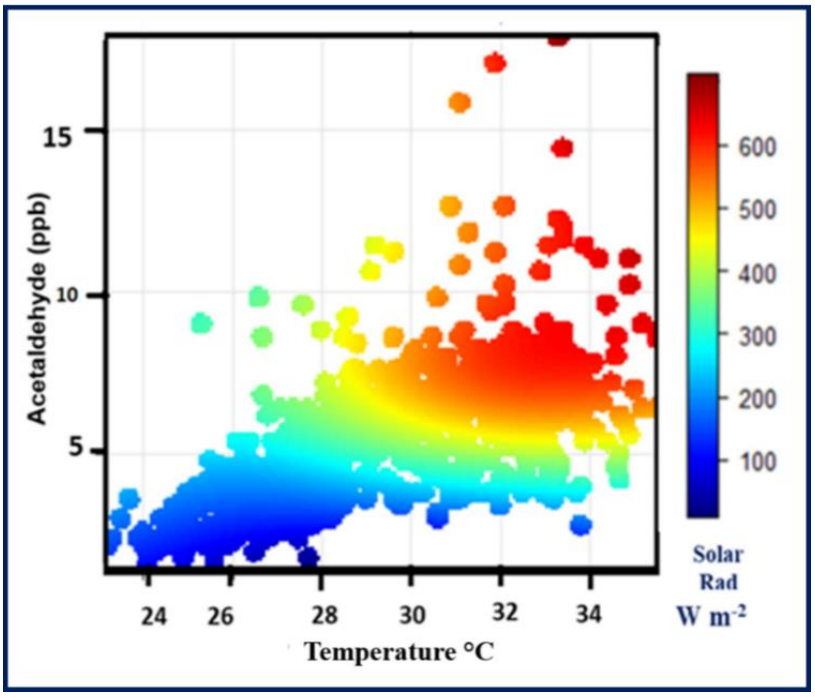

Figure 2.10 Correlation of daytime acetaldehyde and ambient temperature color coded with solar radiation data for the period of study using hourly averaged data (21.07.2012-19.09.2012)

MVK+MACR can be formed photochemically during the oxidation of isoprene by hydroxyl radicals. One molecule of isoprene can yield 0.23 molecules of methacrolein and 0.32 molecules of MVK (Carter and Atkinson, 1996). A more recent laboratory study by Liu et al. 2013 investigated the yields of MVK+MACR from isoprene under both low NO_x and high NO_x conditions. While the yields under low NO_x conditions (< 70 ppt NO) were much lower and ranged as low as 0.1 overall, under high NO_x conditions they were comparable to previous studies and ranged from 0.5 to 0.8. The daytime correlation of the MVK+MACR with isoprene using hourly averaged data showed good linearity (r= 0.6; Figure 6 a) and yielded a slope of 0.5. An average

daytime ratio of MVK+MACR to isoprene of 0.5 is consistent with the measured values of this ratio from isoprene emitting forests (Eerdekens et al., 2009; Karl et al., 2009; Kuhn et al., 2007), and therefore likely suggests that the major source of MVK+MACR during the monsoon season is from isoprene photo-oxidation. The chemistry of isoprene oxidation resulting in production of methyl vinyl ketone and methacrolein proceeds through differing mechanisms in high NOx and low NOx regimes. In low NO_x forested sites, formation of methyl vinyl ketone and methacrolein through alkly peroxy radicals (RO_2) is a significant contributor alongside the NO pathway (Liu et al. 2013), which could explain why we have overall comparable MVK+MACR/isoprene ratios at our suburban site and many other forested sites. Also, while higher ozone in suburban locations could result in higher hydroxyl radical formation, the loss rates from reactive anthropogenic emissions at suburban sites, could lead to steady state OH radical concentrations that do not scale linearly with production from ozone.

The largest global source of acetaldehyde is photo-oxidation of C-2 and higher alkanes and alkenes. According to the molar yield estimates presented in (Millet et al., 2010), the contribution to acetaldehyde production under high NOx regime ranks as follows on a global basis: *n*-butane (98 %) > propene (82%) > ethane (81%) > propane (26%). Isoprene oxidation also results in acetaldehyde production but the contribution to acetaldehyde production is only 1.9%. Acetaldehyde can also be directly emitted as a primary biogenic emission from leaves which is light and temperature dependent (Fall, 2003; Kesselmeier and Staudt, 1999). Figure 2.11 b shows good correlation of acetaldehyde with isoprene in the daytime during the monsoon season (r=0.7) and the slope of 3.9 for acetaldehyde/ isoprene confirms that photochemical production of isoprene expectedly cannot explain most of acetaldehyde abundance. Co-synchronous variability in acetaldehyde mixing ratios and solar radiation was also observed for acetaldehyde (Figure 2.8 b). This suggests the combined influence of photochemical and biogenic sources controlling the daytime ambient acetaldehyde but when combined with information presented so far and in Figure 2.11 (discussed below), it is likely that the photochemical production of acetaldehyde is more important than the biogenic source of acetaldehyde, consistent also with findings of Millet et al. 2010 for several atmospheric environments in the world.

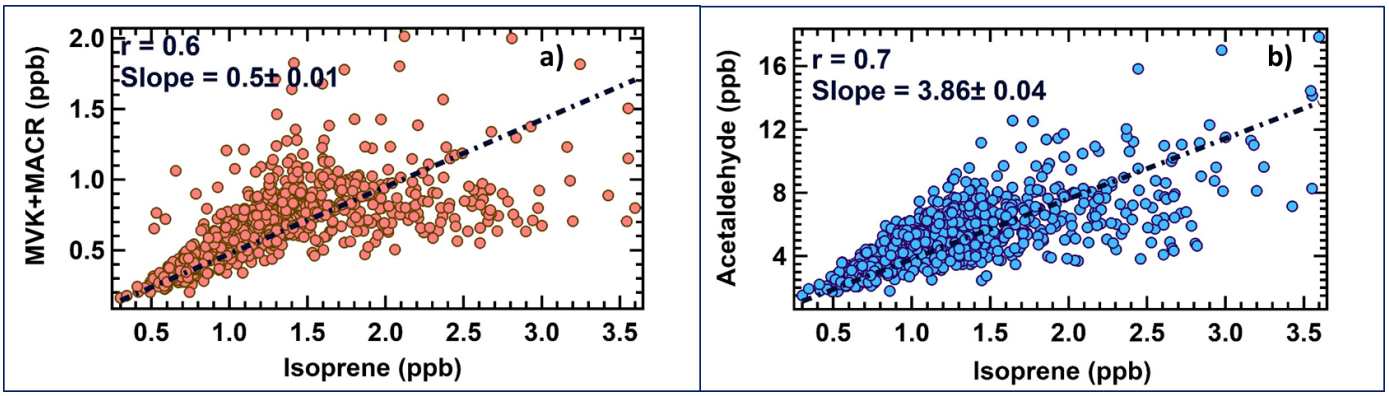

Figure 2.11 a) Correlation of MVK+MACR with isoprene using hourly averaged values during daytime b) Correlation of acetaldehyde with isoprene using hourly averaged daytime data (21.07.2012-19.09.2012)

The major source of formaldehyde is photo-oxidation of hydrocarbons (Fortems-Cheiney et al., 2012; Parrish et al., 2011). However, formaldehyde can also be directly emitted from biomass burning (Lee et al., 1997), industrial activity (Buzcu Guven and Olaguer, 2011) and vegetation (Seco et al., 2008). Among hydrocarbons, isoprene is a dominant formaldehyde precursor (Wolfe et al., 2016) followed by alkenes like ethene, propene, 1-butene and 1,3-butadiene (Parrish et al., 2011). Assuming hydroxyl radical as the prominent oxidant of alkenes producing formaldehyde, the product yield of 1.44 molecules of formaldehyde was estimated from one molecule of ethene and 0.86 molecules from propene (Seinfeld and Pandis, (1998)). From isoprene oxidation at NO_x levels above 1 ppb, which is representative of conditions during this study, the reported yield is greater than 0.9 molecules formaldehyde from 1 molecule of isoprene (Wolfe et al., 2016). Analyses of the daytime hourly averaged formaldehyde with isoprene is shown in Figure 2.12 which showed good correlation (r = 0.6) and yielded a slope of 1.1, consistent with isoprene oxidation being a significant source of formaldehyde.

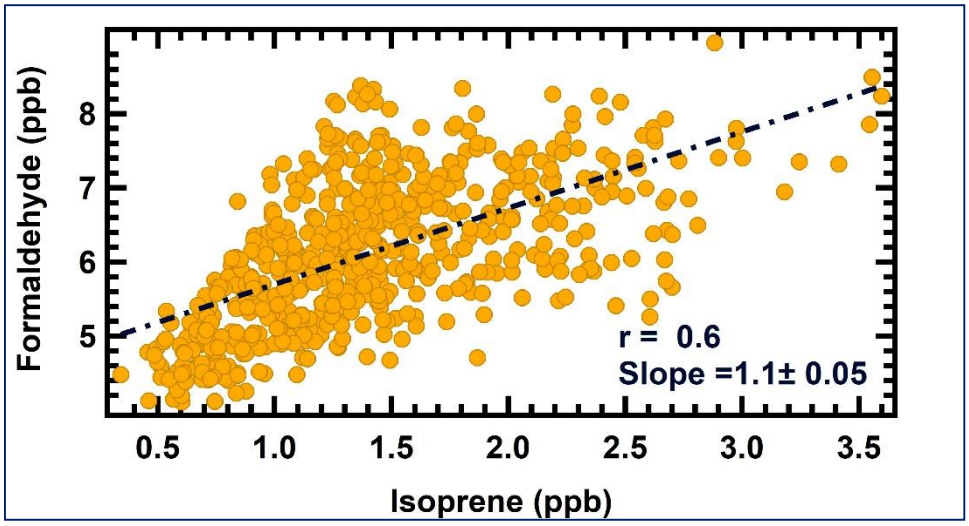

Figure 2.12 Correlation of daytime formaldehyde with daytime isoprene using hourly averaged monsoon time data (21.07.2012-19.09.2012)

In the next sections, we examine the impact of the boundary layer growth and dilution effects on the diurnal profiles of these compounds for additional insights and comparison with the summer season mixing ratios of these compounds.

2.4.3 Boundary layer growth and dilution effect on diurnal variability

The boundary layer grows after sunrise due to radiative heating of the ground which heats the surface air and drives mixing through turbulence, which affects the diurnal variation of chemical compounds due to the dilution effect (van Stratum et al., 2012). Figure 2.13 (a-d) shows the hourly averaged diurnal profile of acetaldehyde, isoprene, formaldehyde and sum of MVK+MACR represented as the mean (solid line), the 25^{th} and 75^{th} percentiles (shaded regions) derived from all measurements (n > 80,000) for the period from 21.07.2012-19.09.2012, with averaged hourly boundary layer height (as dashed lines). The plots in Figure 2.13 (e, f) show the hourly averaged diurnal profiles for temperature, wind speed, and solar radiation for the same period. The Sun rises shortly after 6 am local time and after the first hour of heating the daytime boundary layer grows due to radiative heating from ~100 m at 7 am to ~850 m by 16:00, following which as the thermals weaken, the boundary layer height decreases to ~400 m shortly by sunset. While the solar radiation reaches its diurnal maxima at around 13:00 local time, the temperature reaches its diurnal maxima at 14:00 local time.

Figure 2.13 shows that formaldehyde and acetaldehyde mixing ratios start to increase just after sunrise and by 13:00 local time when radiation peaks, reach their highest values of the day with their mixing ratios showing an increase of 3 ppb and 1.5 ppb, respectively despite the dilution effect due to the growing boundary layer. On the other hand, isoprene mixing ratios start to increase slightly later and reach their maximum values of the day by 14:00 local time when temperature peaks, with the average isoprene mixing ratios increasing from ~1 ppb at 6 am to ~1.6 ppb at 14:00 local time. Isoprene exhibits a lag of 1 hour and 0 hour with solar radiation and temperature respectively, at our measurement site which is similar to previous observations reported within a tropical rainforest (eg. (Jones et al., 2011). This lag can be attributed to a consequence of the strong competition between light dependent isoprene emission and light dependent isoprene destruction, that is reaction of isoprene with photochemically produced hydroxyl radicals. Based on the solar radiation profile the hydroxyl radical would also be expected to peak around l3:00. However rapid sequestering of isoprene by OH could have suppressed ambient concentrations at that time causing a shift in the isoprene maxima. On the other hand, for acetaldehyde and formaldehyde which are less reactive than isoprene with the hydroxyl radicals, the maxima would be expected at 13:00 local time, as was observed. The increase in formaldehyde and acetaldehyde mixing ratios much before isoprene starts to increase suggests that the photochemical production of these compounds is significantly influenced by photo-chemical oxidation of other hydrocarbons in addition to isoprene. The diurnal variation of MVK+MACR is consistent with their formation primarily from isoprene oxidation as their profile trails that of isoprene mixing ratios. However unlike in the study by Kalogridis et al., 2014 who reported a 2 hour lag between rise in isoprene and MVK+MACR mixing ratios at a forested site in France, we did not see a strong lag and we think the reason is that in this moderately high NOx environment (~5 ppb NOx) and monsoon conditions conducive for higher OH radical concentrations due to sufficient ozone, high humidity and radiation (Kumar et al., 2016), the oxidation chemistry proceeds much faster than in sites where tree canopy is denser and does not favour rapid photochemical oxidation.

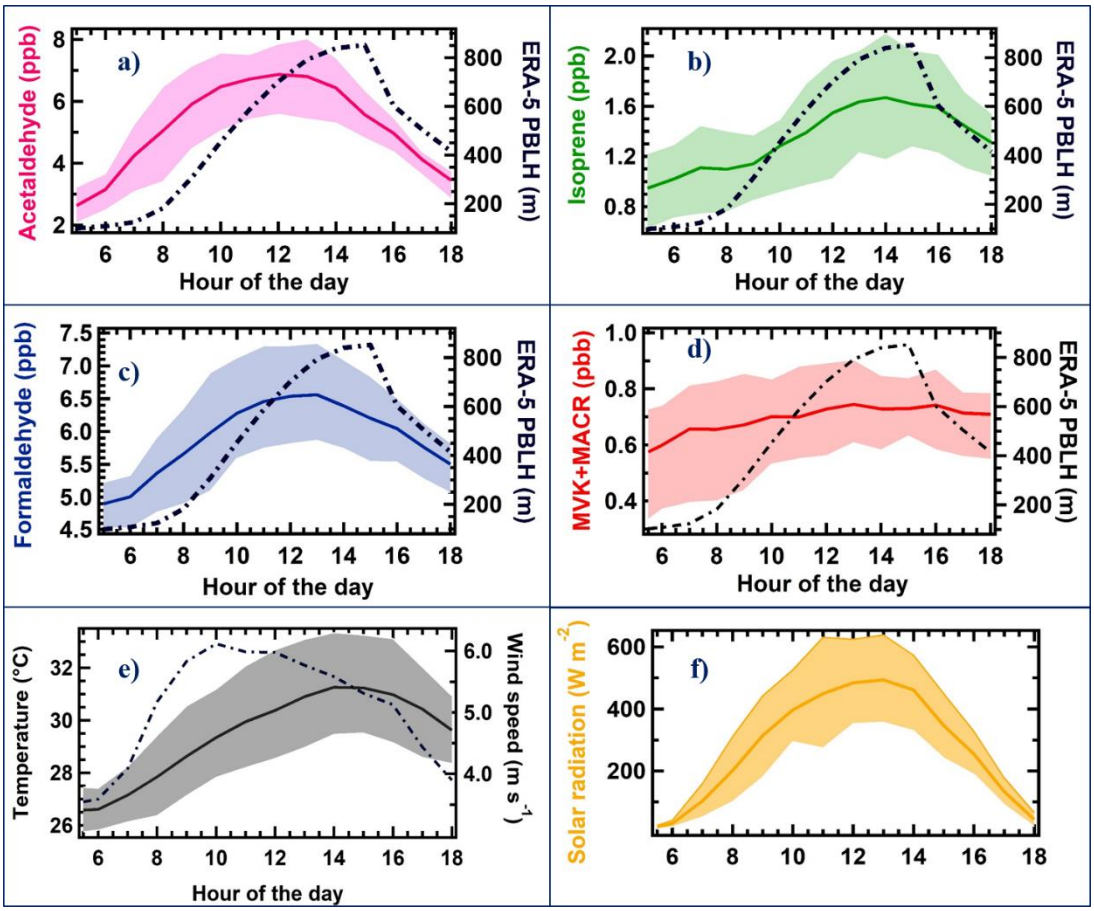

Figure 2.13 Daytime hourly averaged diurnal variation of a) acetaldehyde b) isoprene c) formaldehyde d) sum of MVK+MACR e) temperature and f) solar radiation represented as the mean (solid line), the 25th and 75th percentiles (shaded regions) derived from all measurements for the period (21.07.2012-19.09.2012) with mean boundary layer height (dashed line in sub-panels a to d) extracted from ERA-5 dataset and hourly averaged wind speed (dashed line in subpanel e)

2.4.4 Analyses of diurnal variations in MVK+MACR/Isoprene ratios

Figure 2.14 presents the diurnal variations in ratios of MVK+MACR to isoprene which are very helpful to assess the oxidation of isoprene. The yields of isoprene oxidation products are known to strongly depend on the ambient levels of NO_x. Very low ratios of MVK+MACR/ isoprene of 0.1 to 0.13 have been reported in low NO_x regimes (NO < 70 ppt) in a laboratory study (Liu et al., 2013) and a field study (Kalogridis et al. 2014) (NO < 30 ppt), while much higher ratios of 0.3-0.75 (Holzinger et al., 2002) have more commonly been observed in higher NO_x regimes. In addition to the NO_x regime, the time available for isoprene oxidation in ambient air before the air is sampled is also important and could influence the observed ratios. During our study the daytime NO_x was not as low as that observed in a Mediterranean forest by Kalogridis et al. 2014, with

average NO_x during daytime circa 5 ppb (NO> 1 ppb) as reported in Kumar et al., 2016. Thus, it is not surprising that the observed MVK+MACR/ Isoprene ratios were 0.54 ± 0.04 and in line with expected yields under high NO_x regimes including by Liu et al. 2013 of 0.5 -0.8 for MVK+MACR.

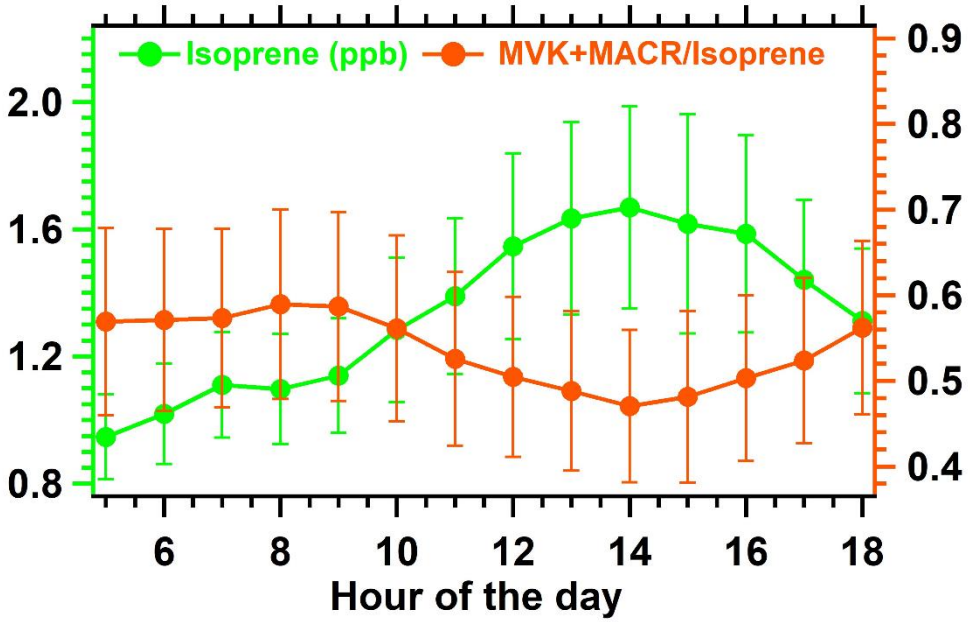

Figure 2.14 Daytime hourly averaged diurnal variation of the ratio of MVK +MACR to isoprene (vertical bars represent ambient variability as standard deviation)

2.5 Comparison of isoprene, acetaldehyde and isoprene oxidation products during monsoon and summer season based on mass concentration

The pie-chart in Figure 2.15 presents a summary of day time average fractional contributions of isoprene, acetaldehyde, formaldehyde and MVK+MACR for the months of monsoon and summer. The total mass concentration due to these compounds are 20.9 µg m^{-3} and 13.6 µg m^{-3} for monsoon and summer respectively. The relative contribution of each of the individual species for monsoon and summer season are isoprene (M:3.6 ± 1.7 µg m^{-3}) (S:3.1 ± 1.5 µg m^{-3}), formaldehyde (M:6.1 ± 1.40 µg m^{-3}) (S:4.6 ± 1.3 µg m^{-3}), acetaldehyde (M:9.3 ± 3.5 µg m^{-3}) (S: 4.5 ± 2.4 µg m^{-3}), MVK+MACR (M:1.9 ± 0.9 µg m^{-3}) (S:1.6 ± 0.9 µg m^{-3}) where M stands for monsoon and S stands for summer season respectively. The analysis shows higher mass concentrations for all the species

during the monsoon season, with the acetaldehyde mass concentration in monsoon season twice as high as the summer season. The main factor responsible for the observed differences in summer and monsoon season is the dilution effect due to the ventilation coefficient (ventilation co-efficient is the product of boundary height and wind speed). The average ventilation coefficient during daytime hours was 5900 m^2 s^{-1} in summer and 1445 m^2 s^{-1} in monsoon season, which is four-fold higher. Thus, despite the presence of additional emission sources in summer such as crop residue biomass burning which was reported by Sinha et al., 2014, the lower monsoon season ventilation coefficient, resulted in higher mixing ratios and mass concentrations for the oxygenated compounds during monsoon season, despite lower radiation compared to summer.

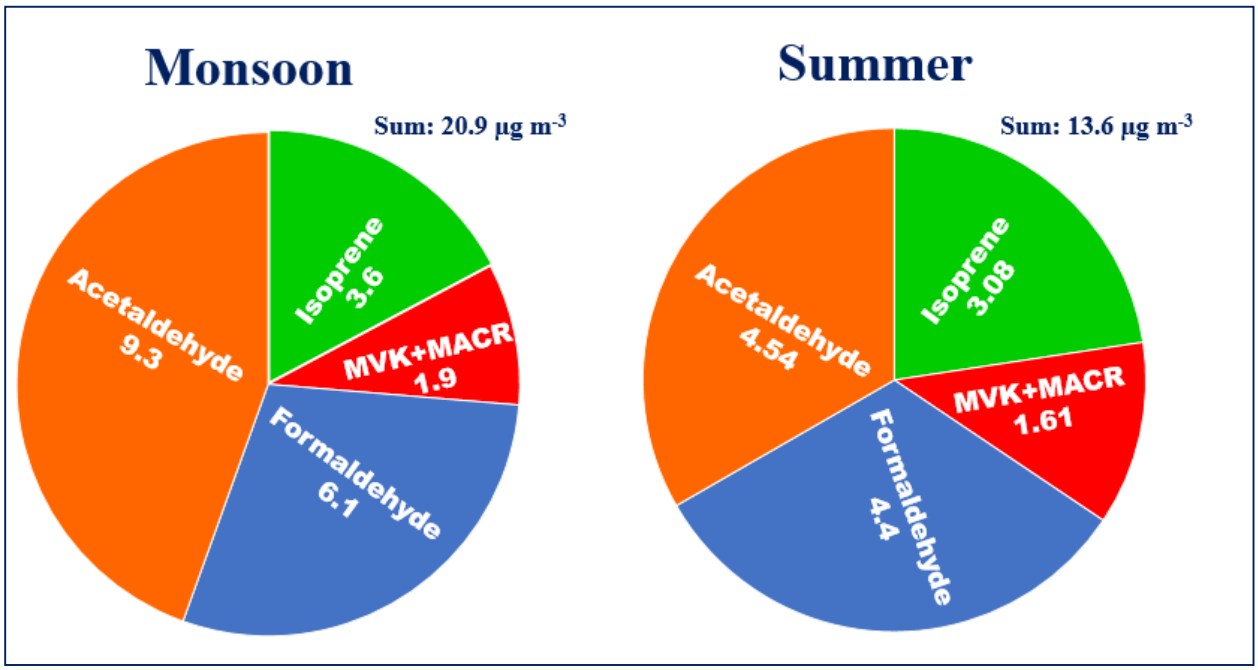

Figure 2.15 Pie chart showing the mass concentration contributions of isoprene, formaldehyde, acetaldehyde and MVK+MACR for summer (01.05.2012-31.05.2012) and monsoon (21.07.2012-19.09.2012).

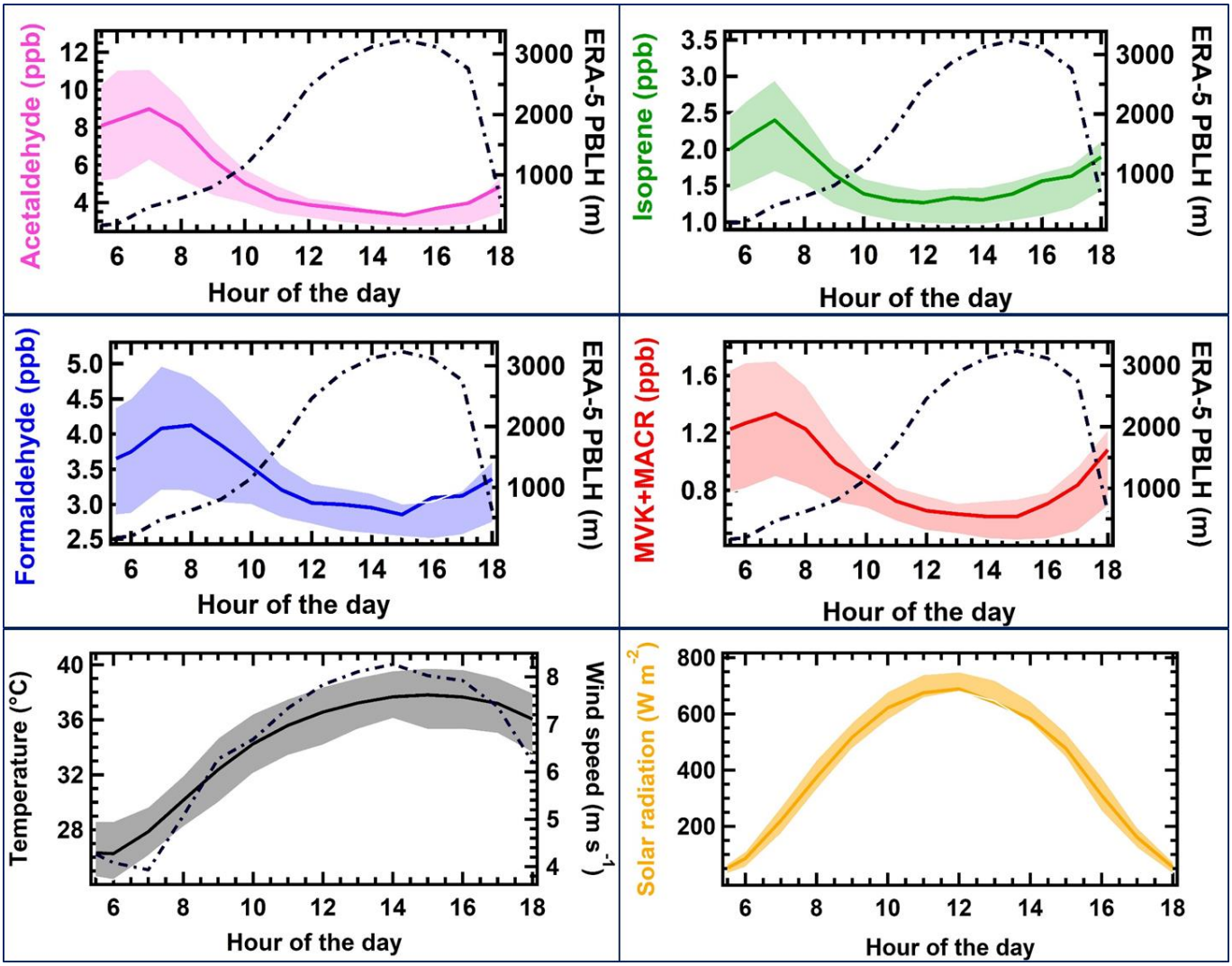

Figure 2.16. Daytime hourly averaged diurnal variation of a) acetaldehyde b) isoprene c) formaldehyde d) sum of methyl vinyl ketone and methacrolein (MVK+MACR) e) temperature and f) solar radiation represented as the mean (solid line), the 25th and 75th percentiles (shaded regions) derived from all measurements for the period (01.05.2012-31.05.2012) with mean boundary layer height (dashed line in sub-panels a to d) extracted from ERA-5 dataset and hourly averaged wind speed (dashed line in subpanel e)

2.6 Conclusion

This study presents the first monsoon time dataset of isoprene, MVK+MACR, formaldehyde, and acetaldehyde from India. Although the analyzed dataset is from the year 2012, due to continued similar land use and agroforestry practices as well as similar monsoon season meteorology every year, the findings have great contemporary relevance. The influence of biomass burning sources was found to be negligible /absent when compared with summertime conditions at the same site. Further, it was found that biogenic emissions were the major source of isoprene with photo-oxidation of isoprene also the major source of MVK+MACR. Formaldehyde and acetaldehyde have strong photo-chemical sources from oxidation of hydrocarbons, including isoprene. High daytime isoprene was driven primarily by ambient temperature similar to the dependency observed from a tropical rainforest site. Agroforestry cultivation of poplar, eucalyptus (high isoprene emitting trees), which are grown ubiquitously on agricultural fields peripheries over the N.W IGP are the likely sources. The relative contribution of the individual species (isoprene, acetaldehyde, formaldehyde, MVK+MACR) for monsoon and summer season revealed significantly higher mass concentrations for the month of monsoon for these compounds due to the effect of lower ventilation coefficient in monsoon relative to summer.

Future work should focus on constraining the spatial and temporal distribution of biogenic sources of isoprene and photochemical sources of formaldehyde and acetaldehyde over the Indo-Gangetic Plain for better understanding of environmental pollution feedbacks. Tackling the industrial and anthropogenic sources for other abundant VOCs such as methanol and acetone will also be crucial. Such efforts will assist development of improved emission inventories for air quality and atmospheric chemistry models, to mitigate phytotoxic exceedance of 40 ppb ozone that is harming rice yields in this major rice growing region of the world, which is also strategic for the upper atmospheric chemistry since it acts as conduit for surface emissions to influence the remote upper troposphere during the monsoon season.

This chapter sets the foundation for next chapter of my thesis where the WRF-Chem a state of the art chemical transport model was configured over N.W IGP to study regional atmospheric chemistry.

Chapter: 3

Model setup: Weather research and forecasting model coupled with chemistry

3.1 The WRF-Chem model

This chapter presents a general background to mathematical modelling followed by a detailed description of the WRF-Chem model which was setup for north India and has been used in this thesis work. This thesis work utilizes a fully coupled online 3D chemical transport model WRF-Chem to study 3D simulations of biogenic isoprene over South Asia the details regarding the modelling system will be discussed next.

To understand regional scale atmospheric chemical composition, we need a combination of relatively fine resolution, detailed chemistry representation and online coupling between different parts of the model (Zhang et al., 2009). The WRF-Chem model is a prime example of new generation chemical transport model which is capable of simulating the temporal and spatial distribution of trace gases and aerosols simultaneously along with meteorology (Fast et al., 2006; Grell et al., 2005). The fully online and consistent nature of WRF-Chem enables to use same set of schemes for physics, transport, sub-grid scale transport along with same horizontal, vertical grids and time steps. The online nature of model allows for the feedbacks between chemistry and meteorology but it comes at a computational cost. WRF-Chem has been developed with collaborations among different institutions and University scientists over the past decade (https://ruc.noaa.gov/wrf/wrf-chem/). The WRF-Chem model has been used extensively to simulate numerous case studies and applications over South Asia (Ghude et al., 2013; Kumar et al., 2014a; Kumar et al., 2014b; Ojha et al., 2016) but till date but till date none of the studies have evaluated the representation of biogenic volatile organic compounds over the region. Here, I have configured the WRF-Chem model domain over N.W-IGP and this chapter describes the model configuration specific to this study with some details on the complete modeling setup. The technical details about the model setup has been discussed in appendix 1. Additional, details can be obtained from the WRF-Chem user guide (https://ruc.noaa.gov/wrf/wrf-chem/Users_guide.pdf). A 1000 x 1000 km^2 domain centered on 30.667° N, 76.729° E with

horizontal grid of 10 km and 51 vertical levels (surface up to ~10 hPa) was set up. The following model simulations were performed using WRF-Chem.

1. Default: Default configuration of the model without aerosol-radiation feedbacks

2. Improved: Improved model configuration with the modified tree cover of 10% in croplands both in the MEGAN and in the Noah land surface module without aerosol-radiation feedbacks.

3. Improved with aerosol feedback: Improved model configuration with the modified tree cover of 10% in croplands both in the MEGAN and in the Noah land surface module with aerosol-radiation feedbacks on.

4. Hypothetical 50% tree cover: Model configuration with a modified tree cover of 50% in croplands both in the MEGAN and in the Noah land surface module without aerosol radiation feedbacks. We calculate this scenario assuming that areas presently identified as cropland will be planted with 25% broadleaf evergreen trees (e.g. citrus, guava, litchi, mango, olive), 25% broadleaf trees (e.g. poplar, teak) and 40% crops and will retain 5% shrubs, 3% grasslands and 3% urban and build-up area.

The results from these different sensitivity studies will be discussed in much greater detail in chapter 4. Next I discuss the model initialization, emissions, chemistry and different parametrizations of WRF-Chem model.

3.2 Real data initialization: Meteorology

The real data initialization program is the second step of the WRF modeling system which begins after completion of the WRF pre-processing system. In this step of the model initialization process, the WRF model computes a reference state of the atmosphere for the column pressure and geopotential. The real program calculates the perturbations from the base state for column pressure and geopotential to initialize the two components of wind (u, v), potential temperature and water vapor mixing ratio meteorological variables. It is to be noted that the WPS program deals completely in 2D data structure by interpolating the data in 2D grid structure while the real program is involved in 3D interpolation of the data field. The 3D interpolation is achieved by defining a vertical coordinate system in the program. The current setup of the model used in this study uses a terrain following hydrostatic pressure coordinate system defined as:

$$\eta = \frac{P_h - P_{ht}}{P_{hs} - P_{ht}} \qquad 3.1$$

The main advantage of using the terrain following coordinate system is the treatment of surface topography. In the above equation P_{hs} is the pressure at the surface of the earth (which varies with the topography), P_{ht} is the pressure at the top or highest level of the model and P_h is the pressure at that particular level. This definition of the vertical coordinate system was proposed by (Phillips, 1957) where the model top was considered as the top of the atmosphere which was further improved by (Laprise, 1992)**.** The η value varies from 1 at the surface to 0 at the top of the atmosphere as shown in Figure 3.1. In this study the modeling domain was divided into 51 vertical levels from the surface.

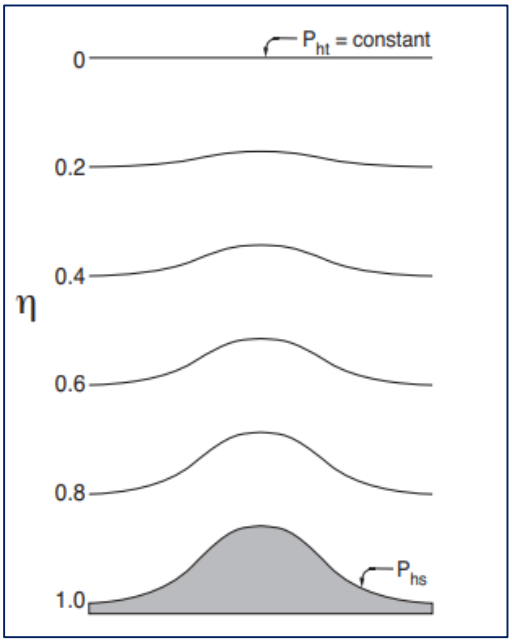

Figure 3.1 Schematic of the terrain following η coordinate system (Adopted from WRF ARW NCAR technical notes-(Skamarock et al., 2008)).

The η or the 51 vertical levels between surface and 10 millibar (approximately 30 km) and values correspond to these 51 levels are: 1.00000, 0.99381, 0.98643, 0.97786, 0.96815, 0.95731, 0.94538, 0.93122, 0.91490, 0.89653, 0.87621, 0.85405, 0.82911, 0.80160,0.77175, 0.73981, 0.70509, 0.66798, 0.62889, 0.58823, 0.54957, 0.51281, 0.47788, 0.44471, 0.41323, 0.38336, 0.35503, 0.32819, 0.30276, 0.27869, 0.15963, 0.14352, 0.12836, 0.11410, 0.10070, 0.08811, 0. The reason for keeping the model top level so high was mainly due to tall mountains (the great Himalayas)

which were in the modeling domain, so the stratosphere is relatively closer to the ground in those areas. Therefore, we need to give space for interaction of troposphere and stratosphere. Additionally, model tops can reflect back waves which will be reduced in case of a higher model top pressure. The plot in Figure 3.5 b shows the vertical grid structure in the modeling setup at 30° latitude. The current vertical structure has been defined in such a way that within the lowest 1 km layer we have 10 levels which has been designed in such a way to represent the planetary boundary layer and processes at a higher resolution.

3.2.1 CFL condition

The atmospheric chemistry models solve the continuity equation which evolve with time which is non-linear and cannot be solved analytically. Therefore, to find approximate solution ARW solver is used by the WRF model which numerically integrates the equation by using a third order time split Runge-Kutta (RK3) scheme as described by (Klemp et al., 2007; Skamarock and Weisman, 2009; Wicker and Skamarock, 2002)**.** This integration is carried out using a fixed time step which has to be defined by the user during initialization of the model. The parameter used to define dynamic stability of the solver is known as CFL (Courant-Fredrichs-Lewy Condition) (Courant* et al., 1928)**.** The dimensionless courant number C_r is defined using the wind-fields (u, v, w) and resolution (▲x, ▲y, ▲z and ▲t) for each of the grid boxes is given by equation 3.2.

$$C_r = u \times \frac{\blacktriangle t}{\blacktriangle x} \qquad 3.2$$

Where, u is the horizontal wind speed along direction of x, and ▲x is the horizontal model resolution. The condition $C_r < 1$ has to be maintained for dynamic stability. Sometimes, while exploring deep convection or during the monsoon season w and ▲z should be considered. One of the rule of thumb for preventing instabilities is ▲t = 6*▲x. In this study the horizontal model resolution was set at 10 km and the time step used was 60 seconds.

3.3 Real data initialization: Emissions

It would be really challenging to make valid prediction of chemical transport and transformation of atmospheric constituents without suitable emissions to evolve from. Therefore, after the initialization of the meteorological variables in the next step the real data initialization program

includes the biogenic, anthropogenic and biomass burning emissions of chemical species in the model. Each of these emissions will be discussed in the next section.

3.3.1 Biogenic emissions

The current version of WRF-Chem model uses Model of emissions of gases and aerosols from nature (MEGAN) 2.04 version (Guenther et al., 2006). The framework used by MEGAN model is discussed next. The following equations have been adopted from (Guenther et al., 2006).

$$EM = € \times \gamma_{CE} \times \gamma_{age} \times \gamma_{SM} \times \rho \quad 3.3$$

$$\gamma_{CE} = \gamma_T \times \gamma_P \times \gamma_{LAI} \quad 3.4$$

Where, EM is the emission in units (µg m^2 h^{-1}), € is the emission factor in units (µg m^{-2} h^{-1}), γ_{CE} is the canopy factor, γ_{age} is the leaf age factor, γ_{SM} is the soil moisture factor. P is the loss and production within canopy, γ_T is the temperature factor, γ_P is the photosynthetic photon flux density (PPFD) factor and γ_{LAI} is the leaf area index factor. The current algorithm of WRF-Chem model doesn't take γ_{SM} *and* ρ in the calculations they are set to 1.0. Next, I discuss the temperature and light sensitivity used by the MEGAN model.

$$\gamma_T = E_{opt} \times C_{T2} \exp((C_{T1} \times x)/ C_{T2} - C_{T1}(1 - \exp(C_{T2} \times x))) \quad 3.5$$

$$x = [(1/T_{opt}) - (1/T_{hr})]/0.00831 \quad 3.6$$

$$T_{opt} = 313 + +(0.6 \times (T_{240} - 297)) \quad 3.7$$

$$E_{opt} = 1.75. \exp(0.08(T_{daily} - 297)) \quad 3.8$$

Where, T_{hr} is hourly average temperature T_{daily} is daily average temperature in kelvin representative of simulation period, C_{T1} (=80) and C_{T2} (=200) are empirical coefficients and T_{240} is the temperature for past 240 hrs. The γ_P is the photosynthetic photon flux density (PPFD) factor which is computed from the following equations (Guenther et al., 2006).

$$\gamma_p = 0 \quad \sin(a) <= 0 \tag{3.9}$$

$$\gamma_p = \sin(a) * [2.46*0.9*\varphi^3 (1+0.0005(P_{daily} -400))] \tag{3.10}$$

$$\text{For, } 0 < \sin(a) < 180 \tag{3.11}$$

$$\varphi = \frac{\text{Pac}}{(\sin(a)*\text{PToa})} \tag{3.12}$$

$$P_{TOA} = 3000 + 99 * cos\left(2 * 3.14 - \left(DOY - \frac{10}{365}\right)\right) \tag{3.13}$$

$$P_{ac} = \text{SRAD}* 4.766 * 0.5 \tag{3.14}$$

Where, a is the solar angle in degrees, P_{daily} is the daily average PPFD measured in µmol $m^{-2}s^{-1}$, P_{Toa} is the PPFD at the top of atmosphere, P_{ac} is the above canopy PPFD, DOY is the day of the year. The schematic in Figure 3.2 shows the algorithm used by MEGAN model to compute isoprene emissions. The model estimates the isoprene emission factor from an input file which is at a spatial resolution of 1 km^2. Next, the isoprene emission factor which is mapped to the regional

modelling domain is subjected to adjustment factors discussed above to compute the actual isoprene emission at each of the grid points.

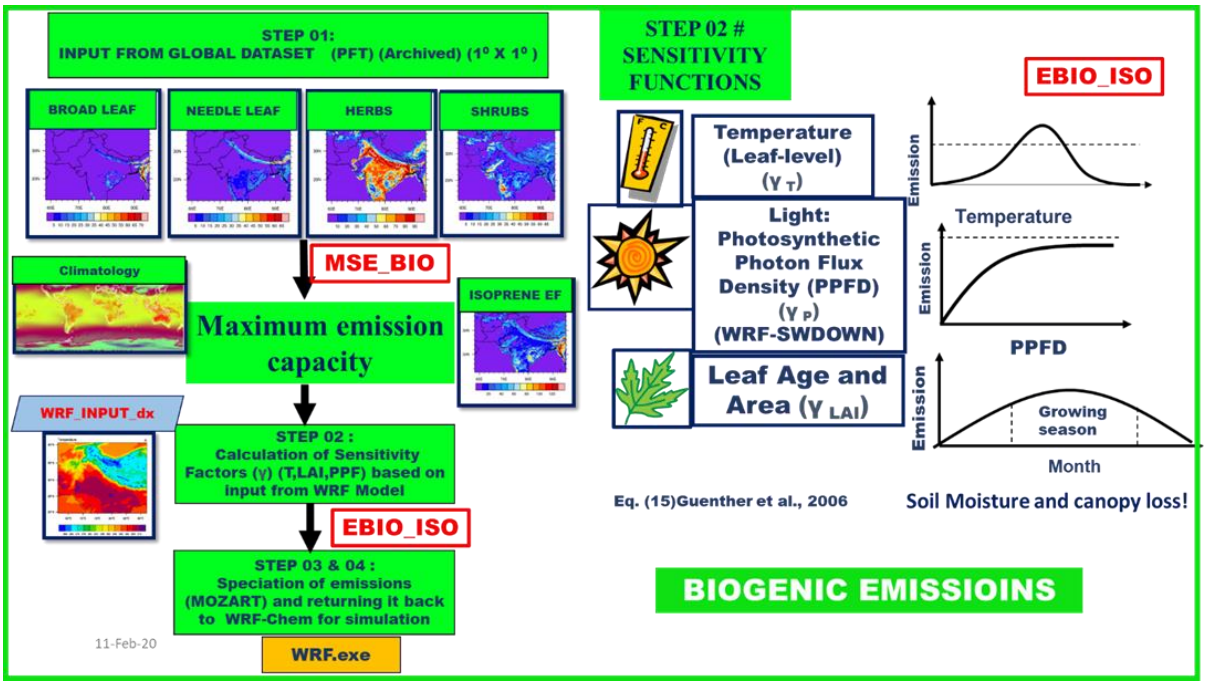

Figure 3.2 Schematic of the MEGAN model algorithm.

The MEGAN algorithm explained above requires accurate estimation of land-cover which includes distribution of plant functional types (PFTs) namely (vegetative surface) broadleaf trees, needle-leaf trees, shrubs, herbs and (non-vegetative surface) bare ground or water (Guenther et al., 2006). The PFTs used by MEGAN model are developed using a variety of inputs including satellite observations, vegetation inventories, ecosystem models and vegetation maps. The plot in Figure 3.3 shows different PFTs and their corresponding global fractions used by the current MEGAN model.

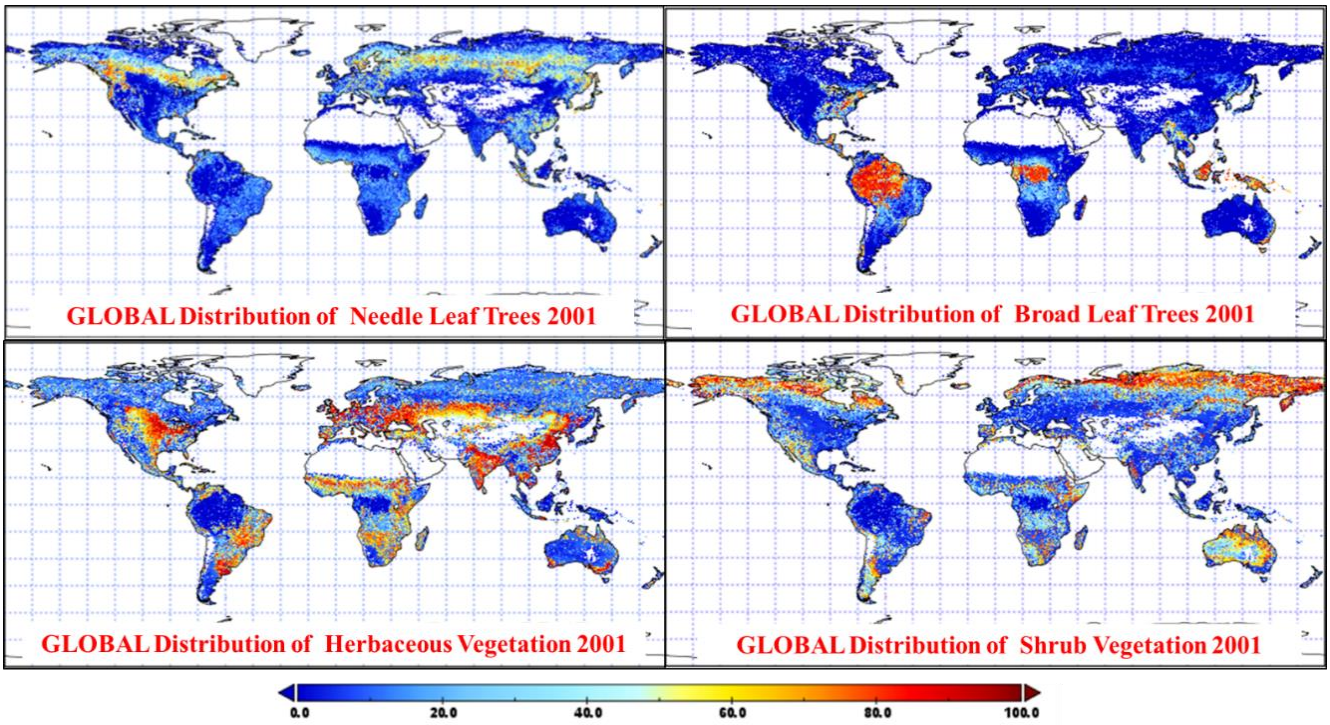

Figure 3.3 Global distribution of vegetation fraction of needle leaf, broad leaf, herbs and shrub vegetation classes used by MEGAN model.

3.3.2 Anthropogenic emissions

Next, I discuss the anthropogenic emissions used by the WRF-Chem model. The anthropogenic emissions are defined as 4D arrays (i, j, k, time) for each emitted species which are defined in the Registry file of the WRF-Chem model. The emissions are specified as moles km^{-2} hr^{-1} for trace gases and as µg m^{-3} for aerosols. These flux values are then converted to ppm using as the model solves all the chemistry in parts per million concentration level.

In this study EDGAR v4.3.2 (emission database for global atmospheric research (EDGAR v4.3.2)) was used which provide global gridded emissions for CO, NO_x, SO_2, NMVOC, PM_{10}, $PM_{2.5}$, BC and OC. This gridded global dataset is mapped to the regional modelling domain using anthro_emiss pre-processor (https://www2.acom.ucar.edu/wrf-chem/wrf-chem-tools-community). These global gridded emission inventory datasets are prepared by accounting for different sources of anthropogenic emissions and include industrial, transport, heating waste and cooking. These emissions are estimated by multiplying an emission factor with activity data/factor.

The total anthropogenic emissions for each of the species are segregated into different sectors for EDGAR v4.3.2 inventory and is representative for the year 2012.

The data tabulated in Table 3.1 and 3.2 shows % contribution of each sector to the total anthropogenic emissions for different trace gas species and NMVOCs over the modelling domain EDGAR v4.3.2 emission inventory. If we analyze the sectorial variability for different species for EDGAR v432 the domestic % contribution which represents biofuel burning in cooking stoves is identified as the highest contributor to the CO (58.6, 44.8) and NMVOC (47.3, 39.2) emissions. For NO_x the contribution is mainly dominated by transport and power sector. For SO_2 the contribution is mainly dominated from power sector and industry where the primary source is SO_2 produced from coal used as fuel in industries and power plants. For NH_3 the contribution for both the emission inventories is mainly dominated from the agricultural sector which includes emission from cattle feedstock, manure management etc.

Table 3.1 Comparison of annual average anthropogenic emissions (Gg per year) for CO, NO_x, NMVOC and SO_2 over the modeling domain.

Species	EDGAR v4.3.2
CO	2.0
NOx	0.14
NMVOC	0.38
SO_2	0.18
NH_3	0.30

Table 3.2 Annual total anthropogenic CO, NO_x, NMVOC and SO_2 emissions over the modeling domain and different source categories to total emissions.

species	Total EDGAR v4.3.2	Percentage contribution				
		Domestic	Industry	Power	Transport	Agriculture
CO	2.0	44.8	9.9	0.05	27.9	16.9
NOx	0.14	7.1	13.6	27.9	37.1	12.9
NMVOC	0.38	39.2	38.9	0.3	16.4	5.3
SO_2	0.18	2.2	24.5	61.1	11.1	1.1
NH_3	0.3	6.7	1.8	0.1	1.4	90

3.3.3 Biomass burning emissions

In this section I discuss about the representation of open biomass burning emissions in WRF-Chem. Open biomass burning contributes significantly to the global emission of aerosols, trace gases and in particular BC (Bond et al., 2004). The variable nature of biomass burning depending on its geographical location and time of the year makes compilation of fire emissions database extremely challenging.

Different studies over different parts of the globe have shown that biomass burning is extremely variable both temporally and spatially differing from continents to biomes, showing a strong interannual as well as diurnal variability (Chandra and Sinha, 2016; Kumar et al., 2016a; Sarkar et al., 2013; van der Werf et al., 2006).

The development of fire emissions was built on the premise of locating individual fires which are detected by remote sensing instruments Moderate Resolution Imaging Spectroradiometer (MODIS). MODIS was launched by National Aeronautics and Space Administration (NASA) on the polar orbiting Earth observatory System (EOS) and is calibrated, processed using atmospheric correction, cloud screening and geographical location. The MODIS instrument has 2 channels (21 and 22) at wavelength band 4μm which is used for global fire detection (Kaufman et al., 1998)

where channel 22 is saturated at 331K and is relatively less noisy in comparison to channel 21 which is saturated at 500K and is not affected by water vapor and gas absorption (Giglio et al., 2003). The channel 21 is also used when there is missing data from channel 22 (Giglio et al., 2003). The algorithm for fire detection functions by scanning the fire pixels in the satellite data and detection of threshold of active fires using brightness temperature which are defined as the pixels with a significant increase in the radiance at the 4μm spectral band, combined with 4μm being stronger than 11μm spectral band. The algorithm further examines each MODIS swath-based fire masks (date, time and location) and makes different categorical dataset including water, cloud, missing data, non-fire and unknown. This categorical data set is used to identify fire pixels through two different logical paths namely: single absolute threshold test and multiple absolute threshold test. The second one is designed to identify majority of active fire pixels in the satellite swath. Any false alarm and cloud is detected using brightness temperature for 250-m red and near-IR channel whereas water induced false alarms are detected by 2.1μm band (Giglio et al., 2003).

As traditional bottom up inventories the biomass burning estimates are computed using product of emission factor (An estimate of the emission of that species per unit mass of fuel burned) EF_{veg}^{i} (Andreae and Merlet, 2001) with estimation of mass of burned biomass which is estimated from the product of burned area A_{Fire} with a density factor α_{veg} and burning efficiency β_{veg} as shown in equation 3.15.

$$M^{i} = \alpha_{veg}\, \beta_{veg}\, EF_{veg}^{i}\; A_{Fire} \qquad 3.15$$

The value of α_{veg} and EF_{veg}^{i} are dependent on the land cover classification while β_{veg} depends on the tree cover/vegetation type. The fuel loading for each pixel showing fire data as detected by MODIS fire count is determined from global land cover dataset for the year 2000 (Latifovic and Zhu, 2004) which describes the vegetation type, land use type and % vegetation cover. The plot in figure 3.26 shows MODIS Vegetation continuous field product which provides the information on type of vegetation at 500m (Hansen et al., 2000) which is overlaid on GLC2000 land cover characterization map to compute fuel loadings and distribution of vegetation at each pixel. The burning efficiency β_{veg} for herbaceous and woody fuels is estimated using the algorithm described

by (Ito and Penner, 2004). The emission factor EF_{veg}^{i} for different vegetation classes is adopted from (Akagi et al., 2011; Wiedinmyer et al., 2011). The plot in Figure 3.4 shows the global distribution of vegetation class used by the NCAR FINN biomass burning emission inventory. During the month of August monthly averaged variation of total biomass burning emissions (Gg/day) of different gaseous and VOC species over the modeling domain from NCAR Finn inventory was estimated to be CO (1.6), NO_x (0.07) SO_2(0.004), NH_3(0.05) and NMVOC (0.4).

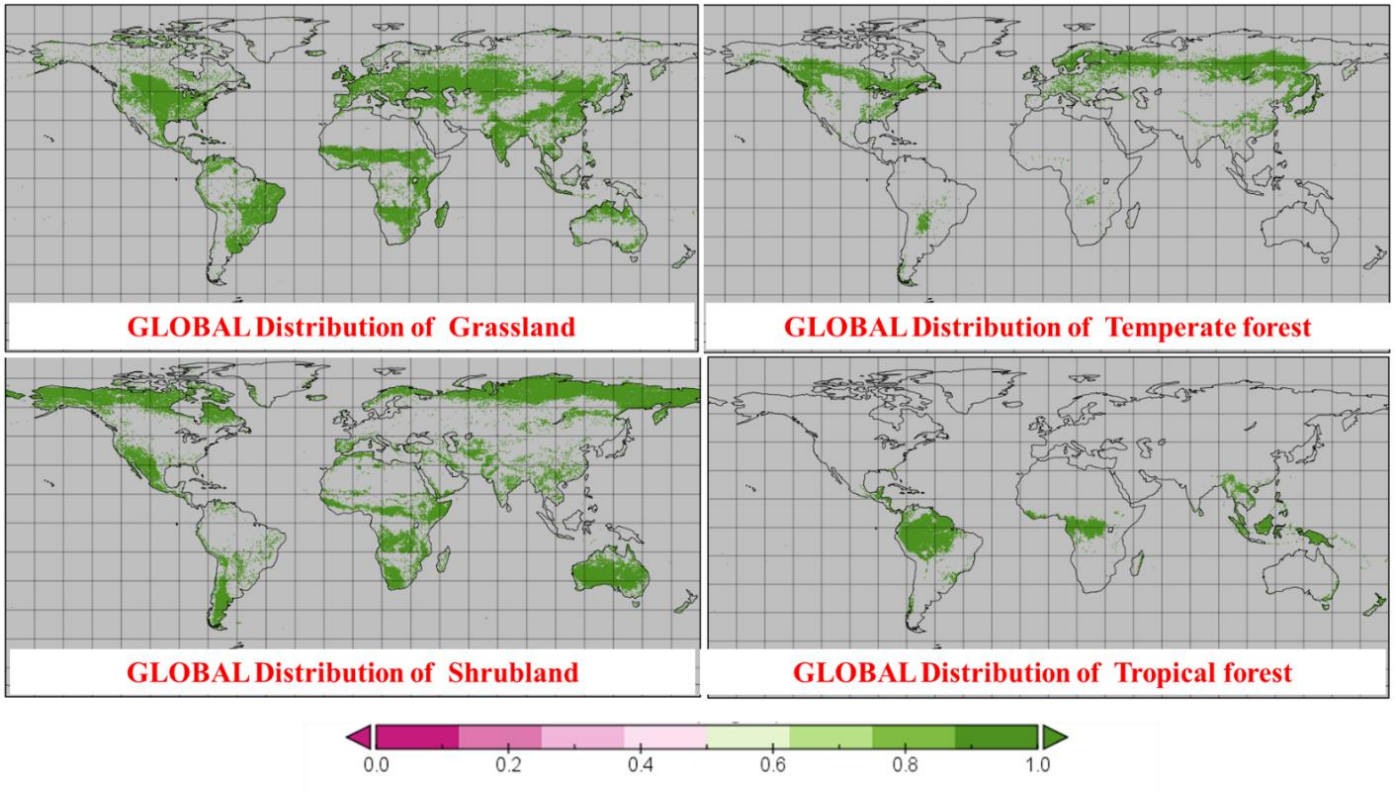

Figure 3.4 Global distribution of vegetation fraction of needle leaf, broad leaf, herbs and shrub vegetation classes used by NCAR Finn inventory.

3.4.4 Natural and mechanical emissions

The natural emissions for dust and sea-salt in WRF-Chem is not represented using emission inventories. Instead they are calculated using mechanistic algorithms which are based upon land/ocean surface characteristics and wind speed at anemometer height (10m) (Skamarock et al., 2008). The dust emission flux in WRF-Chem are calculated as a function of wind, soil-type and moisture using the (Chin et al., 2002; Ginoux et al., 2001) parametrization scheme. This scheme

calculates fraction of erodible mass in each grid cell for different fractions of dust represented as bins along with using land surface types and topological features. During the monsoon season due to wet conditions dust emission is negligible over north India.

3.4 Model chemistry

The WRF-Chem model has several options for using different gas-phase chemistry mechanisms, including Regional atmospheric chemistry mechanism [RACM], Regional acid deposition model [RADM] (Stockwell et al., 1990), Carbon bond mechanism –version 4 [CB-4] (Simonaitis et al., 1997), State-wide air pollution research mechanism of 1999 [SAPRAC99] (Carter, 1994), Carbon bond mechanism [CBM-Z] (Zaveri and Peters, 1999) and Mozart mechanism (Emmons et al., 2010). This study used Mozcart mechanism which is a combination of Mozart and Gocart scheme.

3.4.1 Gas-phase Chemistry and photolysis scheme

This study utilizes Mozart gas phase chemistry which was build up using the KPP (Kinetic Pre-Processor) (Damian et al., 2002). The advantage of compiling WRF-Chem model with KPP is it gives a simplified approach to add a new chemical species to the WRF-Chem registry. It computes evolution of chemical species with time as per the user defined chemical mechanism (the selected mechanism while simulation Chem_Opt in Namelist.input). In WRF-Chem model the addition of chemical mechanisms is accomplished in WRF-Chem Registry file (Registry.WRF-Chem), the user also needs to set the WRF_KPP option in the bashrc file during the model compilation to activate KPP. Simulating WRF-Chem chemistry with KPP gives not only an advantage of higher numerical efficiency but also gives flexibility in addition of new chemical species and equation (Ahmadov, 2012). After compilation KPP input files for chemistry mechanisms are located in the directory Chem/KPP/mechanisms for different mechanisms declared as packages in the Registry file. In this study MOZART chemical mechanism was used which has about 85 gas phase species, 12 bulk aerosol components, 39 photolysis reactions and 157 gas phase reactions. The reaction set also includes updated isoprene oxidation scheme and VOC treatment, with three lumped species beyond 3 Carbon for alkenes. alkanes and aromatics (BIGENE, BIGALK and TOLUENE) and their oxidation products (Emmons et al., 2010). The global archived data MOZART dataset is available at 6-hr temporal resolution (https://www.acom.ucar.edu/wrf-chem/mozart.shtml) which is used as initial and boundary conditions for the model simulation on reanalysis mode.

The photolysis scheme in WRF-Chem comprises of the photolysis reactions which are calculated from the Fast-J scheme (Fast et al., 2006). This photolysis driver computes different frequencies at each of the grid points by treating aerosol absorption and molecular absorption online (Grell et al., 2005). It is to be noted that the actinic flux at each of the grid points is calculated by accounting the temperature, cloud fraction/profile, ozone concentration and water vapor mixing ratio. The water vapor mixing ratio acts as a proxy for estimating hygroscopic aerosol growth. The computation for 20 photochemical reactions begins with the estimation of incident solar radiation at the top of atmosphere which includes scattering and absorption of light at the surface. The main equation involved in photolysis calculation is following:

$$J_i = \int_0^{\lambda} I_A \times \sigma_{i\,(\lambda)} \times {}^{\varphi}{}_{\lambda} \quad (3.37)$$

Where, J_i (molecules cm^{-3} s^{-1}) is the frequency for the photochemical gas phase reactions for any particular species i, σ_λ is the absorption cross-section, ${}^{\varphi}{}_{\lambda}$ is the quantum yield over the range of wavelength. In WRF-Chem modelling system there are several radiative transfer options available (phot_opt = 1: Madronich TUV scheme (Madronich, 1987)), (phot_opt = 2: Fast J scheme (Fast et al., 2006)) and (phot_opt = 3: Madronich F-TUV scheme (Tie et al., 2003)). In this study we have used phot_opt = 3 Madronich F-TUV scheme where the photolysis rates are computed online by taking into account the influence of aerosols on photolysis rate and is updated hourly.

3.5 Model physics

This section discusses about the different physics options in the WRF-Chem model which has been used for parametrization of land surface, radiation, planetary boundary layer, convection and microphysics. The schematic in Figure 3.5 shows the representation of different parametrizations as modules and different processes/parameters through which different modules are connected.

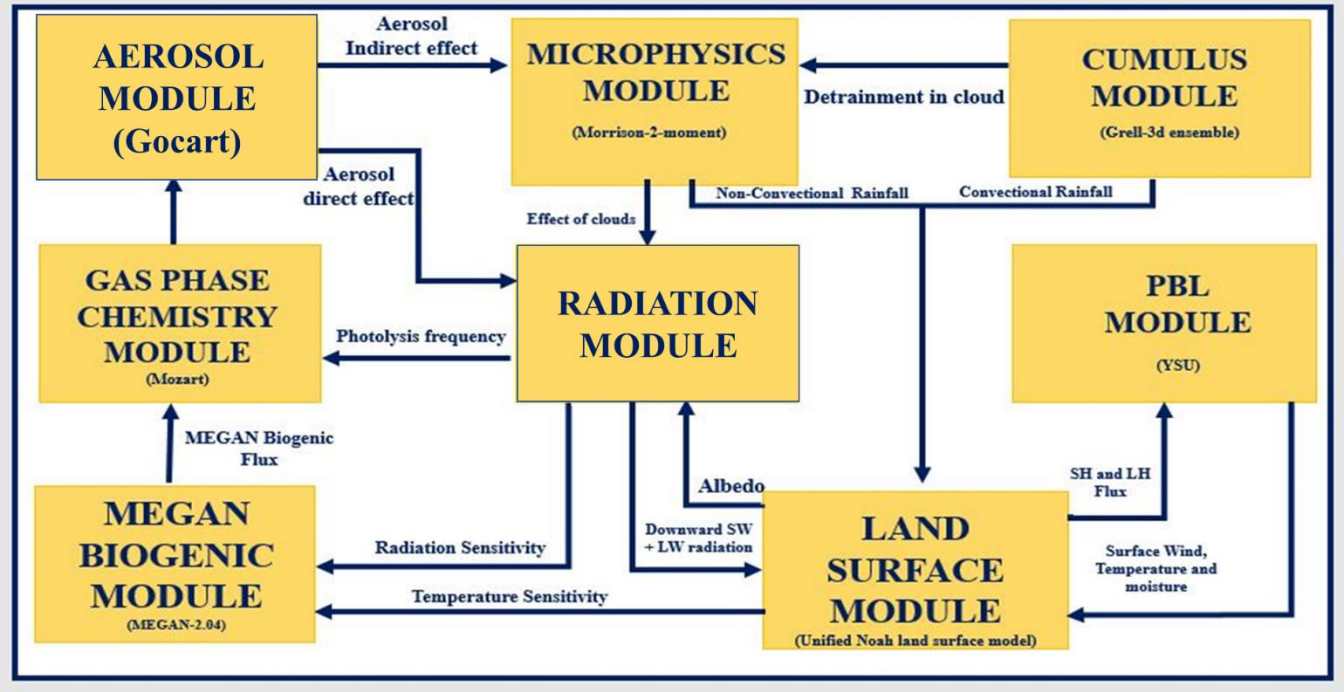

Figure 3.5 Overview of different modules showing different parametrizations in the WRF-Chem model.

3.5.1 The Surface layer scheme and the land surface model

The frictional velocities and exchange coefficients which are used in calculations of surface and moisture flux values in the land surface modules is provided by the surface layer scheme. In this study the Eta surface layer scheme which works on the principle of similarity theory has been used here, it also includes viscous sub-layer parametrization (Foken, 2006; Janjic, 1996; Janjić, 1994). The viscous sub-layer effects over the land are accounted for temperature and humidity variable through the roughness height (Zilitinkevich, 1995). Further to avoid the singularities when there is a case of unstable surface layer in the WRF-Chem model then corrections are applied as suggested by (Holdsworth et al., 2016). It is to be noted that in case of WRF-Chem model all the surface layer scheme is hard wired to a specific planetary boundary layer scheme in this study Eta Yonsei University (YSU) scheme has been used.

Numerical weather prediction models represent their lower most boundary and account for the sub-grid scale transport using land surface models. In this study the Noah land surface model has been used for simulating the above processes. The land surface models have a very critical role as they use information from different schemes as depicted in the schematic image in Figure 3.27. The land surface models use the atmospheric information from the surface layer scheme, use the

precipitation forcing from microphysics and cumulus schemes while it takes the radiative forcing from the radiation module and using the information about the surface properties (eg. land use type, albedo, soil moisture etc.) and land's state variables computes the heat and moisture flux values over the land and water bodies.

Any Land Surface Model provides 5 Quantities to its Parent Model which is WRF-Chem in this study. The four parameters include Q_H Surface Sensible Heat Flux, Q_E Surface Latent Heat Flux, Q_{lu} Upward Long wave radiation or surface emissivity $a \times Q_{su}$ Upward Short wave radiation or albedo and Q_M moisture transport flux through evapotranspiration as shown in Figure 3.6.

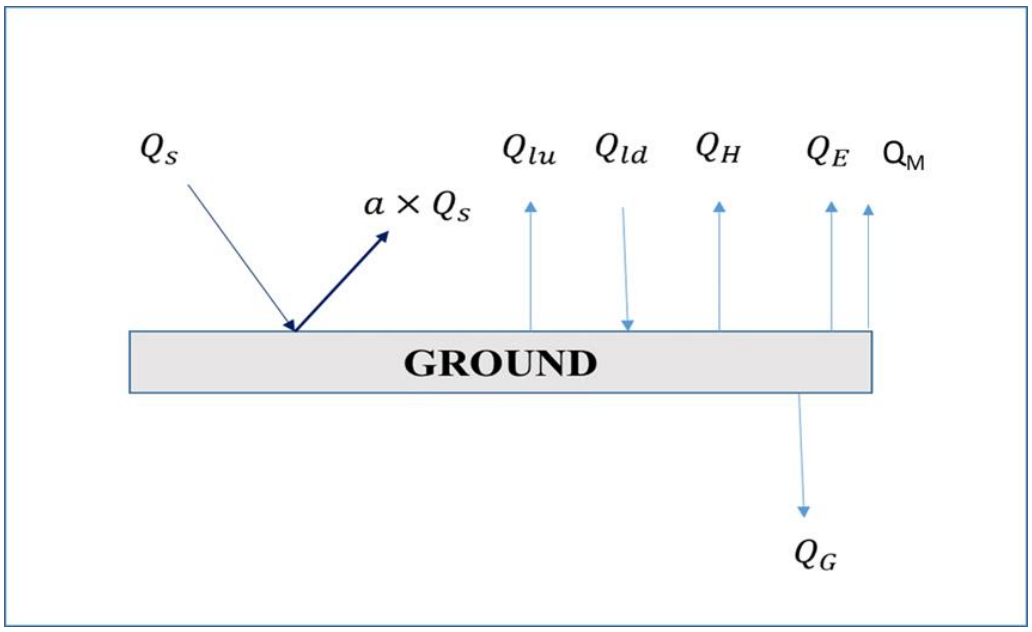

Figure 3.6 Schematic displaying different energy fluxes in land surface models.

These estimated surface sensible and latent heat flux values which drive the growth of planetary boundary layer and thus provide the WRF-Chem model with atmospheric tendencies of horizontal momentum, moisture, temperature and clouds in the entire vertical atmospheric column. The schematic in Figure 3.7 shows the details and processes associated with Noah land surface model. The land use data is provided as an input to the Noah land surface model which is linked to secondary parameters like green vegetation fraction, number of roots etc. through defined vegetation parameters as a look up table in the model code (VEGPARM.TBL). More details will be discussed in the next chapter

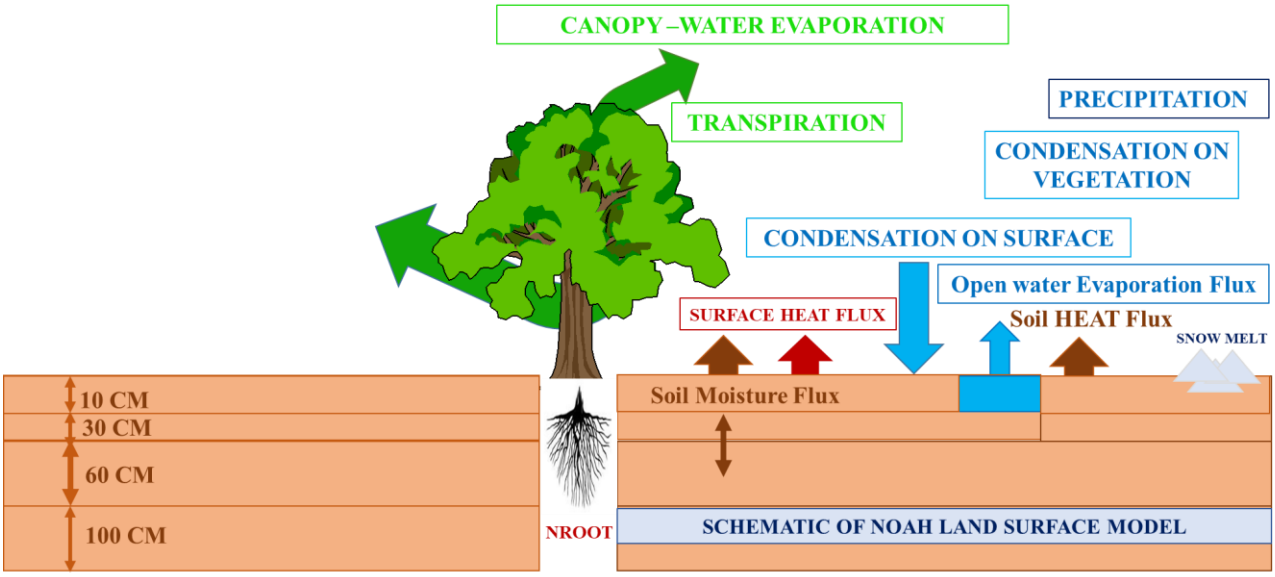

Figure 3.7 Schematic of Noah land surface model.

3.5.2 Radiation module

The radiation module in the WRF-Chem modelling system provides heating associated with SW and LW radiation in model. The radiation scheme uses radiative flux divergence along with downward shortwave and longwave radiation for computing the ground heat budget. The longwave radiation includes thermal or infrared radiation of the solar spectrum which is radiated from the surface and gases. The computed upward longwave flux is mainly sensitive to concentration of gases including water vapour, clouds (eg. too cloudy days can lead to cooling in the day time and warming at the night time), land cover type (mainly driven through emissivity), skin temperature etc. The short-wave radiation includes the visible and nearby wavelength comprising the solar spectrum. Reflection, scattering and absorption are the main processes which define the short wave radiation process. It is to be noted that land cover type (mainly driven through albedo) is the majority factor which is sensitive to the computed upward shortwave flux. In this study the long wave and short wave radiation has been studied using rapid radiative transfer model (RRTM) (Mlawer et al., 1997) (ra_lw_physics and ra_sw_physics =4).

3.5.3 Planetary boundary layer

The planetary boundary layer scheme computes the vertical sub-grid transport due to eddy turbulent transport in the whole atmospheric column. The main important way through which different PBLH schemes are parametrized is on the sole basis of how the perturbation quantities

are vertically distributed. This vertical gradient of perturbation quantities determines whether a particular PBLH scheme is local or non-local. In case of non-local closure schemes multiple vertical layers can be used to determine variables at a given point while in case of local schemes only the adjacent levels corresponding to that vertical level can directly affect the variables at that point. The vertical mixing throughout in case of a local scheme is accomplished through large eddies which leaves the local schemes at a disadvantage during localized stability conditions (Stensrud, 2007). The PBLH parametrization influences the representation of buoyancy, vertical wind shear as well as precipitation evolution (Hong et al., 2006) therefore one of the main objectives while configuring any model domain is performing sensitivity studies to select the best possible scheme on the basis of model validation. In WRF-Chem modelling setup there are both types of local and non-local schemes available for modelling (eg. Yonsei university (YSU) is a non-local scheme) while (Mellor-Yamada-Janjie (MYJ) is a local scheme) (Hu et al., 2010).

3.5.4 Microphysics and cumulus parametrization

There are mainly 2 options available in WRF-Chem modelling system to represent microphysics scheme namely single moment microphysics and double moment microphysics scheme. The single level scheme mainly computes number concentration for the different prognostic variables of water (eg. cloud, rain, snow etc.) while the double moment scheme also computes the mixing ratios of these prognostic variables apart from the number density. In this study a double moment Morrison microphysics scheme (Morrison et al., 2005) has been used (Morrison double moment mp_physics = 10). The main advantage of using a double moment scheme is computation of both number density and mixing ratios allows a more robust representation of particle size distribution which is very significant from point of view of cloud processes and precipitation. More details on these parametrizations can be found elsewhere (Skamarock and Weisman, 2009).

The cumulus parametrization in WRF-Chem modelling system computes vertical flux values which are unresolved due to small scale updrafts or downdrafts along with the compensating motion on the outside of clouds. As the spatial scale of the WRF-Chem model in this study was 10 km^2 therefore the model uses cumulus parametrization for computing sub grid scale shallow or convective cloud effects. These schemes become active in the modelling domain where an individual column gets a trigger which as a feedback provides elevated moisture and heat profile in those individual columns. It is worth mentioning that while nesting or performing high

resolution simulations (Horizontal resolution: < 5 km) it is advisable to deactivate the cumulus parametrization option in the namelist option by setting (cu physics = 0) (Wagner et al., 2018). In this study Grell 3D ensemble cumulus parametrization has been used for simulations at spatial resolution of 10 km^2. It fundamentally utilizes a cloud model with moist downward drafts and upward drafts along with incorporating effects of entrainment, detrainment and microphysics (Grell and Dévényi, 2002).

3.6 Model simulation over N. W IGP

The model domain was configured over N.W IGP with the different parametrization options as discussed in preceding chapters. The model was simulated for the month of august and validated with ground-based isoprene measurements. The plot in Figure 3.8 model domain and corresponding spatial variability of surface albedo at (01/08/2012: 00:00:00) of simulation. The plot in Figure 3.9 shows the average isoprene concentration for isoprene over the model domain for the month of august. Different studies have extensively utilized WRF model for simulating monsoon dynamics and climatology with similar parametrization schemes (Raju et al., 2015) (Ashrit and Mohandas, 2010) (Das et al., 2008). The plot in Figure 3.10 shows measured vs modelled isoprene values interpolated over Mohali. Modelled isoprene shows a strong under-prediction during the daytime. The under-prediction is due to missing source of daytime isoprene over N.W IGP which will be discussed in greater detail in the next chapter.

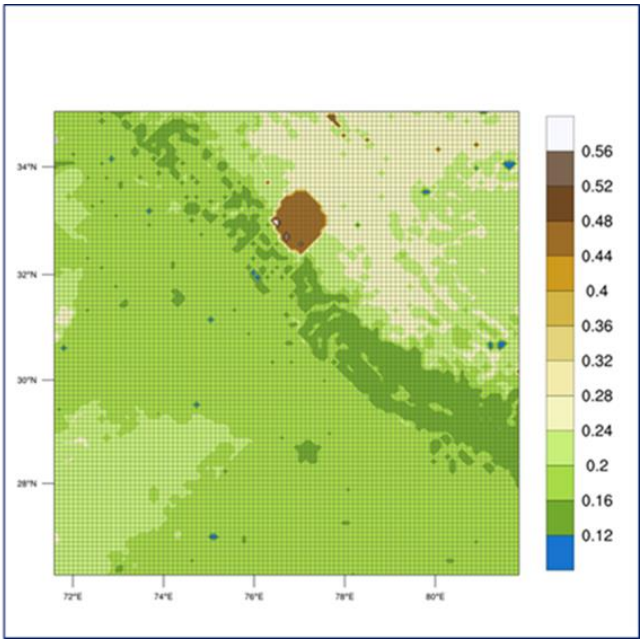

Figure. 3.8 Simulation domain showing the albedo values used by model at (01/08/2012: 00:00:00) of simulation

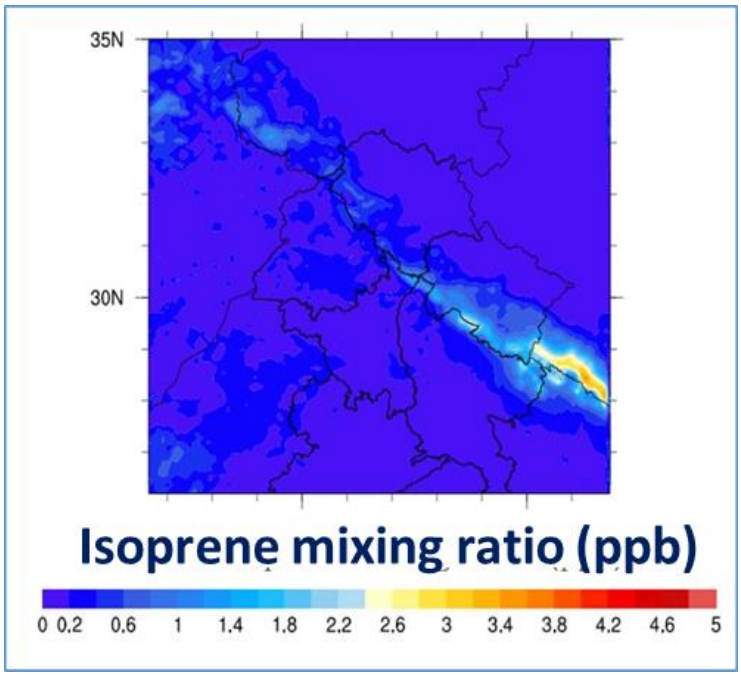

Figure 3.9 Plot showing average isoprene concentration over the model domain for month of august simulated using WRF-Chem.

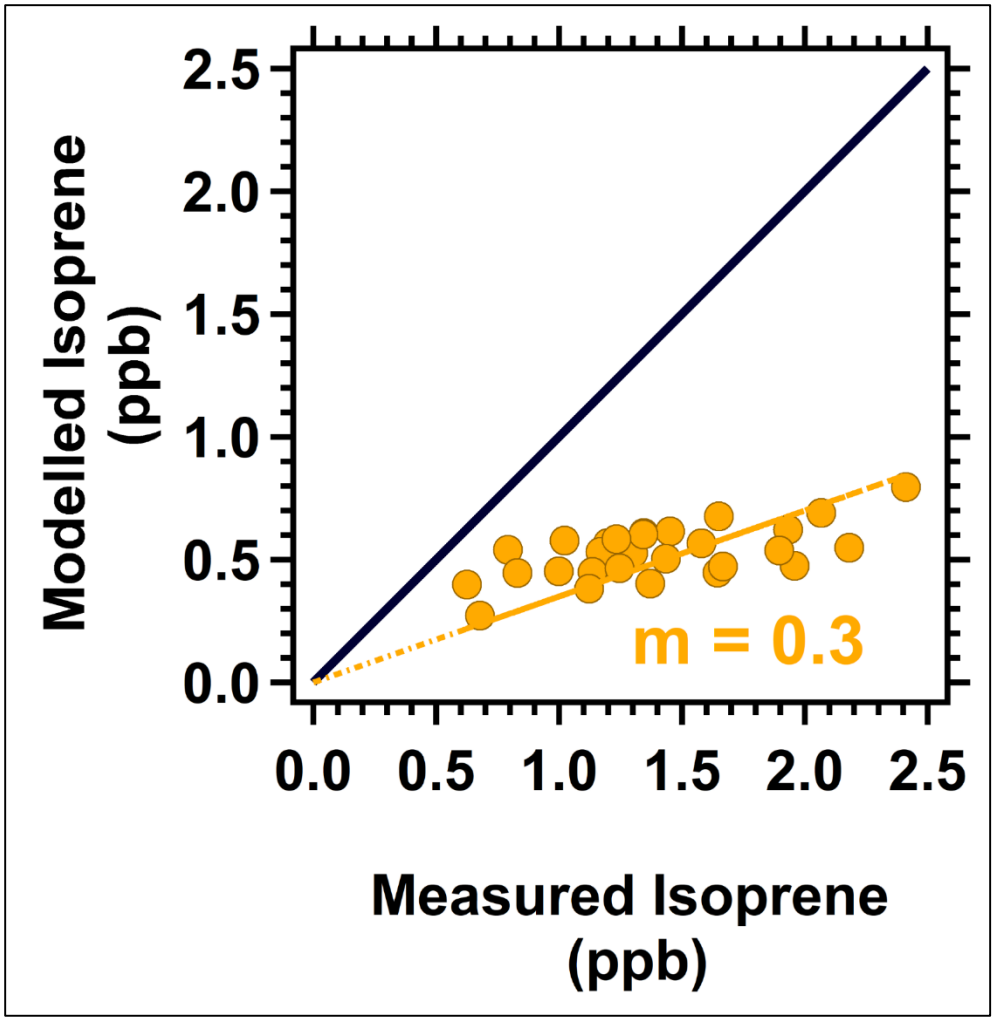

Figure 3.10 Plot showing measured vs modelled isoprene values interpolated over Mohali.

Chapter: 4

Cropland trees need to be included for accurate model simulations of land-atmosphere heat fluxes, temperature, boundary layer height, and ozone

The contents of this chapter have been published in the international peer reviewed journal as (Mishra et al., 2021), with B. Sinha, R. Kumar, M. Barth, H. Hakkim, V. Kumar, A. Kumar, S. Datta, A. Guenther and V. Sinha. This study was designed by V. Sinha and B. Sinha. I analyzed the VOC measurements and model runs with B. Sinha and V. Sinha. I had set-up the WRF-Chem model with technical inputs from R. Kumar and M. Barth. I processed the GlobCover 2009, and ERA-5, MOD44B and Landsat 30-m VCF dataset with help from V. Kumar. A. Guenther provided expert inputs on MEGAN and CLM model. H. Hakkim A. Kumar, S. Datta helped in isoprene data analysis. All authors discussed the results and commented on the paper.

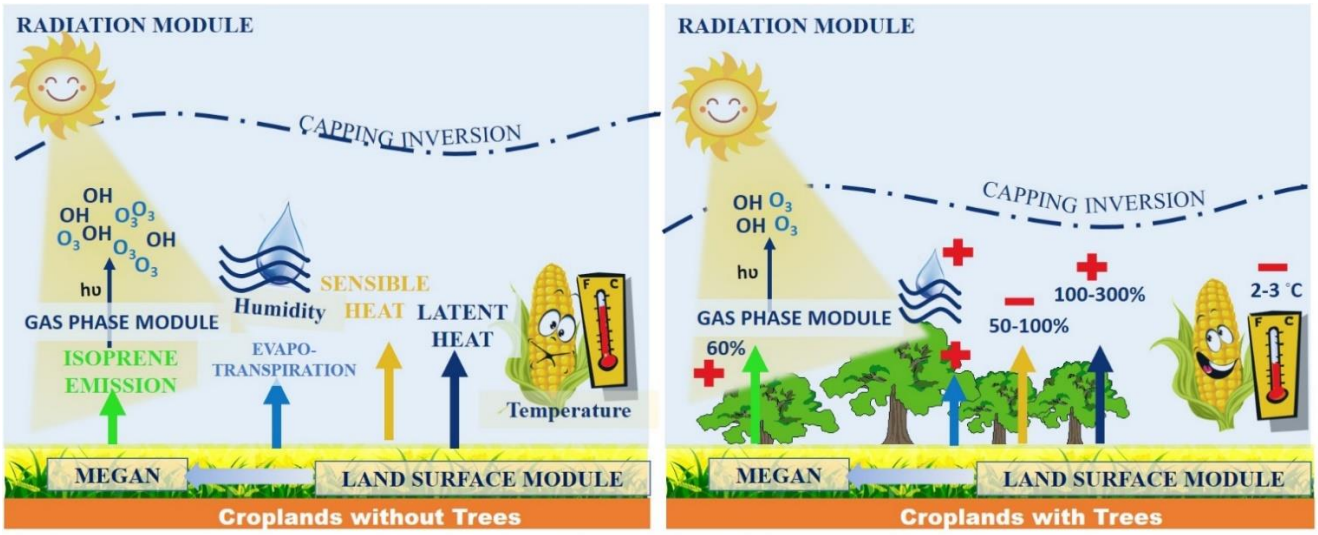

Figure 4.1 Graphical abstract of the chapter.

4. 1 Abstract

Trees significantly impact land-atmosphere feedbacks through evapotranspiration, photosynthesis and isoprene emissions. These processes influence the local microclimate, air quality and can mitigate temperature extremes and sequester carbon dioxide. Despite such importance, currently only 5 out of 15 atmospheric chemistry climate models even partially account for the presence of cropland trees. We first show that the tree cover over intensely farmed regions in Asia, Australia and South America is significantly underestimated (e.g. only 1-3% tree cover over north-India) in the Model of Emissions of Gases and Aerosol from Nature (MEGAN) and absent in Noah land-surface module of the weather research and forecasting (WRF-Chem) Model. By including the actual tree cover (~10%) over the north-west Indo Gangetic Plain in the Noah land-surface module of the WRF-Chem and the MEGAN module, during the rice growing monsoon season in August, we find that the latent heat flux alone increases by 100-300% while sensible heat flux reduces by 50-100%, leading to a reduction in daytime boundary layer height by 200-400 m. This greatly improves agreement between the modelled and measured temperature, boundary layer height and surface ozone, which were earlier overestimated and isoprene and its oxidation products which were earlier underestimated. Mitigating peak daytime temperatures and ozone improves rice production by 10-20%. Our findings from north-west Indo-Gangetic Plain establish that such plantations mitigate heat stress, and have beneficial effects on crop yields while also sequestering carbon. Expanding agroforestry practices to 50% of the cropland area could result in up to 40% yield gain regionally. Implementing such strategies globally could increase crop production and sequester 0.3-30 GtC per year, and therefore future climate mitigation and food security efforts should consider stakeholder participation for increased cropland agroforestry in view of its beneficial effects.

4.2 Introduction

Agroforestry has long been recognized as a practice that brings pecuniary benefits to farmers (Current et al., 1995). It is well known that trees can change land-atmosphere-feedbacks through both evapotranspiration and photosynthesis and yet the impact of these trees on the microclimate of agricultural landscapes, atmospheric boundary layer meteorology, ozone and crop yields and

global relevance has received much less attention than the potential climate benefits of trees in general through carbon-capture.

Since the 1980s farmer driven expansion (Bannister and Nair, 2003; Reij and Garrity, 2016; Salam et al., 2000) and policy interventions (Chavan et al., 2015; Lasco et al., 2014) around the world have greatly increased the tree cover of croplands (Song et al., 2018; Zomer et al., 2016) through agroforestry (Bannister and Nair, 2003; Chavan et al., 2015; Reij and Garrity, 2016; Salam et al., 2000) , silvi-pastoralism (Knoke et al., 2014) and permaculture (Hathaway, 2016). Currently about 43% of the world's agricultural area has greater than 10% tree cover (Song et al., 2018; Zomer et al., 2016). Despite these changes in the recent decades, the most recent tree census (Crowther et al., 2015) declared major parts of South Asia, mainland China and other regions with intense agriculture to be devoid of trees. The tree driven land-atmosphere feedbacks can mitigate temperature extremes and impact microclimates and atmospheric chemistry in several ways. Despite such importance, currently tree cover in croplands across major populated continents remains significantly underestimated. The issue of the missing cropland trees is also not limited to a specific land surface module and appears to be common to the land surface modules of several models used in the latest IPCC report (Flato et al., 2013). Table 4.1 shows that BVOC emission modules Lund-Potsdam-Jena General Ecosystem Simulator (LPJ-GUESS) and Model of Emissions of Gases and Aerosol from Nature (MEGAN) have been incorporated into 5 of the 15 global models. The Biogenic volatile organic compound (BVOC) emission modules (LPJ-GUESS and MEGAN) which have been incorporated into 5 out of 15 global models currently account for trees in croplands only partially. Generally, the LPJ-GUESS BVOC emission module has higher BVOC emissions over croplands than the MEGAN BVOC emission module. However, both do not account for the increase in tree cover over agricultural regions since the year 2000 (Chen et al., 2018). Till date there are no studies quantifying the impact of agroforestry on regional boundary layer dynamics, temperatures and the air quality of intensely farmed regions. This represents a critical knowledge gap which hampers our ability to use global models for accurately assessing the impact of environmental stress (Xu et al., 2019) and air pollution (Tai et al., 2014; Yue and Unger, 2014) on crops and natural ecosystems in intensely farmed regions.

In this study we investigate the extent of missing cropland trees in several globally significant regions of the world and then using in-situ observations and the Weather research and forecasting

(WRF) model illustrate the consequences of the missing tree cover for modelled temperature, sensible and latent heat fluxes, boundary layer height, ozone and isoprene over one of the world's most intensely cultivated agricultural region with high population density, namely the north west Indo-Gangetic Plain during the rice growing season in summer monsoon season. We discuss the relevance of the results for contemporary and future practices and the potential benefits that could accrue from increases in agroforestry over the north-west Indo Gangetic Plain in terms of ozone and heat mitigation and improved rice crop yields and as an example for climate and crop yield gains globally.

Table 4.1 Comparison of different GCMs which all took part in IPCC AR5 & CMIP5 simulation

MODEL	**Reference**	**Trees in cropland present in Land surface model?**	**Trees in cropland present in BVOC emission model?**
HadCM3	(Cox et al., Hadley Centre technical note 23, 2001)	No (TRIFFID)	No (BVOC emissions)
IPSL (CM5A)	(Hansen et al., 2000; Poulter et al., 2015; Zhu et al., 2015)	No (ORCHIDEE)	No (BVOC emissions)
CSIRO (BOM/QCCCE)	(De Kauwe et al., 2015; Loveland et al., 2000; Wang et al., 2012)	No (CABLE 2)	No (BVOC emissions)
BCC-CSM	(Wu et al., 2014)	No (BCC-AVIM1.0 CLM3.0)	No (BVOC emissions)
NASA-GISS (E2)	(Schmidt et al., 2014)	No (TBM & SVATS)	No (MEGAN2.1)
MIROC (ESM/CHEM)	(Sato et al., 2007; Watanabe et al., 2011)	No (MATSIRO, SEIB-DGVM)	No (BVOC emissions uncoupled to Vegetation)
NCEP	(Yuan et al., 2011)	No (NOAH LSM)	No (BVOC emissions)

NOAA-GFDL	(Delworth et al., 2006)	No (AM2-LM2)	No (BVOC emissions)
INMCM4	(Volodin et al., 2010)	No (SWAP)	No (BVOC emissions)
FGOALS-gl	(Lawrence and Chase, 2007; Peng and Dan, 2014; Zhou et al., 2018)	partial (CLM3.0)	No (BVOC emissions)
ECHAM5	(Goll et al., 2017; Loveland et al., 2000; Makkonen et al., 2012; Pongratz et al., 2008; Sitch et al., 2003)	No (JSBACH)	partial (LPJ GUESS & MEGAN2)
ECHAM6-HAMMOZ	(Brovkin et al., 2009; Goll et al., 2017; Pongratz et al., 2008; Schultz et al., 2018)	partial (JSBACH)	partial (MEGAN2.1 & LPJ GUESS)
MPI-M (MPI-ESM-P)	(Brovkin et al., 2009; Giorgetta et al., 2013; Goll et al., 2017; Sitch et al., 2003)	partial (JSBACH)	partial (LPJ GUESS)
CCSM4	(Ke et al., 2012; Lawrence et al., 2011; Lawrence and Chase, 2007)	partial (CLM-4.0)	partial (MEGAN2.1)
CMCC (CMCC-CM)	(Cherchi et al., 2019)	partial (CLM 4.5)	no (BVOC emissions)

4.3 Materials and methods

4.3.1 Site and choice of study period

Figure 4.1 shows the location of the IISER Mohali atmospheric chemistry measurement facility a sub-urban site on a 30-m continuous vegetation field (CVF) map from Landsat (Sexton et al., 2013) with a colour scale representing the % of tree cover. The site and multi-year climatology has been described previously in Kumar et al., 2016 and Pawar et al., 2015. The red square in Figure 1 marks the modelling domain of the current study, the middle panel a zoom in version and the extreme right panel in Figure 4.2 shows snapshots of the land-use in its vicinity. The site is close to forested slopes at the foothills of the Himalayan mountain range (~30 km in the north-west and south-east direction) and it should be noted that the study site does not have anomalously high tree cover relative to its surroundings. In the state of Punjab where the site is located, villages, towns and even the neighbouring city of Chandigarh stand out as light coloured areas with below average tree cover against a backdrop of much higher (10-20%) tree cover in the agricultural lands. Chandigarh, which is one of the three nearest cities to the measurement site, lies in the north to the east wind sector, and it has been designated as a green city that has nearly 42,000 trees belonging to 66 tree species growing along the road in a systematic manner (Kohli et al., 2000).

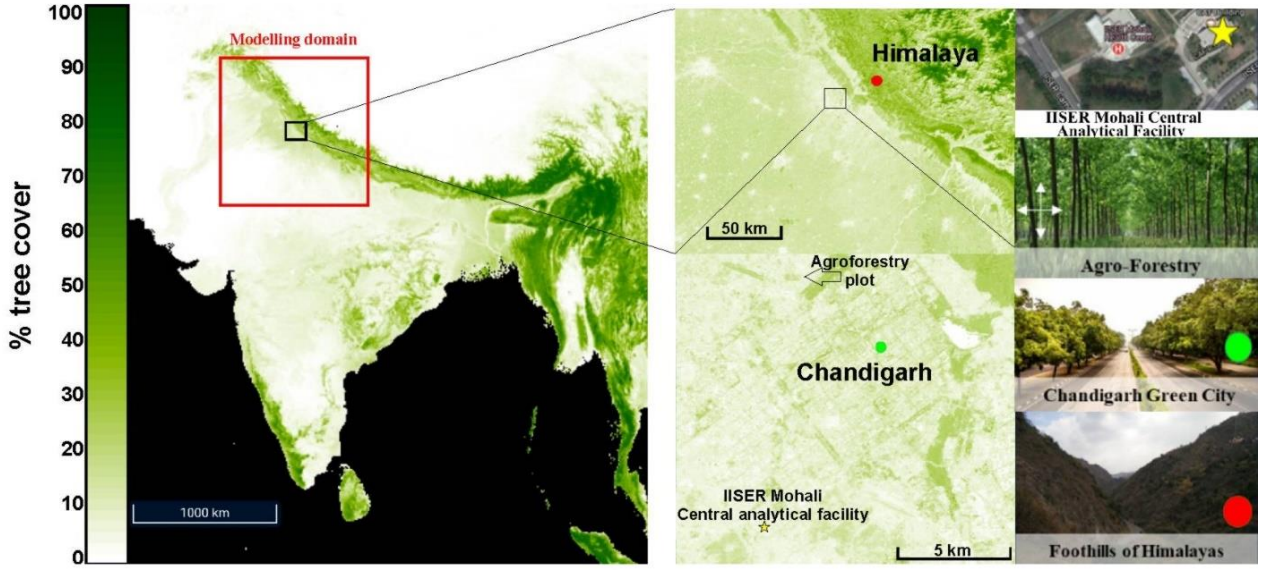

Figure 4.2 (Left) Location of Mohali on a 30-m continuous vegetation field (CVF) map from Landsat. The red square delineates the modelling domain of our case study. (Middle) Exact location of measurement facility zoomed, (Right) some images of the vegetation surrounding the atmospheric chemistry facility.

The site is flanked by rural and agricultural lands in the west and north-west wind sector, which is also the dominant fetch region. Due to mixed agroforestry practices prevalent over the region, the rural and agricultural lands have large swathes of poplar and eucalyptus, which are planted at the periphery of agricultural fields and along roads. We chose the month of August 2012 for this study because during peak monsoon season the impact of vegetation on atmospheric chemistry is strongest (vegetation throughout the region is not moisture limited) while many anthropogenic fire sources such as crop residue burning and forest fires are absent during this time period and even residential biofuel and waste burning are lowest during this time of the year. A longer study period would overlap with the onset of the monsoon in July and the crop residue burning of short duration rice cultivars that are harvested early in September. During monsoon onset, difficulties with reproducing the spatio-temporal patterns of the first monsoon showers correctly can have a disproportionate impact on the model output and would affect all aspects of the model from energy and moisture fluxes over radiation and photochemistry to BVOC emissions. During crop residue burning (May, September-November), wildfire (March-June) and landfill fire (March-June) affected periods, any model-measurement comparison is dominated by difficulties associated with representing the high spatio-temporal variability of fire sources accurately. In particular, small fires that are difficult to detect present severe challenges. Winter season is even more challenging when it comes to model-measurement comparison, as the strong temperature and fog-induced day to day variations of residential fuel usage are not accurately represented in any emission inventory (Hakkim et al., 2019). Hence, since the focus of the present study is on the impact of cropland trees we chose the month of August which has the best signal to noise ratio while studying the impact of vegetation on the regional atmospheric chemistry and dynamics. The year 2012 was selected for this study, because it is the first year for which we have observational data for the full month of August, and the most recent year for which an updated emission inventory is available (Crippa et al. 2018).

4.3.2 Ambient measurements of temperature, ozone, isoprene and its oxidation products

Ambient temperature, radiation, relative humidity, wind direction, wind speed and ozone are measured routinely at the site using a meteorological station (Met One Instruments Inc., Rowlett, USA) and sampling inlets at ~20 m above ground, as described previously (Sinha et al., 2014). Ozone is measured using UV absorption photometry (Model 49i Thermo Fischer Scientific,

Franklin, USA). Comprehensive description of the instrument including QA/QC in terms of accuracy and linearity is available elsewhere and the total uncertainty of the ozone measurements was less than 6% (Sinha et al., 2014).

The measurement of isoprene and isoprene oxidation products, that is the sum of methacrolein (MACR) and methyl vinyl ketone (MVK), was carried out using a high sensitivity proton transfer reaction quadrupole mass spectrometer (PTR-MS). The instrument inlet was also positioned at a height of ~20 m above ground. An analytical description of the PTR-MS, along with standard operating and calibration protocols, are available in previous works from our group (Chandra and Sinha, 2016; Sinha et al., 2014). Isoprene (C_5H_8; M.W: 68.12 g/mol) is detected at its protonated organic ion m/z = 69 (de Gouw and Warneke, 2007) after soft ionization with hydronium ions, the reagent ion used in the PTR-MS technique. Previous PTR-MS studies including some from our own group have shown that isoprene can also be emitted from anthropogenic sources and have contributions at m/z 69 from furan produced from combustion and biomass burning sources (Akagi et al., 2011; Karl et al., 2007; Yokelson et al., 2013). So we took care to confirm that the daytime isoprene in the monsoon season in this region was indeed primarily due to biogenic emissions. In the Kathmandu valley a study performed by our group (Sarkar et al., 2016) using a higher resolution proton transfer time-of-flight mass spectrometer that can resolve isoprene from furan in the winter (December 2012-January 2013), showed that the signal at m/z 69 was mainly from isoprene, and furan contributed a maximum of up to 25 % to the signal even during peak night time biomass burning. At the site of the present study in Mohali, we also determined isoprene to be the major contributor to measured m/z 69 signal based on the VOC-OHM technique (Kumar and Sinha, 2014). Furthermore, the ambient daytime isoprene mixing ratios were found to respond to solar radiation and temperature as is characteristic of biogenic emissions and not the case for anthropogenically emitted molecules. Given the prevalence of poplar and eucalyptus trees in the fetch region as well as findings reported in previous studies including from India that poplar and eucalyptus are high isoprene emitters (He et al., 2000; Schnitzler et al., 2010; Varshney and Singh, 2003), and some plant chamber experiments on a poplar tree, we are therefore confident about the assignment of m/z 69 to isoprene during monsoon season in the region.

The sum of methacrolein (MACR) (C_4H_6O; M.W: 70.09 g/mol) and methyl vinyl ketone (MVK) (C_4H_6O; M.W: 70.09 g/mol) were detected at the protonated organic ion m/z = 71. The specificity

of PTR-MS to monitor MVK + MACR has been demonstrated previously (de Gouw and Warneke, 2007; Vlasenko et al., 2010; Warneke et al., 2011). As a part of QA/QC, PTR-MS was calibrated for isoprene and sum of methacrolein and methyl vinyl ketone using a VOC gas standard (Apel-Riemer Environmental, USA) with VOC free zero air as described in Sinha et al., 2014. The overall uncertainty for isoprene and MVK+MACR reported in this work was below 20%.

4.3.3 Global occurrence of cropland trees in major agricultural regions

Figure 4.3 shows maps of the tree cover over four major agricultural regions of the world namely South Asia (10°N -38°N and 68°E -100°E, Panels A, E, I and M), the North China plains (35°N -45°N and 105°E -130°E) in East Asia (Panels B, F, J, N), Victoria and New South Wales (30°S -40°S and 130°E -155°E) in Australia (Panels C, G, K, O) and the Rio de la Plata river basin (27°S -39°S and 48°W -71°W) in South America (D, H, L, P.). Red arrows highlight areas with irrigated or rain fed cropland for which the present day tree cover is underestimated by the Noah land surface and MEGAN module in South Asia (10°N -38°N and 68°E -100°E, Panels A, E, I and M), the North China plains (35°N -45°N and 105°E -130°E) in East Asia (Panels B, F, J, N), Victoria and New South Wales (30°S -40°S and 130°E -155). Panels A to D show the tree cover according to the global tree count exercise carried out by Crowther et al., 2015 in number of trees per km^2. During this global tree counting exercise the authors only counted trees in natural landscapes. Croplands and cities were assumed to be devoid of trees. The Noah land surface module in the WRF-Chem is based on similar assumptions. When a model grid cell is correctly identified as agricultural land it is assumed to be devoid of trees. Panels E to H show the tree cover in the MEGAN as % of the ground covered by a crown (Guenther et al., 2006 and Guenther et al., 2012). Panels I to L show the tree cover of the 30 m continuous vegetation field Landsat (Sexton et al., 2013) product in % of the ground covered by a crown. Panels M to P show the GlobCover land use land cover (LULC) classification map. It can be seen that all underestimate cropland tree cover relative to the Landsat images. We note that the most recent tree census (Crowther et al., 2015) declared major parts of South Asia, mainland China and other regions with intense agriculture to be devoid of trees (Figure 4.3 A-D) and these same areas are treated as devoid of trees in the Noah land surface module. As trees have direct impacts on sensible and latent heat fluxes at the land-atmosphere interface, temperature and associated atmospheric dynamics they can therefore significantly impact the microclimate of croplands affecting crop yields. The significant

underestimation of the tree cover over croplands in MEGAN model (Guenther et al., 2006; Guenther et al., 2012) which have 0 to less than 10% tree cover (Figure 4.3) would also have consequences for low modelled isoprene fluxes over intensely farmed regions of Asia in recent studies (Stavrakou et al., 2014). Figure 4.3 demonstrates that this problem is not restricted to Asia and the underestimation of the tree cover can be observed in other intensely farmed regions elsewhere in Asia, Australia and South America (Figure 4.3 G-H and K-L).

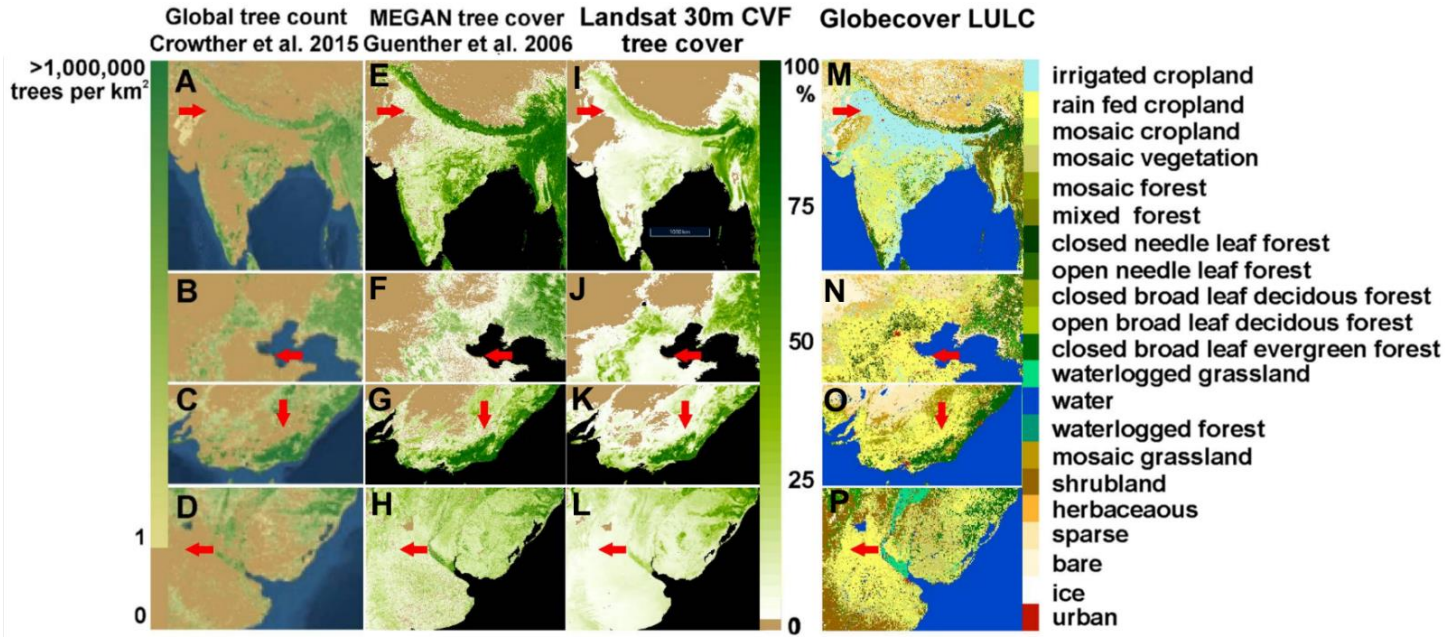

Figure 4.3 Four major agricultural regions in the world in which vast tracts of land were declared as devoid of trees during the global tree count. Red arrows highlight areas with irrigated or rain fed cropland for which the present day tree cover is underestimated by the Noah land surface and MEGAN module in South Asia (10°N -38°N and 68°E -100°E, Panels A, E, I and M), the North China plains (35°N -45°N and 105°E -130°E) in East Asia (Panels B, F, J, N), Victoria and New South Wales (30°S -40°S and 130°E -155°E) in Australia (Panels C, G, K, O) and the Rio de la Plata river basin (27°S -39°S and 48°W -71°W) in South America (D, H, L, P.). Panels A to D show the tree cover according to the global tree count in number of trees per km^2. Panels E to H show the present day tree cover percentage according to MEGAN in the units percent of the ground covered by a crown. Panels I to L show the present day tree cover percentage of the 30 m continuous vegetation field Landsat product in the units percent of the ground covered by a crown. Panels M to P show the GlobCover land use land cover (LULC) classification map.

4.4 Methodology for revised tree cover estimation

To estimate the fractional tree cover for different types of croplands on different continents (Table 4.2) we used the Moderate Resolution Imaging Spectroradiometer (MODIS) sensor derived Vegetation Continuous Fields (VCF) yearly product for global representation of vegetation cover, namely MOD44B version-6 (Dimiceli et al., J.R.G. 2015. Accessed 2019-06-09) and the European Space agency GlobCover land use land cover (LULC) datasets (Arino et al., E.S.A 2012 GlobCover Dataset). Before proceeding with our analysis we compared MOD44B version-6 VCF with the Landsat 30 m VCF (Sexton et al. 2013) which was brought to the same spatial resolution as the MOD44B VCF using a mode sampling algorithm. Reduced Major Axis regression revealed no systematic bias (slope of 0.94, r=0.6) between the two VCF products for the centre of our case study region. Hence we proceeded with the 250 m VCF product, which is computationally less expensive to process, for our analysis. The MOD44B dataset yields the % tree cover at 250 m pixel resolution but does not differentiate broadleaf and needleleaf trees. GlobCover provides 22 numeric LULC classes at 300 m spatial resolution and differentiates broadleaf trees, needleleaf trees, shrubs, herbs, crop and various mosaic land cover types. Firstly, we use these two datasets to establish the average tree cover of croplands on different continents. For both the datasets, pixel-wise extraction was accomplished using geospatial data abstraction library (GDAL/OGR contributors 2020), an open-source library used for geospatial data processing. The MOD44B extracted dataset was resampled using mode resampling technique, and the fractional tree cover was computed at 1 x 1 km^2 grid resolution. Similarly, the GlobCover land use classes at 300 x 300 m^2 pixels of dataset were first aggregated and then re-gridded at 1 x 1 km^2 to compute fractional cover of each LULC class. To calculate the average tree cover for each LULC class of the GlobCover dataset, MOD44B pixels were matched with GlobCover pixels only for such pixels where at least a full 1 x 1 km^2 pixel belonged to the same LULC class. The average tree cover of each GlobCover LULC class for several regions in each of the continents is shown in Table 4.2 Table 4.1 includes only LULC classes for which at least 100 continuous 1 x 1 km^2 pixels could be evaluated on the respective continent. Overall more than 10 million points with a minimum of 1 million points on each continent were evaluated to generate Table 4.2. The Tundra and Taiga biomes across Eurasia and North America were tabulated separately from the rest of the respective continents. Our results in Table 4.2 clearly show that 2-45% tree cover in croplands persist across all continents although the tree density, particularly for mosaic croplands varies from region to

region with the prevalent land management practices. Hence, the findings of this study have relevance for other intensely cropped regions.

Next, in order to compute the input files with the revised tree cover for our study region, we used both datasets to compute the fractional tree cover of each 10 x 10 km^2 pixel for our South Asian modelling domain (Table 4.3). The fractional tree cover by broad leafed and needle leafed trees, shrubs, herbs and bare land is required as input for the MEGAN module of the WRF-Chem model. In this context we use MOD44B to estimate the average tree cover and GlobCover to assign the trees to the correct plant functional class (i.e. to broad leaf or needle leaf trees) depending on the relevant LULC class.

Table 4.2 Tree cover percentage of LULC classes for GlobCover pixels over different continents.

class	GlobCover name	Tree cover [%] of LULC class							
		South Asia	Whole Asia	Africa	Australia & Oceania	South America	North America	Europe	Tundra /Taiga
11	Post-flooding or irrigated croplands (or aquatic)	10.5	10.1	11.6	n.a.	n.a.	n.a.	3.4	n.a.
14	Rainfed croplands	7.6	6.9	1.6	12.9	15.3	3.1	5.8	n.a.
20	Mosaic cropland (50-70%) / vegetation (grassland/shrubland/forest) (20-50%)	10.2	9.1	1.9	44.9	19.3	9.7	7.3	n.a.
30	Mosaic vegetation (grassland/shrubland/forest) (50-70%) / cropland (20-50%)	7.0	9.1	13.6	36.6	15.8	11.7	9.2	n.a.
40	Closed to open (>15%) broadleaf evergreen or semi-deciduous forest (>5m)	67.3	67.1	58.9	65.7	60.4	59.1	n.a.	n.a.
50	Closed (>40%) broadleaf deciduous forest (>5m)	35.2	53.1	36.4	n.a.	25.4	44.6	40.6	47.8
60	Open (15-40%) broadleaf deciduous forest/woodland (>5m)	37.9	37.9	13.7	29.5	28.3	n.a.	n.a.	n.a.
70	Closed (>40%) needleleaf evergreen forest (>5m)	55.2	48.9	27.8	68.9	n.a.	38.1	39.1	n.a.
90	Open (15-40%) needleleaf deciduous or evergreen forest (>5m)	n.a.	40.2	n.a.	n.a.	n.a.	52.2	43.4	38.0
100	Closed to open (>15%) mixed broadleaf and needleleaf forest (>5m)	38.2	34.3	n.a.	71.6	n.a.	52.9	53.0	48.6
110	Mosaic forest or shrubland (50-70%) / grassland (20-50%)	26.5	38.2	6.4	12.2	3.4	10.5	22.9	11.5
120	Mosaic grassland (50-70%) / forest or shrubland (20-50%)	1.7	2.9	8.1	24.5	6.0	22.0	18.8	9.9
130	Closed to open (>15%) shrubland (<5m)	52.9	48.7	13.8	22.4	15.7	1.5	14.5	n.a.
140	Closed to open (>15%) herbaceous vegetation	2.9	3.0	0.8	6.6	19.9	14.4	17.9	19.3
150	Sparse (<15%) vegetation	0.1	4.5	0.3	0.9	4.0	19.6	7.6	5.3
160	Closed to open (>15%) broadleaf forest regularly flooded	n.a.	n.a.	66.8	64.2	59.2	6.6	n.a.	n.a.
170	Closed (>40%) broadleaf forest or shrubland permanently flooded	33.5	33.5	9.3	54.8	n.a.	44.1	n.a.	n.a.
180	Closed to open (>15%) grassland or woody vegetation on regularly flooded or waterlogged soil	0.2	0.3	3.7	n.a.	29.7	n.a.	25.6	15.9
190	Artificial surfaces and associated areas (Urban areas >50%)	8.1	6.1	2.8	12.0	5.1	16.7	9.2	11.3
200	Bare areas	0.2	0.2	0.2	0.1	1.8	5.4	0.7	1.3
210	Water bodies	0.0	0.1	0.0	0.0	0.2	0.7	0.2	0.2
220	Permanent snow and ice	1.2	1.2	n.a.	n.a.	0.5	0.1	n.a.	1.5

Table 4.3 Vegetation cover percentage of LULC classes for GlobCover pixels over South Asia (7.2°N to 37.4°N and 67.0°E to 100.0°E). Figure 4.1 shows the locations of the pixels for which manual photo-interpretation was performed.

class	GlobCover LCC name	Plant function type				
		broad-leafed tree	needle leafed tree	shrubs	herbs	bare
11	Post-flooding or irrigated croplands (or aquatic)	10.5	0	10.5	79	0
14	Rainfed croplands	9.6	0	3.4	47	40
20	Mosaic cropland (50-70%) / vegetation grassland/ shrubland/ forest) (20-50%) Desert and steppe climate Tropical and temperate climate	 2 11	 0 0	 2 19	 89 60	 7 10
30	Mosaic vegetation (grassland/shrubland/forest) (50-70%) / cropland (20-50%) Arid & montane climate Tropical moist climate	 5 17	 0 0	 8 45	 47 37	 40 1
40	Closed to open (>15%) broadleaf evergreen or semi-deciduous forest (>5m)	67	0	14	13	6
50	Closed (>40%) broadleaf deciduous forest (>5m)	35	0		12	3
60	Open (15-40%) broadleaf deciduous forest/woodland (>5m)	38	0	33	26	3
70	Closed (>40%) needleleaf evergreen forest (>5m)	0	55	35	5	5
90	Open (15-40%) needleleaf deciduous or evergreen forest (>5m)	0	42	24	13	21
100	Closed to open (>15%) mixed broadleaf and needle-leaved forest (>5m)	38	24	10	22	6
110	Mosaic forest or shrubland (50-70%) / grassland (20-50%)	26.5	0	12.5	26	35
120	Mosaic grassland (50-70%) / forest or shrubland (20-50%) Montane climate Tropical and temperate climate Desert and steppe climate	 10 7.5 0	 29 2 0	 5 79.5 4	 28 5 58	 28 6 38
130	Closed to open (>15%) shrubland (<5m)	53	1	25	19	2
140	Closed to open (>15%) herbaceous vegetation Montane climate Desert and steppe climate	 2 5	 3 0	 2 2	 24 24	 69 69
150	Sparse (<15%) vegetation	1	0	1	17	81
160	Closed to open (>15%) broadleaf forest regularly flooded	60	0	5	1	34
170	Closed (>40%) broadleaf forest or shrubland permanently flooded	33.4	0	38.6	18	10
180	Closed to open (>15%) grassland or woody vegetation on regularly flooded or waterlogged soil	0	0	1	12	87
190	Artificial surfaces and associated areas (Urban areas >50%)	8	0	12	20	60
200	Bare areas	0	1	4	13	82
210	Water bodies	0	0	0	0	100
220	Permanent snow and ice	0	1	0	0	99

4.5 Estimation of the fractional LULC cover in terms of plant functional types over South Asia for modeling experiments

Biogenic emissions of gases and aerosols are calculated using the MEGAN model version 2.04 (Guenther et al., 2006) but this requires the land use land cover distribution in terms of the respective plant functional types such as broad leaf, needle leaf, shrubs, herbs (including crops) and bare land. For the model simulations over South Asia, the fractional cover by shrubs, herbs and bare land was established using a photo-interpretation approach (Bey et al., 2016), while the fractional cover with broadlef and needleleaf trees was calculated by combining MOD44B and GlobCover as described in section 4.4. More than 500 pixels from the 19 LULC classes available in the GlobCover classes were randomly chosen for photo interpretation. The selected 300 x 300 m^2 pixels were used for manual photo-interpretation of very high spatial resolution satellite images, made freely accessible for visualization on Google Earth. We performed spot counting (Bastin et al., 2019) using a grid of 9 x 9 spots for a 300 x 300 m^2 image for computing the fraction of each plant functional type (Plant function types (PFTs)- broadleaf trees, needleleaf trees, shrubs, and herbs) used by MEGANv2.04 model (Figure 4.4). The set of images in Figure 4.5 illustrate the principle of calculation and show a GlobCover pixel with the 81 counting spots overlaid on Google Earth. When the intersection points of the grid coincide with a vegetation class, a match is scored as shown in the calculation for the plant function type count in Figure 4.5. The assignment to the vegetative classes was accomplished using the following guidelines: the distinction between deciduous and evergreen category of vegetation, herbaceous crops, and shrubs was made by using images captured in different seasons. The leaves of deciduous trees disappear during the fall season or dry season depending on the climate zone and crops are subjected to a crop cycle. Shrubs and trees were differentiated with the help of the timeline and the length of the shade in early morning and late afternoon images. In addition, the shape of the shade was also used to help with the identification of coniferous trees, which tend to appear as a conical structure while the broadleaf trees tend to have a round crown. Due to limitations imposed by the pixel size, only trees with a crown diameter of greater than 2 m were considered as candidates for classification as tree and evaluated for shade length.

The computed fractional cover of each cell with the 19 GlobCover LULC classes and the fractional cover of each LULC class with the 4 plant function types (Table 4.3) were used to calculate the fraction for 4 PFT (Broadleaf trees, Needleleaf trees, Shrubs, and herbs) classes used in MEGAN

2.04 model. The isoprene emission potential was derived from the 4 PFTs as described in (Guenther et al., 2006).

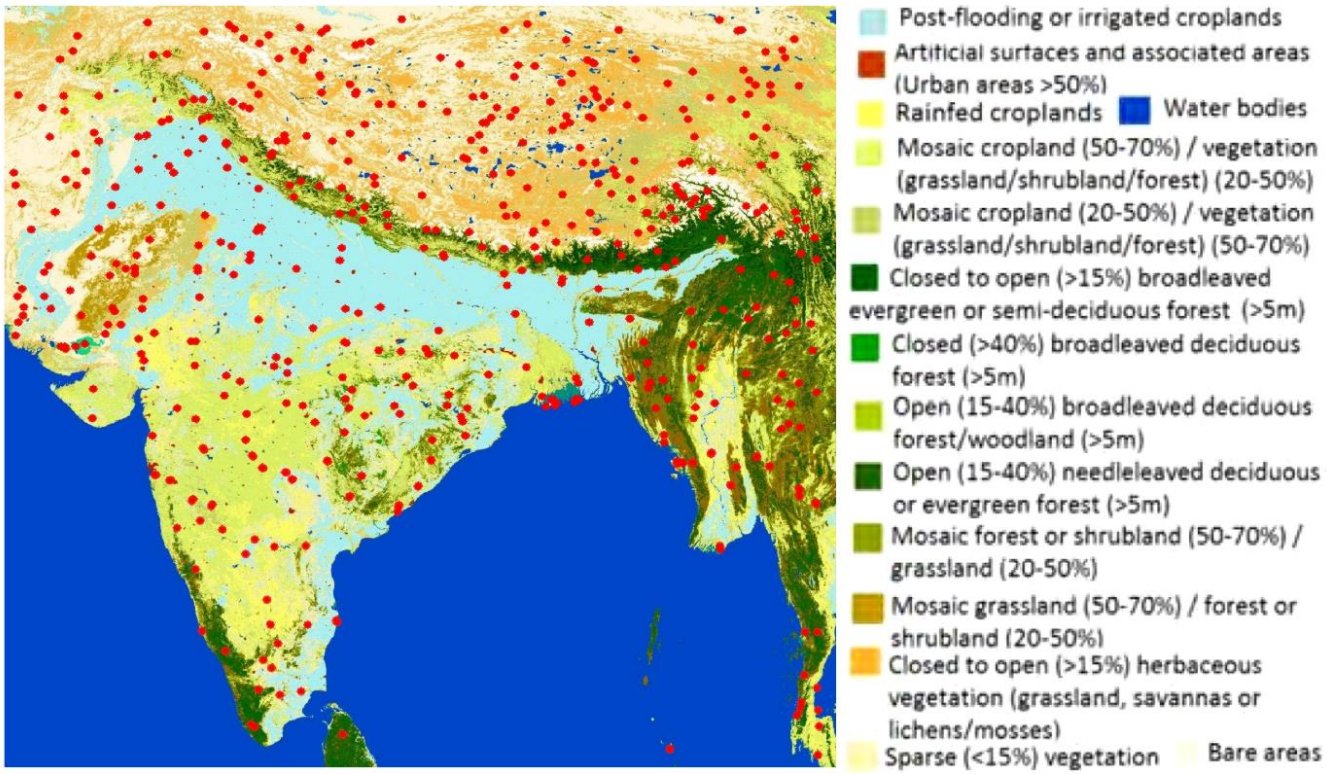

Figure 4.4 Locations of the pixels for which manual photo-interpretation was performed superimposed on the Globcover LULC map of South Asia.

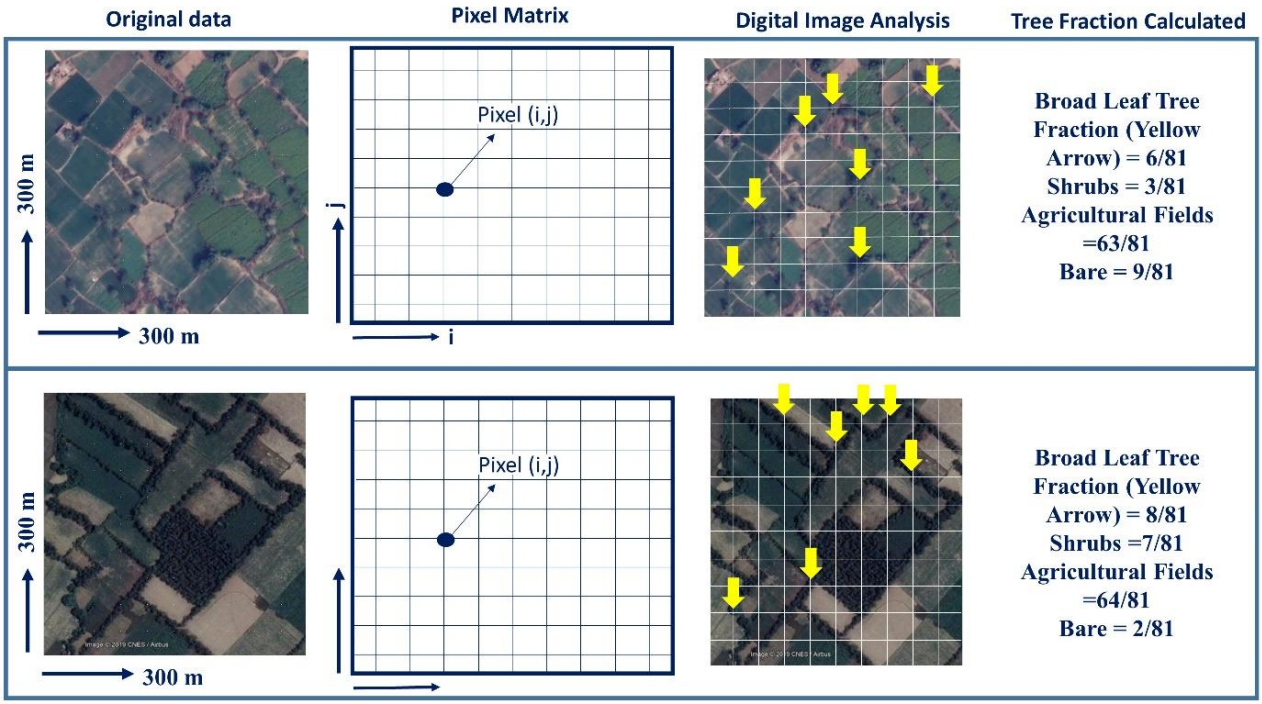

Figure 4.5 Principles and calculation of vegetation fraction. The plant function type is determined by spot counting. Where the interception of the cell grid (pointed as arrow) matches with the corresponding vegetation class (in this case broadleaf tree) match is scored, the fourth column shows the calculation for two datasets (a1, a2) for tree fraction calculation.

4.6 WRF-Chem model configuration

One month of data from 1st August 2012 to 31st August 2012 during the monsoon season was studied in detail using 3D simulations with a weather research and forecasting model coupled with Chemistry (WRF-Chem). We chose the WRF-Chem Model for this study as it is one of the most widely used and well validated chemical transport models over South Asia (Kumar et al. 2012, Ghude et al. 2017). We believe that it is advantageous to use this model for emphasizing the missing process to ensure other researchers can quickly incorporate our findings into their research. It simulates the mixing, transport, emissions, chemical transformations of gases and aerosols concurrently with the meteorology (Fast et al., 2006;Grell et al., 2005). A 1000 x 1000 km^2 domain centered on 30.667° N, 76.729° E with horizontal grid of 10 km and 51 vertical levels (surface upto ~10 hPa) was set up with a 3 days spin-up time. This modelling domain is shown as a red square in Figure 4.2. The initial and lateral boundary conditions for meteorological fields were taken from National Centre for Environment Predictions final analysis fields available every

6 hours at a spatial resolution of 1° x 1° (Data Archive at National Center for Atmospheric Research, CIS Laboratory 2000) while fields such as albedo, vegetation fraction, soil classification and terrain height were taken from the Modified IGBP MODIS 20-category vegetation land use dataset (Friedl et al., 2010). We use the Noah land surface module (Chen and Dudhia, 2001) with the Yonsei University (YSU) planetary boundary layer scheme (Hong et al., 2006), Rapid Radiative Transfer Model for General Circulation Models radiative transfer module (Mlawer et al., 1997), Fast J photolysis scheme (Fast et al., 2006), the Morrison (2-moment) microphysics scheme (Morrison et al., 2005) and the Grell 3D ensemble convective parameterization (Grell and Dévényi, 2002). Anthropogenic emissions for CO, NO_x, SO_2, NH_3, OC, and BC, and NMVOC were taken from the Emission Database for Global Atmospheric Research (EDGAR v4.3.2) (Crippa et al., 2018), daily varying emissions of trace gas species from biomass burning are taken from the NCAR (FINN) v1 fire inventory (Wiedinmyer et al., 2011). Biogenic emissions of gases and aerosols are calculated online using MEGAN Model version 2.04 (Guenther et al., 2006). This study utilizes the chemical mechanism represented by the MOZCART chemical scheme (Chemical opt =112) (Emmons et al., 2010; Pfister et al., 2013), which includes 81 chemical species involved in 159 gas phase and 38 photolysis reactions. Aerosols in the MOZCART mechanism are represented using the Global Ozone Chemistry Aerosol Radiation and Transport (GOCART) scheme. The chemical initial and lateral boundary conditions were provided by archived datasets of MOZART-4 global 3D chemical transport model (Emmons et al., 2010).

The WRF-Chem model has the option of nudging the model towards temporally and spatially interpolated analyses of meteorological variables using relaxation terms for simulations (Stauffer and Seaman, 1990; Stauffer and Seaman, 1994). At present in WRF-Chem model nudging can be applied to east-west component of wind (u), north-south component of wind (v), potential temperature (temp) and water vapor mixing ratio (Q_{vapour}). The application of analysis nudging to the simulation, avoids errors in transport of chemical species and is very useful in atmospheric chemistry simulations. This feature can be very useful for atmospheric chemistry simulations to avoid errors in transport of chemical species. In all our model runs nudging was switched off below the model level 15 (~2 km). Therefore, no nudging of u and v wind vectors, temperature and water vapor mixing ratio was applied within the planetary boundary layer. For the upper atmospheric layers above ~2 km , the nudging interval was set to 6 hrs, with nudging coefficients for temperature, moisture and wind being 6×10^{-4} s^{-1}. The coefficients were determined on the basis

of different sensitivity simulations while configuring the model domain over the north-west Indo-Gangetic Plain.

The Noah land surface module is based on the Moderate Resolution Imaging Spectroradiometer - International Geosphere-Biosphere Programme (MODIS-IGBP) vegetation dataset in its calculations and calculates leaf area index (LAI) and albedo based on vegetation types and fractions. The changes made in the improved vegetation classes in the MEGANv2.04 biogenic modules were incorporated in the Noah land surface module by re-computing different secondary parameters in "VEGPARM.TBL" (Table 4.4) for the croplands to make it representative of the agroforestry practices over N.W Indo Gangetic plains. In addition, the changes were also incorporated in the WRF initial condition files. The changed values for the improved Noah land surface cover with 10% trees are provided in Table 4.5 and those for the simulation with 50% trees in croplands are provided in Table 4.6.

Using the improved tree cover representation in the existing model setup, the following model simulations were performed:

1. Default: Default configuration of the model without aerosol-radiation feedbacks

2. Improved: Improved model configuration with the modified tree cover of 10% in croplands both in the MEGAN and in the Noah land surface module without aerosol-radiation feedbacks.

3. Improved with aerosol feedback: Improved model configuration with the modified tree cover of 10% in croplands both in the MEGAN and in the Noah land surface module with aerosol-radiation feedbacks on.

4. Hypothetical 50% tree cover: Model configuration with a modified tree cover of 50% in croplands both in the MEGAN and in the Noah land surface module without aerosol radiation feedbacks. We calculate this scenario assuming that areas presently identified as cropland will be planted with 25% broadleaf evergreen trees (e.g. Citrus, Guava, Litchi, Mango, Olive), 25% broadleaf trees (e.g. poplar, teak) and 40% crops and will retain 5% shrubs, 3% grasslands and 3% urban and build-up area.

Table 4.4 Vegetation parameters for Modified IGBP MODIS Noah dataset in Noah land surface model: default case

VEGETATION TYPE	SHDFAC	NROOT	RS	RGL	HS	SN_{UP}	MAXALB	LAI_{MIN}	LAI_{MAX}	$EMISS_{MIN}$	$EMISS_{MAX}$	$ALBEDO_{MIN}$	$ALBEDO_{MAX}$	Z_{0MIN}	Z_{0MAX}	Z_{TOPV}	Z_{BOTV}
Evergreen Needleleaved Forest	0.7	4	125	30	47.35	0.08	52	5.00	6.40	0.95	0.95	0.12	0.12	0.5	0.5	17	8.5
Evergreen Broadleaved Forest	0.95	4	150	30	41.69	0.08	35	3.08	6.48	0.95	0.95	0.12	0.12	0.5	0.5	35	1
Deciduous Needleleaved Forest	0.7	4	150	30	47.35	0.08	54	1.00	5.16	0.93	0.94	0.14	0.15	0.5	0.5	14	7
Deciduous Broadleaved Forest	0.8	4	100	30	54.53	0.08	58	1.85	3.31	0.93	0.93	0.16	0.17	0.5	0.5	20	11.5
Mixed Forest	0.8	4	125	30	51.93	0.08	53	2.80	5.50	0.93	0.97	0.17	0.25	0.2	0.5	18	10
Closed Shrubland	0.7	3	300	100	42.00	0.03	60	0.50	3.66	0.93	0.93	0.25	0.30	0.01	0.05	0.5	0.1
Open Shrubland	0.7	3	170	100	39.18	0.035	65	0.60	2.60	0.93	0.95	0.22	0.30	0.01	0.06	0.5	0.1
Woody Savannah	0.7	3	300	100	42.00	0.03	60	0.50	3.66	0.93	0.93	0.25	0.30	0.01	0.05	0.5	0.1
Savannah	0.5	3	70	65	54.53	0.04	50	0.50	3.66	0.92	0.92	0.2	0.20	0.15	0.15	0.5	0.1
Grassland	0.8	3	40	100	36.35	0.04	70	0.52	2.90	0.92	0.96	0.19	0.23	0.1	0.12	0.5	0.01
Wetland	0.6	2	70	65	55.97	0.015	59	1.75	5.72	0.95	0.95	0.14	0.14	0.3	0.3	0	0
Crop	0.8	3	40	100	36.25	0.04	66	1.56	5.68	0.92	0.985	0.17	0.23	0.05	0.15	0.5	0.01
Urban and Built-up	0.1	1	200	999	999	0.04	46	1.00	1.00	0.88	0.88	0.15	0.15	0.5	0.5	0	0
Crop natural vegetation	0.8	3	40	100	36.25	0.04	68	2.29	4.29	0.92	0.98	0.18	0.23	0.05	0.14	0.5	0.01
Ice and snow	0	1	999	999	999	0.02	82	0.01	0.01	0.95	0.95	0.55	0.70	0.001	0.001	0	0
Barren and sparse	0.01	1	999	999	999	0.02	75	0.10	0.75	0.9	0.9	0.38	0.38	0.01	0.01	0.02	0.01
Water	0	0	100	30	51.75	0.01	70	0.01	0.01	0.98	0.98	0.08	0.08	0.0001	0.0001	0	0
Wooden Tundra	0.6	3	150	100	42	0.025	55	0.41	3.35	0.93	0.93	0.15	0.20	0.3	0.3	10	0.1
Mixed Tundra	0.6	3	150	100	42	0.025	60	0.41	3.35	0.92	0.92	0.15	0.20	0.15	0.15	5	0.1
Barren Tundra	0.3	2	200	100	42	0.02	75	0.41	3.35	0.9	0.9	0.25	0.25	0.05	0.1	0.02	0.01

Table 4.5 Vegetation parameters for Modified IGBP MODIS Noah dataset in Noah land surface model – improved 10% tree cover case

VEGETATION TYPE	SHDFAC	NROOT	RS	RGL	HS	SN_{UP}	MAXALB	LAI_{MIN}	LAI_{MAX}	EMISS MIN	EMISS MAX	ALBEDO MIN	ALBEDO MAX	Z_{0MIN}	Z_{0MAX}	Z_{TOPV}	Z_{BOTV}
Evergreen Needleleaved Forest	.70	4	125	30	47.35	0.08	52	5.00	6.40	.950	.950	.12	.12	.50	.50	17.0	8.5
Evergreen Broadleaved Forest	.95	4	150	30	41.69	0.08	35	3.08	6.48	.950	.950	.12	.12	.50	.50	35.0	1.0
Deciduous Needleleaved Forest	.70	4	150	30	47.35	0.08	54	1.00	5.16	.930	.940	.14	.15	.50	.50	14.0	7.0
Deciduous Broadleaved Forest	.80	4	100	30	54.53	0.08	58	1.85	3.31	.930	.930	.16	.17	.50	.50	20.0	11.5
Mixed Forest	.80	4	125	30	51.93	0.08	53	2.80	5.50	.930	.970	.17	.25	.20	.50	18.0	10.0
Closed Shrubland	.70	3	300	100	42.00	0.03	60	0.50	3.66	.930	.930	.25	.30	.01	.05	0.50	0.10
Open Shrubland	.70	3	170	100	39.18	0.035	65	0.60	2.60	.930	.950	.22	.30	.01	.06	0.50	0.10
Woody Savannah	.70	3	300	100	42.00	0.03	60	0.50	3.66	.930	.930	.25	.30	.01	.05	0.50	0.10
Savannah	.50	3	70	65	54.53	0.04	50	0.50	3.66	.920	.920	.20	.20	.15	.15	0.50	0.10
Grassland	.80	3	40	100	36.35	0.04	70	0.52	2.90	.920	.960	.19	.23	.10	.12	0.50	0.01
Wetland	.60	2	70	65	55.97	0.015	59	1.75	5.72	.950	.950	.14	.14	.30	.30	0.00	0.00
Crop	.70	2	50	80	39.25	0.03	59	2.1	5.8	.930	.975	.16	.22	.10	.20	2.00	1.00
Urban and Built-up	.10	1	200	999	999.0	0.04	46	1.00	1.00	.880	.880	.15	.15	.50	.50	0.00	0.00
Crop natural vegetation	.80	3	40	100	36.25	0.04	68	2.29	4.29	.920	.980	.18	.23	.05	.14	0.50	0.01
Ice and snow	.00	1	999	999	999.0	0.02	82	0.01	0.01	.950	.950	.55	.70	0.001	0.001	0.00	0.00
Barren and sparse	.01	1	999	999	999.0	0.02	75	0.10	0.75	.900	.900	.38	.38	.01	.01	0.02	0.01
Water	.00	0	100	30	51.75	0.01	70	0.01	0.01	.980	.980	.08	.08	0.0001	0.0001	0.00	0.00
Wooden Tundra	.60	3	150	100	42.00	0.025	55	0.41	3.35	.930	.930	.15	.20	.30	.30	10.0	0.10
Mixed Tundra	.60	3	150	100	42.00	0.025	60	0.41	3.35	.920	.920	.15	.20	.15	.15	5.00	0.10
Barren Tundra	.30	2	200	100	42.00	0.02	75	0.41	3.35	.900	.900	.25	.25	.05	.10	0.02	0.01

Table 4.6 Vegetation parameters for Modified IGBP MODIS Noah dataset in Noah land surface model – hypothetical 50% tree cover case

VEGETATION TYPE	SHDFAC	NROOT	RS	RGL	HS		SN_{UP}	MAXALB	LAI_{MIN}	LAI_{MAX}	EMISS MIN	EMISS MAX	ALBEDO MIN	ALBEDO MAX	Z_{0MIN}	Z_{0MAX}	Z_{TOPV}	Z_{BOTV}
Evergreen Needleleaved Forest	.70	4	125	30.	47.35		0.08	52.	5.00	6.40	.950	.950	.12	.12	.50	.50	17.0	8.5
Evergreen Broadleaved Forest	.95	4	150	30.	41.69		0.08	35.	3.08	6.48	.950	.950	.12	.12	.50	.50	35.0	1.0
Deciduous Needleleaved Forest	.70	4	150	30.	47.35		0.08	54.	1.00	5.16	.930	.940	.14	.15	.50	.50	14.0	7.0
Deciduous Broadleaved Forest	.80	4	100	30.	54.53		0.08	58.	1.85	3.31	.930	.930	.16	.17	.50	.50	20.0	11.5
Mixed Forest	.80	4	125	30.	51.93		0.08	53.	2.80	5.50	.930	.970	.17	.25	.20	.50	18.0	10.0
Closed Shrubland	.70	3	300	100.	42.00		0.03	60.	0.50	3.66	.930	.930	.25	.30	.01	.05	0.50	0.10
Open Shrubland	.70	3	170	100.	39.18		0.035	65.	0.60	2.60	.930	.950	.22	.30	.01	.06	0.50	0.10
Woody Savannah	.70	3	300	100.	42.00		0.03	60.	0.50	3.66	.930	.930	.25	.30	.01	.05	0.50	0.10
Savannah	.50	3	70	65.	54.53		0.04	50.	0.50	3.66	.920	.920	.20	.20	.15	.15	0.50	0.10
Grassland	.80	3	40	100.	36.35		0.04	70.	0.52	2.90	.920	.960	.19	.23	.10	.12	0.50	0.01
Wetland	.60	2	70	65.	55.97		0.015	59.	1.75	5.72	.950	.950	.14	.14	.30	.30	0.00	0.00
Crop	.60	3	70	60.	42.25		0.05	51.	2.60	6.00	.940	.960	.15	.20	.20	.35	2.50	1.50
Urban and Built-up	.10	1	200	999.	999.0		0.04	46.	1.00	1.00	.880	.880	.15	.15	.50	.50	0.00	0.00
Crop natural vegetation	.80	3	40	100.	36.25		0.04	68.	2.29	4.29	.920	.980	.18	.23	.05	.14	0.50	0.01
Ice and snow	.00	1	999	999.	999.0		0.02	82.	0.01	0.01	.950	.950	.55	.70	0.001	0.001	0.00	0.00
Barren and sparse	.01	1	999.	999.	999.0		0.02	75.	0.10	0.75	.900	.900	.38	.38	.01	.01	0.02	0.01
Water	.00	0	100.	30.	51.75		0.01	70.	0.01	0.01	.980	.980	.08	.08	0.0001	0.0001	0.00	0.00
Wooden Tundra	.60	3	150.	100.	42.00		0.025	55.	0.41	3.35	.930	.930	.15	.20	.30	.30	10.0	0.10
Mixed Tundra	.60	3	150.	100.	42.00		0.025	60.	0.41	3.35	.920	.920	.15	.20	.15	.15	5.00	0.10
Barren Tundra	.30	2	200.	100.	42.00		0.02	75.	0.41	3.35	.900	.900	.25	.25	.05	.10	0.02	0.01

4.7 Metrics used for WRF-Chem model evaluation

In the following "M" and "O" terms signify model and observed/reanalyses values, respectively.

We used Mean Bias (MB),

$$\text{MB} = \frac{1}{N}\sum_{i=1}^{N}\left(M_i - O_i\right) \quad (1)$$

Normalized Mean Bias (NMB)

$$\text{NMB} = \frac{1}{N}\frac{\sum_{i=1}^{N}\left(M_i - O_i\right)}{\sum_{i=1}^{N} O_i} \times 100 \quad (2)$$

Mean Absolute Gross Error (MAGE)

$$\text{MAGE} = \frac{1}{N}\sum_{i=1}^{N}\left|M_i - O_i\right| \quad (3)$$

and Mean Normalized Gross Error (MNGE)

$$\text{MNBE} = \frac{1}{N}\frac{\sum_{i=1}^{N}\left|M_i - O_i\right|}{\sum_{i=1}^{N} O_i} \times 100 \quad (4)$$

to validate the WRF-Chem model output against hourly observations from the IISER Mohali Atmospheric Chemistry facility for the default run, improved run and improved run with aerosol feedback. However, the available observational data allows us to evaluate the model output only for one of the grid cells within the modelling domain. To validate the model output over the full modelling domain we use the fifth generation of reanalysis dataset (ERA5) (C3S, 2017) of global climate from European centre for medium range weather forecast (ECMWF). ERA5 data is available at a spatial resolution of 0.25°×0.25° and hourly temporal resolution. ERA5 data is bilinearly interpolated using climate data operator (CDO) on the WRF-Chem simulation grid for inter-comparison. We chose this dataset over Modern-Era Retrospective analysis for Research and Applications (MERRA 2) (0.625°-0.5°) due to its superior spatial resolution and the 4D Var advanced-data assimilation system of ECMWF used to create the dataset. Several studies have shown that ERA5 performs better against observation datasets (Hersbach et al., 2020; Olauson, 2018).

4.8 Results and discussion

4.8.1. Model evaluation

We evaluate the model performance for the default and improved model runs using the hourly modelled temperature, boundary layer height, horizontal wind speed and absolute humidity as well as the hourly averaged mixing ratios of ozone, isoprene, and the oxidation products of isoprene, namely methyl vinyl ketone and methacrolein (Table 4.7). We compute Mean Bias (MB), Normalized Mean Bias (NMB), Mean Absolute Gross Error (MAGE) and Mean Normalized Gross Error (MNGE) with respect to in-situ observations over the measurement site in Mohali as described in Section 4.3.1 Table 4.7 shows, that for the default run the planetary boundary layer, isoprene and ozone have the highest NMB (>40%) and MNGE (>70%) among all parameters. Introducing 10% tree cover into croplands results in substantial reductions of the NMB for these three parameters (<10%) indicating that the missing trees were responsible for the discrepancy in the default run.

Table 4.7 Comparison of WRF-Chem simulations for August 2012 against ground based measurements of ambient temperature, absolute humidity and wind speed at the IISER Mohali atmospheric chemistry facility and against ERA 5 planetary boundary layer height. D stands for default run, I for improved run and I-A for improved run with aerosol feedback.

Variable	Mean Bias			Normalized Mean Bias			Mean Absolute Gross Error			Mean Normalized Gross Error		
Model run	D	I	I-A	D	I	I-A	D	I	I-A	D	I	I-A
Temperature (K)	1.0	0.8	-0.5	0.3 %	0.3 %	-0.2%	1.9	1.5	1.7	0.6 %	0.5%	0.5%
Absolute humidity (g/m^3)	-1.8	-0.6	-0.5	-9.0%	-2.6%	-2.2%	2.2	1.5	1.4	11.4%	6.9%	6.7%
Wind Speed (m/s)	-1.6	-1.4	-1.3	-38.9%	-32.1%	-30.5%	2.2	2.1	2.1	52.1%	49.6%	48.8%
Planetary Boundary Layer (m)	220	29	-35	65.3%	8.7%	-10.4%	258	180	153	76.2%	53.3%	45.2%
Isoprene (ppb)	-1.0	-0.1	1.0	-73.9%	4.9%	86.4%	1.0	0.7	1.1	75.1%	53.1%	78.8%
MVK+MACR (ppb)	0.04	0.3	0.7	5.1%	35.8%	105.6%	0.5	0.4	0.8	68.9%	63.1%	112.1%
Ozone (ppb)	8.5	-0.1	-3.6	43.5%	-0.3%	-18.4%	14.2	10.1	9.0	72.5%	51.80%	45.8%

To investigate whether the improvements in the monthly average MB are due to improved representation of daytime photosynthesis related processes, we plot the day time data for both the improved and the default model run versus the observations (Figure 4.6 A-D). For this analysis, the modelled data from the default (shown in gold), improved model simulation with cropland trees (shown in green) were extracted and interpolated to the coordinates of our observational site from 9 am to 4 pm local time to derive daily averages and compared with the similarly daily

averaged measured data from the IISER Mohali facility. Each dot represents one day and "m" stands for the slope of the line. It can be seen that the modelled planetary boundary layer height is no longer strongly overestimated with the slope for improved model data and ERA5 data falling onto the 1:1 line (m=1.0, Figure 4.6B) for the improved land cover. Figure 4.6B shows that the bias for the daytime boundary layer reduces substantially from ~400 m to ~70 m. Figure 4.6C illustrates that whereas the default model without cropland tree cover was significantly underestimating the measured daytime isoprene (m=0.3), the improved model simulation performs better and the slope of the model –measurements regression line is significantly improved (m=0.9; Figure 4.6 C). Similarly, the slope for the sum of isoprene oxidation products methacrolein and methyl vinyl ketone improve from m= 0.5 to m= 1 (Figure 4.6 D) and overall the agreement between modelled and measured absolute humidity is good (m=1.1; Figure 4.6 A). We also extract the hourly modelled data from the default (shown in gold), improved model simulation with cropland trees (shown in green) and the hourly ERA5 data (shown in grey) which we compare with the measured temperature (shown in blue) for the month of August 2012 (Figure 4.7 A). This time series reveals that despite the relatively small mean temperature bias of the default model run, the daytime temperature on certain days can be overestimated by 2-3 K while the nighttime temperature is being underestimated by similar magnitude on other days. This causes cancelation errors that reduce the Mean Bias (MB). It can be seen that the improved model reproduces the amplitude of the diurnal temperature variation much better, despite the fact that this improvement reduces MB only marginally. For several parameters such as PBL, isoprene and ozone the improvements in MB are much greater than the improvement of the MNGE, which drops only 70% to 50%. The magnitude of MAGE and MNGE appears to be driven mostly by model-observation mismatch in cloud cover over this grid cell with cloudy days that appear as clear sky days within the model, causing an overestimation of the surface temperature, ozone and PBL height within the model. The reverse situation causes an underestimation of the surface temperature, ozone and PBL height. Figure 4.7 B clearly shows that with inclusion of the cropland trees, the MB for ozone drops to almost zero and magnitude of the diurnal cycle for ozone is captured much better by the improved rather than the default model. It also shows that despite higher isoprene, the peak daytime ozone is lower by up to 20 ppb, a very significant result which indicates that cropland trees are mitigating ozone induced crop yield losses. When the aerosol feedback is switched on within the improved model, the model develops a small negative mean

bias for both temperature (-0.5° K), ozone (-3.5 ppb) and planetary boundary layer height (-35 m), due to an increase in observed clear sky days that are treated as days with cloud cover within the model.

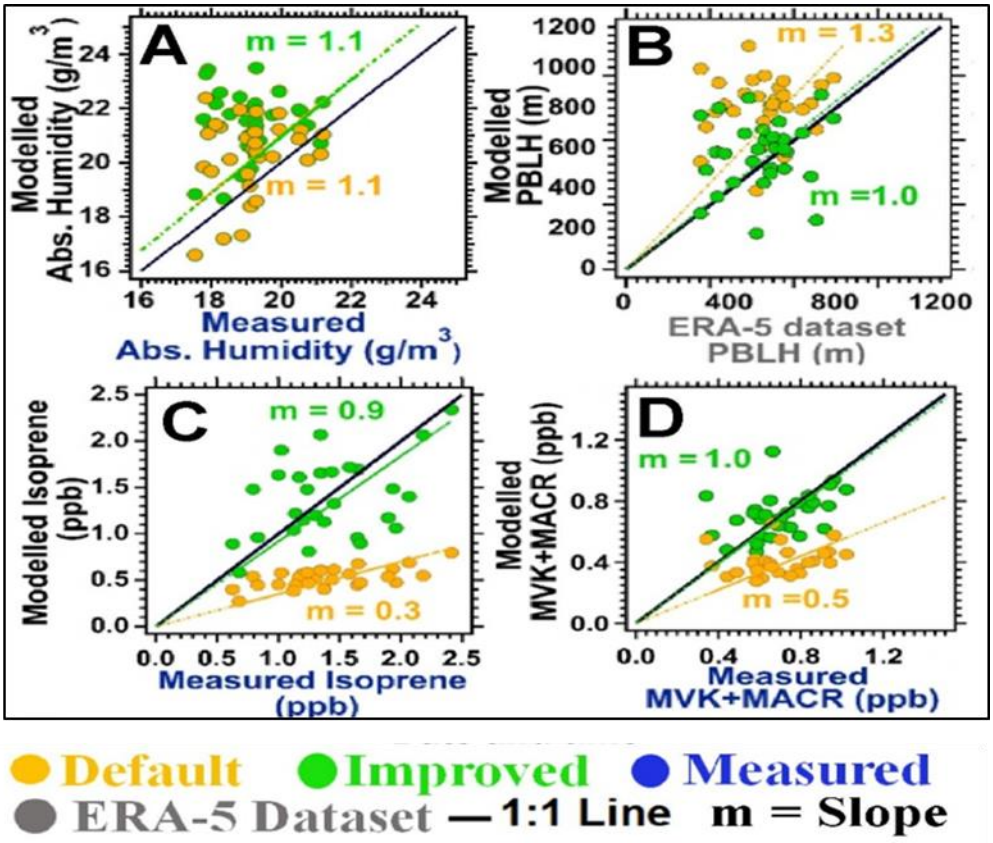

Figure 4.6 Improvement of the model-measurement agreement after incorporating revised tree cover into MEGAN and the Noah land surface module. Model-measurement agreement of the 7-hour average daytime (9 am to 4 pm) absolute humidity (A), isoprene mixing ratio (C) and MVK+MACR mixing ratios (D) for the default and improved model extracted over Mohali. Each dot represents one day and m stands for the slope of the line. (B) Model-ERA-5 agreement of the 7-hour average daytime (9 am to 4 pm) planetary boundary layer height for the default and improved model extracted over Mohali. Each dot represents one day and m stands for the slope of the line

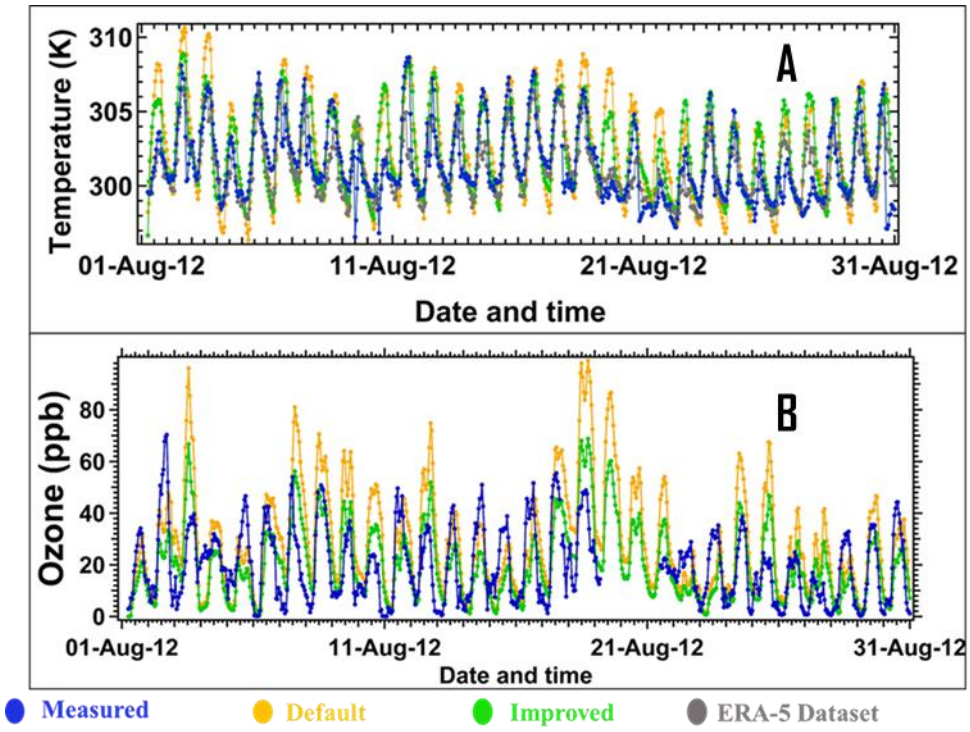

Figure 4.7 (A) Time series of the measured, default model, improved model and ERA-5 temperature extracted over Mohali. (B) Time series of the measured, default model and improved model ozone mixing ratio extracted over Mohali.

To investigate the impact of the model performance for simulating regional atmospheric dynamics related parameters, in Figure 4.8 we evaluate the spatial changes over the modelling domain for the three different WRF-Chem model runs against the ERA5 (Hersbach et al., 2020) planetary boundary layer height and temperature dataset over the region for August 2012. Both model and ERA5 hourly values were averaged for the full month using the daily daytime period 9 am to 4 pm local time for each pixel (10x 10 km^2). It can be seen that inclusion of the trees in the model improves the model performance and reduces positive MB of the daytime boundary layer and temperature with the ERA5 dataset, not just for our grid cell but the modelling domain. Both the planetary boundary layer height and ambient temperature, which were being overestimated in default (Figure 4.8 A and D) case due to the missing evapotranspiration feedback, are now more accurate in the model simulations that account for the cropland trees (Figure 4.8 B and E). The effect is significant with regional changes typically as large as 300-500 m for lower modelled boundary layer heights and 2-3 ℃ for the ambient daytime temperature. It can be also seen that activation of the aerosol effect introduces a small negative bias in PBL (Figure 4.8 C) and surface temperature (Figure 4.8 F) across most of the modelling domain, possibly due to an overestimation of the cloud cover within the domain.

Thus to summarize, inclusion of the cropland tree cover was found to significantly improve the model performance relative to observations both spatially and temporally for daytime temperature, boundary height, ozone, isoprene and its oxidation products. The improved capability to reproduce the observed boundary layer dynamics, ozone mixing ratios and surface temperatures have important implications, in particular for studies evaluating the impact of heat stress (Battisti and Naylor, 2009; Deutsch et al., 2018) and tropospheric ozone (Carter et al., 2017; Tai et al., 2014) on food security, air quality and human health. However, present efforts for exploring the potential of permaculture, silvi-pastoralism, and agroforestry on increased carbon sequestration, crop production and farmer income (Reij and Garrity, 2016, Kuyah et al. 2019) have not received sufficient attention. Future research should explore the magnitude of potential co-benefits of such agricultural interventions that include reductions in heat and air pollution related mortality (Mitchell et al., 2018; Silva et al., 2017), improved workforce productivity (Dunne et al., 2013), reduced soil erosion (Kuyah et al., 2019) and improved water management (Golfam, et al. 2019).

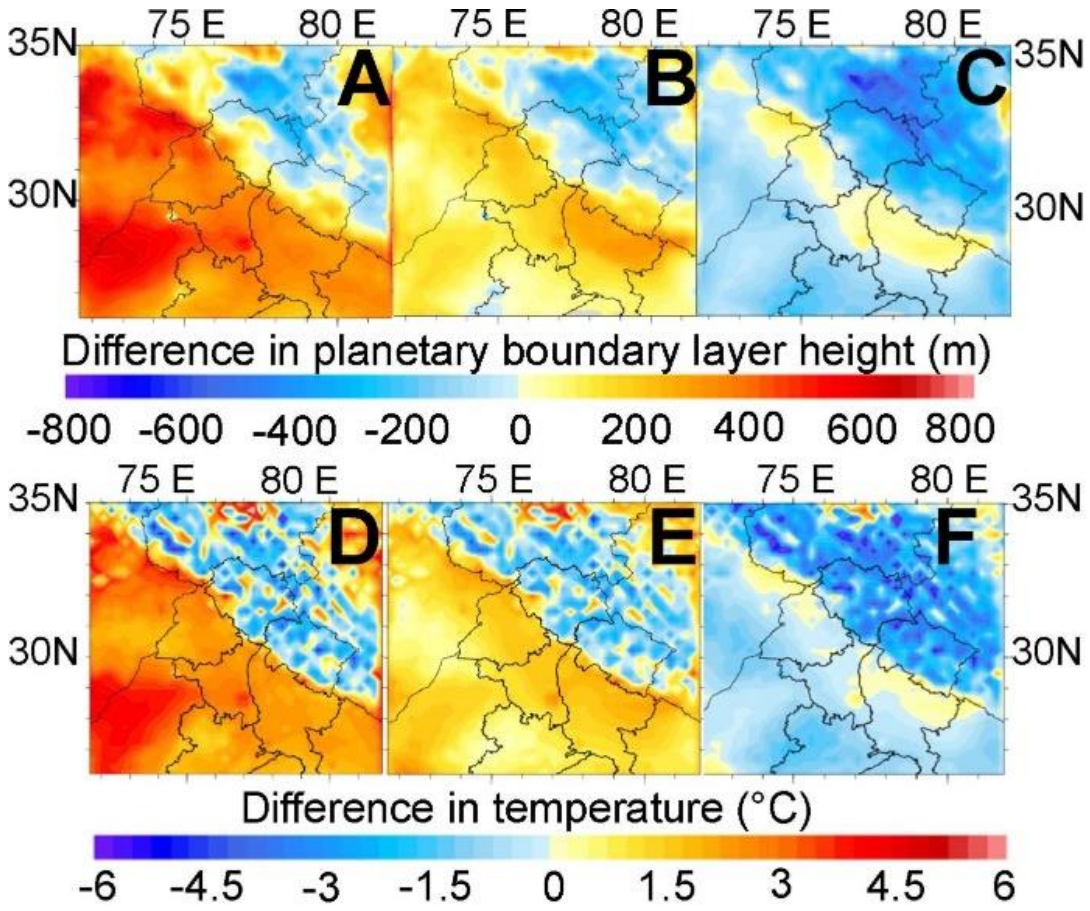

Figure 4.8 Improvement of the model-measurement of spatial patterns of temperature and planetary boundary layer height for our modelling domain after incorporating revised tree cover into MEGAN and the Noah land surface module. A) Difference between default model PBL and ERA-5 PBL height (Default-ERA5). (B) Differences between improved model PBL and ERA-5 PBL height (Improved-ERA5) (C) Differences between improved model with aerosol radiation feedback PBL and ERA-5 PBL height (Improved w. aerosol-ERA5). (D) Difference between default model average temperature and ERA-5 average temperature (Default-ERA5). (E) Differences between improved model average temperature and ERA-5 average temperature (Improved - ERA5). (F) Differences between improved model with aerosol radiation feedback average temperature and ERA-5 average temperature (Improved w. aerosol - ERA5).

4.8.2 Impact of cropland trees on modelled meteorology and composition

We examine monthly-averaged model results (Figure 4.9) of surface sensible heat flux (A), latent heat flux (B), isoprene flux (C), planetary boundary layer height (D), and the monthly sum of the rainfall (E) of the default model run without aerosol radiation feedback and compare these results with the improved/more realistic model configuration that has the modified tree cover of 10% in croplands both in the MEGAN and in the Noah land surface module, but also without aerosol-radiation feedbacks. Updating the tree cover (difference of 10%) relative to the default version tree cover of 0-1% trees in crop lands results in very significant effects. While the latent heat flux

increases by 100% to 300% over croplands in Punjab and Haryana, the sensible heat flux decreases by 50% to 100%. The planetary boundary layer height decreases by 10 to 20% over Punjab and Haryana but increases by about 10% over Uttar Pradesh. The changes in boundary layer by 200-400 m has significant impacts for the air pollutant concentrations which could increase by a similar magnitude just due to reduction in the boundary layer driven dilution effect (van Stratum et al., 2012). Earlier Uttar Pradesh was considered to be mosaic cropland in the land surface module while the other two states were classified as ordinary cropland. Now both areas have been classified as ordinary croplands with 10% tree cover.

The increase in isoprene fluxes due to the higher tree cover was also very significant (60% to 70%). Poplar and eucalyptus have traditionally been cultivated as part of agroforestry with such trees providing additional benefits as wind breakers and shade to crops as well as additional income through wood products. The fraction of the agricultural land under poplar and eucalyptus agroforestry cultivation has experienced a significant increase in recent decades as a result of government crop diversification schemes that gave out several hundred thousand of eucalyptus and poplar saplings for free every year in the early 2000s in the Indian states of Punjab and Haryana. These trees are intercropped with all grain, pulse and vegetable crops, generating several million tonne y^{-1} of fresh wood with the total area under poplar alone over the Indian region currently exceeding 3200 km^2. Poplar, mango and eucalyptus trees are top isoprene emitters and the effect of the reactive isoprene emissions on regional atmospheric chemistry could be quite significant (Lelieveld et al., 2008). It is clear that evapotranspiration increase from the trees in addition to the crops is responsible for changes in the energy fluxes whereas the plant functional types present in the croplands are responsible for the increased isoprene emissions.

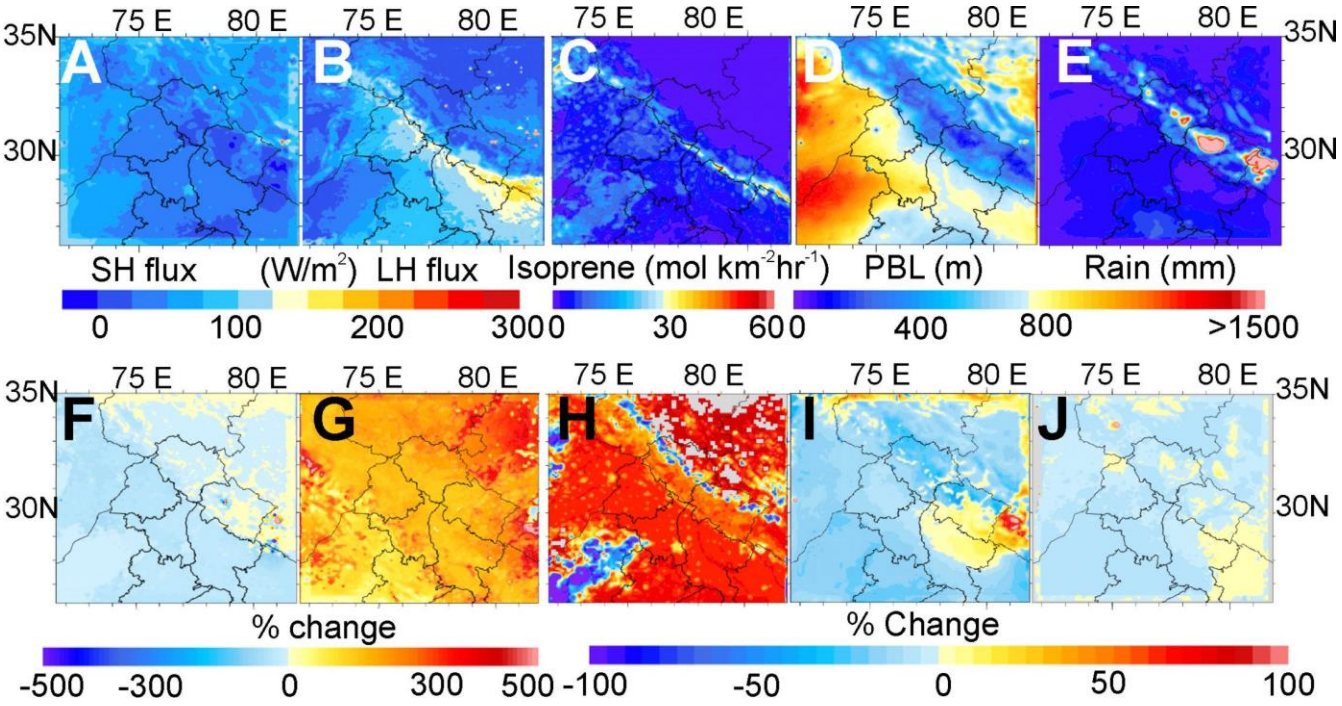

Figure 4.9 Monthly average sensible heat flux (A), latent heat flux (B), isoprene flux (C), planetary boundary layer height (D), and the monthly sum of the rainfall (E) of the default setup. Percentage changes in sensible heat flux (F), latent heat flux (G), isoprene flux (H), planetary boundary layer height (I), and rainfall (J) when changing from the default model setup to the improved model with cropland tree cover included((improved-default) * 100/default)

4.9 Model assessments of August monthly averaged differences in the 7-hour averaged (9 am to 4 pm) M7 ozone mixing ratios, temperature and rice crop yield losses for 10 % and 50% cropland tree cover over north-west Indo-Gangetic Plain

Figure 4.10 shows for August 2012 the monthly averaged differences in the 7-hour averaged (9 am to 4 pm) ozone mixing ratios (ΔM7) for model runs with 10% agroforestry and 50% agroforestry, respectively and the default tree cover, ((Figures 4.10 A and E), the peak daytime temperature (Figures 4.10 B and F), relative yield loss (RYL) calculated using the ozone crop yield loss relationship of Indian rice cultivars (Sinha et al., 2015) (Figures 4.10 C and G), and relative yield loss calculated using the temperature-induced grain sterility function by Weerakoon et al., 2008 (Figures 4.10 D and H). The average ozone from 9 am to 4 pm is known under the name M7 and is a standard World Meteorological Organization ozone exposure metric, for which the exposure-crop yield loss relationship has been well characterized (Mills et al. 2018). We find that

present day agroforestry practices (10% tree cover) reduces the daytime maximum temperature during rice panicle formation – a parameter which determines crop production loss due to flower sterility (Weerakoon et al., 2008) - by 1 to 2°C (Figure 4.10 B).

The seven-hour average ozone mixing ratio from 9 am to 4 pm (M7), which is used to determine ozone related crop production losses (Sinha et al., 2015) reduces by 2 to 3 ppb (Figure 4.10 B). Overall, the present-day tree cover reduces rice production losses due to heat stress and ozone by 10 to 20% (Figures 4.10 C and D) when compared to a scenario of croplands without any trees within them. With identical meteorological and chemical boundary conditions as drivers, an increase in the agroforestry cover of the Indo Gangetic Plain (IGP) from 10% (present day) to 50% would lower the regional peak daytime temperatures during rice panicle formation by up to 4°C (Figure 4.10 E) and the seven-hour average ozone mixing ratio from 9 am to 4 pm (M7) by up to 8 ppb (Figure 4.10 F). The combined effect should increase rice yields of short duration rice cultivars on the remaining 50% of the NW-IGP by up to 40% (Figures 4.10 G and H), primarily because heat stress is already a yield-limiting factor for rice production in the present day climate (Battisti and Naylor, 2009) and likely to become an even greater limitation in the future.

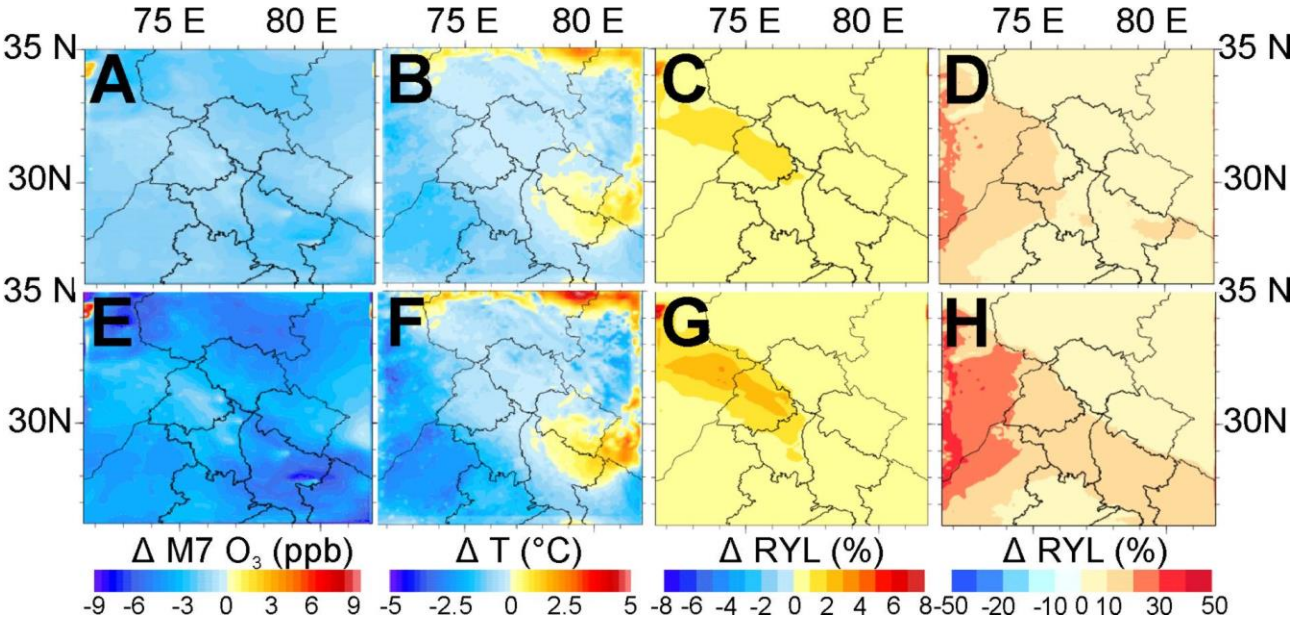

Figure 4.10 August monthly averaged change in parameters with a strong impact on rice yield with identical driving meteorology and boundary conditions after increasing agroforestry cover in the North West IGP From default to 10% (A-D) and from 10% (present) to 50% (E-H). (A) Change in the 7-hour average (9 am to 4 pm) ozone mixing ratio (ΔM7) (10% agroforestry – default tree cover). (B) Change in peak daytime temperature (10% Agroforestry – default tree cover). (C) Difference in relative yield loss (RYL) (10% Agroforestry – default tree cover) calculated using the ozone crop yield loss relationship of Indian rice cultivars (37). (D) Difference in relative yield loss (RYL) (10% Agroforestry – default tree cover) calculated using the temperature induced grain sterility function by Weerakoon et al. 2008 (38). (E) Change in the 7-hour average (9 am to 4 pm) ozone mixing ratio (ΔM7) (50% Agroforestry – 10% Agroforestry). (F) Change in peak daytime temperature (50% Agroforestry – 10% Agroforestry). (G) Difference in relative yield loss (RYL) (50% Agroforestry – 10% Agroforestry) calculated using the ozone crop yield loss relationship of Indian rice cultivars 37). (D) Difference in relative yield loss (RYL) (50% Agroforestry – 10% Agroforestry) calculated using the temperature induced grain sterility function by Weerakoon et al. 2008.

It should be noted that dedicating a plot to agroforestry does not mean regular crop production on that plot ceases. Winter crops such as wheat, pulses, oilseeds, certain herbs and spices, flowers and vegetables as well as shorter fruiting trees such as guava and citrus fruits continue to thrive under deciduous agroforestry trees (Chauhan et al., 2012). Once the trees reach a certain size, traditional monsoon season crops such as rice and sugarcane may suffer yield decreases once the shade offered by trees reduces the radiation reaching the crops, but it has been shown that maize, pulses, and certain vegetables continue to be profitable throughout the tree life cycle (Jain and Singh, 2000). Several studies have reported yield gains in agroforestry plots in comparison to control

plots for millets and maize grown under rain fed, drought prone and heat stressed conditions (Kuyah et al., 2019).

The capability of trees to favourably impact the microclimate in agricultural landscapes presents new climate change mitigation and adaption pathways. Currently the rice-wheat cultivation in the region requires intensive usage of groundwater for irrigation. Overall, our results suggest that parts of the NW IGP could substantially reduce the pressure on groundwater reserves (Rodell et al., 2019; Rodell et al., 2009) by increased cultivation of tree crops such as oil seeds (olives), fruits and timber with only a marginal drop in the net production of wheat and rice.

To calculate the total number of cropland trees in the world, we used the MOD44B tree count (Table 4.2) for various cropland classes, the global cropland area of 1.9-2.2 billion ha (Li et al., 2018; Yu et al., 2013; Zomer et al., 2016), and an assumed average crown diameter of 4-5 m for trees in croplands. We estimate that at present croplands contain 80 to 200 billion of all trees globally. If tree densities in global croplands were increased to those typical for farms practicing some form of agroforestry or permaculture (30 -400 ha^{-1}), the global tree cover on agricultural lands could be increased to 200-400 billion trees globally and the conversion efforts could sequester 0.3-30 Gt C per year (Nair et al., 2009; Roe et al., 2019). While these numbers may appear to be low in comparison to the 205 GtC that Bastin and co-workers proposed to store through the restoration of natural forest ecosystems (Bastin et al., 2019), sequestration rates of 10-30 GtC per year could potentially be sustained over long periods, without compromising the economic viability of farmlands, if the larger trees planted as part of the conversion efforts include species that are ultimately harvested and converted to long-lived consumer products or housing (Churkina et al., 2020) (e.g. *Swietenia mahagoni* or *Tectona grandis*). Lower sequestration rates of 0.3-0.5 GtC y^{-1} could be accomplished by convincing farmers to replace fences with hedges or include a few strategic wind breakers into the agricultural landscape, as generally practiced in the Indo Gangetic plain.

Global reforestation efforts have recently been proposed as a means to limit global warming below 1.5°C by capturing CO_2 (Bastin et al., 2019; Lewis et al., 2019), however, limiting the scope to the regeneration of natural ecosystems only may be too restrictive. Expanding reforestation efforts to include agroforestry in croplands would allow to bring much more area under forest cover globally. Obviously regional conditions will need to be taken into account for determining the best suitable

species for planting as cropland trees in consultation with the regional stakeholders. At the planning stage, modelling studies could be carried out for each region, to evaluate the potential impact of such plantations on regional climate and air quality.

4.10 Conclusion

As the recent farmer-driven expansion of agroforestry has brought 43% of the world's agricultural area to >10% tree cover (Zomer et al., 2016), the missing agroforestry trees must not only be included into regional air quality and weather models but also into global chemistry and climate models. This change would improve the model-measurement-agreement for boundary layer dynamics, moisture, energy fluxes and atmospheric chemistry. While our case study has been limited to north-west India, other regions, for example the Sahel zone in Africa, the area where the Three-North Shelter program was implemented to halt the advancement of the Gobi Desert in China, the Rio de la Plata basin in South America or Victoria and New South Wales in Australia may warrant future studies to evaluate the impact of changes in crop land tree cover on boundary layer dynamics, moisture and energy fluxes and atmospheric chemistry in such regions.

Chapter: 5

Conclusion: Major findings and future outlook

This study presents the first monsoon time dataset of isoprene, MVK+MACR, formaldehyde, and acetaldehyde from India. The influence of biomass burning sources was found to be negligible when compared with summertime conditions at the same site. Further, it was found that biogenic emissions were the major source of isoprene with photo-oxidation of isoprene also the major source of MVK+MACR. Formaldehyde and acetaldehyde which are ubiquitous hydrocarbons were found to have strong photochemical sources from the oxidation of hydrocarbons, including contribution from isoprene oxidation.

The high daytime isoprene over north-west Indo-Gangetic Plain was driven mainly by ambient temperature, it exhibited an exponential dependency with slope values similar to the ones observed from a tropical rainforest site. The farmers of north-west Indo-Gangetic Plain practice mixed agroforestry due to which the croplands have large swathes of poplar and eucalyptus growing at the periphery of croplands, which are strong isoprene emitters. These high isoprene emitting trees in the periphery of agricultural fields are the likely sources of high isoprene concentration during the monsoon season.

The relative contribution of the individual species (isoprene, acetaldehyde, formaldehyde, MVK+MACR) for monsoon and summer season revealed significantly higher mass concentrations for the month of monsoon. This is a very significant result as the summer season has been identified in the past to have the highest biogenic emission from different studies performed in higher northern latitudes. The strong isoprene emission during the monsoon season coupled with lower ventilation coefficient in monsoon relative to summer is the main reason is the reason for the highest biogenic emission observed in the monsoon season.

The WRF-Chem model was configured over north India. The model was optimized and configured to simulate the month of august and validated with ground-based measurements of isoprene and its oxidation products.

The default WRF-Chem modelled isoprene showed a strong under-prediction during the daytime. This under-prediction was due to missing daytime source of isoprene over the north-west Indo-Gangetic Plain. The missing source was identified as agroforestry trees. The issue of the missing cropland trees is also not limited to a specific land surface module and appears to be common to the land surface modules of several models used in the latest IPCC report. Next, I evaluated 15 global chemistry-climate models that took part in the Climate Model Intercomparison Project (CMPI5) which were used in assessment report 5. The evaluation shows that currently, only 5 out of the 15 global models use both the biogenic emission module and land surface module independently. While none of them account for cropland trees and the land use land cover is representative of the year 2000.

Next, I estimated the current fractional tree cover for different types of croplands on different continents using Moderate Resolution Imaging Spectroradiometer (MODIS) sensor derived Vegetation Continuous Fields (VCF) yearly product for the global representation of vegetation cover, namely MOD44B version-6, and the European Space agency GlobCover land use land cover (LULC) datasets. The calculation for different plant functional types was performed using manual spot counting and very high spatial resolution satellite images. The analysis showed that tree cover over intensely farmed regions in Asia, Australia, and South America is significantly underestimated (e.g. only 1-3% tree cover over North India) by the current chemistry-climate models.

Next, I included the actual tree cover (~10%) over the north-west Indo Gangetic Plain in the WRF-Chem model. The new model setup improved agreement between the modelled and measured temperature, boundary layer height, surface ozone which were earlier overestimated. The new model setup also improved agreement between measured and modelled isoprene and its oxidation products which were earlier underestimated. In this study I found that the surface latent heat flux alone increases by 100-300% while surface sensible heat flux reduces by 50-100%, leading to a reduction in daytime boundary layer height by 200-400 m which modulates air pollution. In this study, I also show that the trees in croplands mitigate peak daytime temperatures and ozone which improves rice production by 10-20%. Next, I showed that expanding agroforestry practices to 50% of the cropland area could result in up to 40% yield gain regionally. Therefore, future climate mitigation and food security efforts should consider stakeholder participation for

increased cropland agroforestry because of its beneficial effects. In all the simulations WRF-Chem model was nudged below the PBLH.

The current study focused primarily on improving the representation of vegetation in the MEGAN module and Noah land surface module during the monsoon season. However, the current WRF-Chem set up doesn't take into account the vegetation data while computing the dry deposition of different trace gases and VOCs which can be a limitation. It is worth mentioning here that the representation of vegetation data in the current WRF-Chem modelling system is quite tricky and sometimes difficult to follow. There are three different modules which are simulating different processes are using three different input vegetation datasets. The Noah land surface model and MEGAN model, both have their land-use dataset, similarly, the biomass burning emission module has its own. In my thesis, I have made the representation of vegetation data in the Noah land surface model complement with that of the MEGAN model as per the latest high-resolution satellite imagery over South Asia. These changes will also have to be incorporated over other parts of the globe and also to the biomass burning inventory. So that in the future only a single dataset can be used seamlessly across different modules.

Future studies should implement the improved model setup over other parts of the globe. Additionally, the improved model set up can also focus on high-resolution simulations over urban areas to accurately estimate heat stress and air pollution over different cities to come up with mitigation strategies. The what-if scenario discussed in chapter 4 of the thesis can be implemented for studying urban heat island effect and coming up with what-if scenarios for park cooling effects that are changing vegetation fraction in urban areas.

List of Figures

default model average temperature and ERA-5 average temperature (Default-ERA5). (E) Differences between improved model average temperature and ERA-5 average temperature (Improved - ERA5). (F) Differences between improved model with aerosol radiation feedback average temperature and ERA-5 average temperature (Improved w. aerosol - ERA5).

Figure 4.9 Monthly average sensible heat flux (A), latent heat flux (B), isoprene flux (C), planetary boundary layer height (D), and the monthly sum of the rainfall (E) of the default setup. Percentage changes in sensible heat flux (F), latent heat flux (G), isoprene flux (H), planetary boundary layer height (I), and rainfall (J) when changing from the default model setup to the improved model with cropland tree cover included((improved-default) * 100/default)

Figure 4.10 August monthly averaged change in parameters with a strong impact on rice yield with identical driving meteorology and boundary conditions after increasing Agroforestry cover in the North West IGP From default to 10% (A-D) and from 10% (present) to 50% (E-H). (A) Change in the 7-hour average (9 am to 4 pm) ozone mixing ratio (ΔM7) (10% Agroforestry – default tree cover). (B) Change in peak daytime temperature (10% Agroforestry – default tree cover). (C) Difference in relative yield loss (RYL) (10% Agroforestry – default tree cover) calculated using the ozone crop yield loss relationship of Indian rice cultivars (37). (D) Difference in relative yield loss (RYL) (10% Agroforestry – default tree cover) calculated using the temperature induced grain sterility function by Weerakoon et al. 2008 (38). (E) Change in the 7-hour average (9 am to 4 pm) ozone mixing ratio (ΔM7) (50% Agroforestry – 10% Agroforestry). (F) Change in peak daytime temperature (50% Agroforestry – 10% Agroforestry). (G) Difference in relative yield loss (RYL) (50% Agroforestry – 10% Agroforestry) calculated using the ozone crop yield loss relationship of Indian rice cultivars 37). (D) Difference in relative yield loss (RYL) (50% Agroforestry – 10% Agroforestry) calculated using the temperature induced grain sterility function by Weerakoon *et al.* 2008.

List of Tables

List of Abbreviations

A_{fire}- Area of Burning

A_{old}- Relative emission activity for old foliage

A_{new}-Relative emission activity for new foliage

A_m-Total mass of particular fuel used for a particular task

BVOCs-Biogenic Volatile Organic Compounds

C-Species concentration

CCL –Cloud Convective Layer

CFCs- chlorofluorocarbon

CFL- Courant-Fredrichs-Lewy Condition

CrIS- borne Cross-track Infrared Sounder

CVF-Continuous vegetative field

DMAPP- Dimethylallyl phosphate

DOY-Julian day of the year

$DUST_{emiss}$- Dust uplifting emission

EDGAR-The emission database for global atmospheric Research

EKMA- Empirical Kinematic Modelling Approach

EF^i_{veg}- Emission factor for biomass burning

E_{opt}- Optimum emission

F-Dry deposition flux

FINN-Fire inventory

FNL-Final Analysis data

F_{new}-New foliage fraction

F_{old}- Old foliage fraction

F_{gro}- Growing foliage fraction

F_{mat}- Matured Foliage fraction

GDAL-Geospatial data abstraction library

GFS- Global forecast system

GOCART-Global Ozone Chemistry Aerosol Radiation and Transport

GRIB- Gridded binary data

IEPOX- Isoprene epoxy diol

IGBP- International Geosphere-Biosphere Programme

IpS- Isoprene synthesase enzyme

LULC- Land use land cover

MACR- methacrolein

MEGAN- Model of Emissions of Gases and Aerosol from Nature

MEP- Mevalonate metabolic pathway

MODIS- Moderate Resolution Imaging Spectroradiometer

MOZART-Model for ozone and related chemical tracers

MVK- Methyl vinyl ketone

NCEP- National Centre for Environment prediction

N.W IGP-north-west Indo-Gangetic Plains

ODE-Ordinary Differential equation

PAN- Peroxyacetyl nitrate

PBL – Planetary Boundary Layer

PBLH – Planetary Boundary Layer Height

PCEEA- Parametrized canopy environment emission activity

PDE-Partial differential equation

PFTs- Plant functional types

PPFD-Photosynthetic photon flux density

PTR QMS- Proton transfer reaction quadrupole mass spectrometer

P_{daily}- Daily averaged PPFD

P_{TOA}- PPFD at top of atmosphere

P_{ac}- PPFD at top of canopy

R_{cut}- Cuticle resistance

R_{sm}-Stomata-Mesophyll resistance

R_{gnd}-Ground resistance

R_{inc}- Canopy resistance

r-Correlation Coefficient

RH- Relative humidity

Rho- Normalized ratio for production and loss in plant canopy

Rho_phy- Air Density

RK-Runge Kutta

S-Sensitivity

S_{WRF}- Dimensional tuning factor

SOA- Secondary Organic Aerosol

SRAD-short-wave solar radiation flux in MEGAN Climatology

T_{opt}- Optimum temperature used by MEGAN

T_{daily}- Daily average temperature used by MEGAN

T_{240}-240 Hour average temperature used by MEGAN

T_{24}- 24 Hour average temperature used by MEGAN

T_{hr}- Hourly averaged temperature used by MEGAN

U_{10}-wind velocity at 10m

U_{thres}-Threshold friction velocity

VOCs- Volatile Organic Compounds

VEGFRA- Vegetation fraction

V_d- Deposition velocity

WPS- WRF pre-processing system

WRF- Weather research and forecasting model

WRF-Chem- Weather research and forecasting coupled with chemistry model

Bibliography

Abbe, C., The physical basis of long-range weather forecsts, Mon. Wea. Rev., 29, 551–561 1901:, https://doi.org/10.1175/1520493(1901)29[551c]

Ahmadov R. Chemical mehanisms and KPP. WRF-Chem tutorial. Ncar Technical Note 2012.

Akagi SK, Yokelson RJ, Wiedinmyer C, Alvarado MJ, Reid JS, Karl T, et al. Emission factors for open and domestic biomass burning for use in atmospheric models. Atmos. Chem. Phys. 2011; 11: 4039-4072.

Andreae MO. Emission of trace gases and aerosols from biomass burning – an updated assessment. Atmos. Chem. Phys. 2019; 19: 8523-8546.

Andreae MO, Crutzen PJ. Atmospheric Aerosols: Biogeochemical Sources and Role in Atmospheric Chemistry. Science 1997; 276: 1052-1058.

Andreae MO, Merlet P. Emission of trace gases and aerosols from biomass burning. Global Biogeochem. Cycles 2001; 15: 955-966.

Arino O, Ramos Perez JJ, Kalogirou V, Bontemps S, Defourny P, Van Bogaert E. Global Land Cover Map for 2009 (GlobCover 2009). © European Space Agency (ESA) & Université catholique de Louvain (UCL), PANGAEA; 2012; https://doi.org/10.1594/PANGAEA.787668

Ashrit R, Mohandas S. Mesoscale model forecast verification during monsoon 2008. Journal of Earth System Science 2010; 119: 417-446.

Atkinson R, Arey J. Atmospheric Degradation of Volatile Organic Compounds. Chemical Reviews 2003; 103: 4605-4638.

Atkinson R, Aschmann SM, Tuazon EC, Arey J, Zielinska B. Formation of 3-Methylfuran from the gas-phase reaction of OH radicals with isoprene and the rate constant for its reaction with the OH radical. International Journal of Chemical Kinetics 1989; 21: 593-604.

Atkinson R, Baulch DL, Cox RA, Crowley JN, Hampson RF, Hynes RG, et al. Evaluated kinetic and photochemical data for atmospheric chemistry: Volume II - gas phase reactions of organic species. Atmos. Chem. Phys. 2006; 6: 3625-4055.

Baghi R, Helmig D, Guenther A, Duhl T, Daly R. Contribution of flowering trees to urban atmospheric biogenic volatile organic compound emissions. Biogeosciences Discussions 2012; 9.

Bamberger I, Ruehr NK, Schmitt M, Gast A, Wohlfahrt G, Arneth A. Isoprene emission and photosynthesis during heatwaves and drought in black locust. Biogeosciences 2017; 14: 3649-3667.

Bannister ME, Nair PKR. Agroforestry adoption in Haiti: the importance of household and farm characteristics. Agroforestry Systems 2003; 57: 149-157.

Barkley MP, Smedt ID, Van Roozendael M, Kurosu TP, Chance K, Arneth A, et al. Top-down isoprene emissions over tropical South America inferred from SCIAMACHY and OMI formaldehyde columns. Journal of Geophysical Research: Atmospheres 2013; 118: 6849-6868.

Bastin J-F, Finegold Y, Garcia C, Mollicone D, Rezende M, Routh D, Zohner CM, Crowther TW. The global tree restoration potential. Science 2019; 365: 76-79.

Bates TS, Lamb BK, Guenther A, Dignon J, Stoiber RE. Sulfur emissions to the atmosphere from natural sourees. Journal of Atmospheric Chemistry 1992; 14: 315-337.

Battisti DS, Naylor RL. Historical Warnings of Future Food Insecurity with Unprecedented Seasonal Heat. Science 2009; 323: 240-244.

Blake RS, Monks PS, Ellis AM. Proton-Transfer Reaction Mass Spectrometry. Chemical Reviews 2009; 109: 861-896.

Benefits of trees. Nature Climate Change 2019; 9: 569-569.

Bey A, Sánchez-Paus Díaz A, Maniatis D, Marchi G, Mollicone D, Ricci S, Bastin J-F, Moore R, Federici S, Rezende M, Patriarca C, Turia R, Gamoga G, Abe H, Kaidong E, Miceli G. Collect Earth: Land Use and Land Cover Assessment through Augmented Visual Interpretation. Remote Sensing 2016; 8: 807.

Bond TC, Streets DG, Yarber KF, Nelson SM, Woo J-H, Klimont Z. A technology-based global inventory of black and organic carbon emissions from combustion. J. Geophys. Res. 2004; 109: D14203.

Brovkin V, Raddatz T, Reick CH, Claussen M, Gayler V. Global biogeophysical interactions between forest and climate. Geophysical Research Letters 2009; L07405, doi:10.1029/2009GL03754.

Buzcu Guven B, Olaguer EP. Ambient formaldehyde source attribution in Houston during TexAQS II and TRAMP. Atmospheric Environment 2011; 45: 4272-4280.

Campi P, Palumbo A, Mastrorilli M. Effects of tree windbreak on microclimate and wheat productivity in a Mediterranean environment. European Journal of Agronomy 2009; 30: 220-227.

Carter CA, Cui X, Ding A, Ghanem D, Jiang F, Yi F, Zhong F. Stage-specific, Nonlinear Surface Ozone Damage to Rice Production in China. Scientific Reports 2017; 7: 44224, doi:10.1038/srep44224.

Carter WPL. Development of Ozone Reactivity Scales for Volatile Organic Compounds. Air & Waste 1994; 44: 881-899.

Carter WPL, Atkinson R. Development and evaluation of a detailed mechanism for the atmospheric reactions of isoprene and NOx. International Journal of Chemical Kinetics 1996; 28: 497-530.

Carlton AG, Wiedinmyer C, Kroll JH. A review of Secondary Organic Aerosol (SOA) formation from isoprene. Atmos. Chem. Phys. 2009; 9: 4987-5005.

Chaliyakunnel S, Millet DB, Chen X. Constraining Emissions of Volatile Organic Compounds Over the Indian Subcontinent Using Space-Based Formaldehyde Measurements. Journal of Geophysical Research: Atmospheres 2019; 124: 10525-10545.

Chameides W, Lindsay R, Richardson J, Kiang C. The role of biogenic hydrocarbons in urban photochemical smog: Atlanta as a case study. Science 1988; 241: 1473-1475.

Chandra BP, Sinha V. Contribution of post-harvest agricultural paddy residue fires in the N.W. Indo-Gangetic Plain to ambient carcinogenic benzenoids, toxic isocyanic acid and carbon monoxide. Environment International 2016; 88: 187-197.

Chauhan SK, Sharma R, Dhillon WS. Status of Intercropping in Poplar Based Agroforestry in India. Forest Bulletin 2012; 12(1):49-66.

Chavan S, Dhyani S, Handa AK, Newaj R, Rajarajan K. National Agroforestry Policy in India: A low hanging fruit. Current science 2015; 108 (10): 1826-1834.

Chen F, Dudhia J. Coupling an Advanced Land Surface–Hydrology Model with the Penn State–NCAR MM5 Modeling System. Part II: Preliminary Model Validation. Monthly Weather Review 2001; 129: 587-604.

Chen WH, Guenther AB, Wang XM, Chen YH, Gu DS, Chang M, Zhou SZ, Wu LL, Zhang YQ. Regional to Global Biogenic Isoprene Emission Responses to Changes in Vegetation From 2000 to 2015. Journal of Geophysical Research: Atmospheres 2018; 123: 3757-3771.

Cherchi A, Fogli PG, Lovato T, Peano D, Iovino D, Gualdi S, Masina S, Scoccimarro E, Materia S, Bellucci A, Navarra A. Global Mean Climate and Main Patterns of Variability in the CMCC-CM2 Coupled Model. Journal of Advances in Modeling Earth Systems 2019; 11: 185-209.

Chin M, Ginoux P, Kinne S, Torres O, Holben BN, Duncan BN, et al. Tropospheric Aerosol Optical Thickness from the GOCART Model and Comparisons with Satellite and Sun Photometer Measurements. Journal of the Atmospheric Sciences 2002; 59: 461-483.

Christian TJ, Kleiss B, Yokelson RJ, Holzinger R, Crutzen PJ, Hao WM, et al. Comprehensive laboratory measurements of biomass-burning emissions: 2. First intercomparison of open-path FTIR, PTR-MS, and GC-MS/FID/ECD. J. Geophys. Res. 2004; 109: D02311.

Churkina G, Organschi A, Reyer CPO, Ruff A, Vinke K, Liu Z, Reck BK, Graedel TE, Schellnhuber HJ. Buildings as a global carbon sink. Nature Sustainability 2020; 3: 269-276.

Claeys M, Graham B, Vas G, Wang W, Vermeylen R, Pashynska V, et al. Formation of Secondary Organic Aerosols Through Photooxidation of Isoprene. Science 2004; 303: 1173-1176.

Courant* R, Friedrichs" K, Lewyt H. On the Partial Difference Equations of Mathematical Physics. n Mathematische Annalen 100, 32-74 (1928) 1928.

Cox PM, Betts RA, Jones CD, Spall SA, Totterdell. IJ. Modelling Vegetation and the Carbon Cycle as Interactive Elements of the Climate System, Hadley Centre technical note 23, 2001.

Crippa M, Guizzardi D, Muntean M, Schaaf E, Dentener F, van Aardenne JA, et al. Gridded emissions of air pollutants for the period 1970–2012 within EDGAR v4.3.2. Earth Syst. Sci. Data 2018; 10: 1987-2013.

Crowther TW, Glick HB, Covey KR, Bettigole C, Maynard DS, Thomas SM, Smith JR, Hintler G, Duguid MC, Amatulli G, Tuanmu MN, Jetz W, Salas C, Stam C, Piotto D, Tavani R, Green S, Bruce G, Williams SJ, Wiser SK, Huber MO, Hengeveld GM, Nabuurs GJ, Tikhonova E, Borchardt P, Li CF, Powrie LW, Fischer M, Hemp A, Homeier J, Cho P, Vibrans AC, Umunay PM, Piao SL, Rowe CW, Ashton MS, Crane PR, Bradford MA. Mapping tree density at a global scale. Nature 2015; 525: 201-205.

Cui L, Zhang Z, Huang Y, Lee SC, Blake DR, Ho KF, et al. Measuring OVOCs and VOCs by PTR-MS in an urban roadside microenvironment of Hong Kong: relative humidity and temperature dependence, and field intercomparisons. Atmos. Meas. Tech. 2016; 9: 5763-5779.

Current D, Lutz E, Scherr SJ. The Costs and benefits of Agroforestry to farmers. The World Bank Research Observer 1995; 10: 151-180.

C3S: ERA5: Fifth generation of ECMWF atmospheric reanalyses of the global climate, 2017.

Czoschke N, Jang M, Kamens R. Effect of acidic seed on biogenic secondary organic aerosol growth. Atmospheric Environment 2003; 37: 4287-4299.

Dai Y, Dickinson RE, Wang Y-P. A Two-Big-Leaf Model for Canopy Temperature, Photosynthesis, and Stomatal Conductance. Journal of Climate 2004; 17: 2281-2299.

Damian V, Sandu A, Damian M, Potra F, Carmichael GR. The kinetic preprocessor KPP-a software environment for solving chemical kinetics. Computers & Chemical Engineering 2002; 26: 1567-1579.

Dani K, Jamie I, Prentice I, Atwell B. Evolution of isoprene emission capacity in plants. Trends in plant science 2014; 19.

Das S, Ashrit R, Iyengar G, Mohandas S, Gupta M, George J, et al. Skills of different mesoscale models over Indian region during monsoon season: Forecast errors. Journal of Earth System Science 2008; 117: 603-620.

de Gouw J, Warneke C. Measurements of volatile organic compounds in the earth's atmosphere using proton-transfer-reaction mass spectrometry. Mass Spectrometry Reviews 2007; 26: 223-257.

De Kauwe MG, Kala J, Lin YS, Pitman AJ, Medlyn BE, Duursma RA, Abramowitz G, Wang YP, Miralles DG. A test of an optimal stomatal conductance scheme within the CABLE land surface model. Geosci. Model Dev. 2015; 8: 431-452.

Delworth TL, Broccoli AJ, Rosati A, Stouffer RJ, Balaji V, Beesley JA, Cooke WF, Dixon KW, Dunne J, Dunne KA, Durachta JW, Findell KL, Ginoux P, Gnanadesikan A, Gordon CT, Griffies SM, Gudgel R, Harrison MJ, Held IM, Hemler RS, Horowitz LW, Klein SA, Knutson TR, Kushner PJ, Langenhorst AR, Lee H-C, Lin S-J, Lu J, Malyshev SL, Milly PCD, Ramaswamy V, Russell J, Schwarzkopf MD, Shevliakova E, Sirutis JJ, Spelman MJ, Stern WF, Winton M, Wittenberg AT, Wyman B, Zeng F, Zhang R. GFDL's CM2 Global Coupled Climate Models. Part I: Formulation and Simulation Characteristics. Journal of Climate 2006; 19: 643-674.

Deutsch CA, Tewksbury JJ, Tigchelaar M, Battisti DS, Merrill SC, Huey RB, Naylor RL. Increase in crop losses to insect pests in a warming climate. Science 2018; 361: 916-919.

Dimiceli C, Carroll M, Sohlberg R, Kim DH, Kelly M, Townshend. MOD44B MODIS/Terra Vegetation Continuous Fields Yearly L3 Global 250m SIN Grid V006 Data Set J.R.G. 2015. Archived by National Aeronautics and Space Administration, U.S. Government, LP DAAC. https://doi.org/10.5067/MODIS/MOD44B.006. Accessed 2019-06-09

Dickinson RE, Shaikh M, Bryant R, Graumlich L. Interactive Canopies for a Climate Model. Journal of Climate 1998; 11: 2823-2836.

DiGangi J, Boyle E, Karl T, Harley P, Turnipseed A, Kim S, et al. First direct measurements of formaldehyde flux via eddy covariance: implications for missing in-canopy formaldehyde sources. Atmospheric Chemistry and Physics 2011; 11.

Dudareva N, Klempien A, Muhlemann JK, Kaplan I. Biosynthesis, function and metabolic engineering of plant volatile organic compounds. New Phytologist 2013; 198: 16-32.

Dunne JP, Stouffer RJ, John JG. Reductions in labour capacity from heat stress under climate warming. Nature Climate Change 2013; 3: 563-566.

ECMWF. Copernicus Climate Change Service (C3S) (2017): "ERA5: Fifth generation of ECMWF atmospheric reanalyses of the global climate". Copernicus Climate Change Service Climate Data Store (CDS) Date of access November 2019 Data Access: December 2020.

Eerdekens G, Ganzeveld L, Vilà-Guerau de Arellano J, Klüpfel T, Sinha V, Yassaa N, et al. Flux estimates of isoprene, methanol and acetone from airborne PTR-MS measurements over the tropical rainforest during the GABRIEL 2005 campaign. Atmos. Chem. Phys. 2009; 9: 4207-4227.

Emmons LK, Walters S, Hess PG, Lamarque JF, Pfister GG, Fillmore D, Granier C, Guenther A, Kinnison D, Laepple T, Orlando J, Tie X, Tyndall G, Wiedinmyer C, Baughcum SL, Kloster S. Description and evaluation of the Model for Ozone and Related chemical Tracers, version 4 (MOZART-4). Geosci. Model Dev. 2010; 3: 43-67.

Erisman JW, Van Pul A, Wyers P. Parametrization of surface resistance for the quantification of atmospheric deposition of acidifying pollutants and ozone. Atmospheric Environment 1994; 28: 2595-2607.

Fall R. Abundant Oxygenates in the Atmosphere: A Biochemical Perspective. Chemical Reviews 2003; 103: 4941-4952.

Fast JD, Gustafson Jr. WI, Easter RC, Zaveri RA, Barnard JC, Chapman EG, et al. Evolution of ozone, particulates, and aerosol direct radiative forcing in the vicinity of Houston using a fully coupled meteorology-chemistry-aerosol model. Journal of Geophysical Research: Atmospheres 2006; 111.

Finlayson-Pitts BJ, Pitts JN. Tropospheric Air Pollution: Ozone, Airborne Toxics, Polycyclic Aromatic Hydrocarbons, and Particles. Science 1997; 276: 1045-1051.

Fischer EV, Jacob DJ, Yantosca RM, Sulprizio MP, Millet DB, Mao J, et al. Atmospheric peroxyacetyl nitrate (PAN): a global budget and source attribution. Atmos. Chem. Phys. 2014; 14: 2679-2698.

Flato G, Marotzke J, Abiodun B, Braconnot P, Chou SC, Collins W, Cox P, Driouech F, Emori S, Eyring V, Forest C, Gleckler P, Guilyardi E, Jakob C, Kattsov V, Reason C, Rummukainen M. Evaluation of Climate Models. In: Climate Change 2013: The Physical Science Basis. Contribution of Working Group I to the Fifth Assessment Report of the Intergovernmental Panel on Climate Change [Stocker, T.F., D. Qin, G.-K. Plattner, M. Tignor, S.K. Allen, J. Boschung, A. Nauels, Y. Xia, V. Bex and P.M. Midgley (eds.)]. Cambridge University Press, Cambridge, United Kingdom and New York, NY, USA. Climate Change 2013: The Physical Science Basis. Contribution of Working Group I to the Fifth Assessment Report of the Intergovernmental Panel on Climate Change. Cambridge University Press, 2013.

Foken T. 50 Years of the Monin–Obukhov Similarity Theory. Boundary-Layer Meteorology 2006; 119: 431-447.

India State of Forest Report 2019, Volume –II, Forest Survey of India Ministry of Environment, Forest & Climate Change Government of India , https://fsi.nic.in/isfr2019/isfr-fsi-vol2.pdf

Fortems-Cheiney A, Chevallier F, Pison I, Bousquet P, Saunois M, Szopa S, et al. The formaldehyde budget as seen by a global-scale multi-constraint and multi-species inversion system. Atmos. Chem. Phys. 2012; 12: 6699-6721.

Franklin J. Plant Growth Chamber Handbook. (Iowa Agriculture and Home Economics Experiment Station Special Report No. 99 (SR-99) and North Central Regional Research Publication No. 340.). Ed. by R. W. LANGHANS and T. W. TIBBITS. 21×27·5 cm. Pp.

viii+240 with 20 tables and 45 text-figures. Ames, IA, USA: Iowa State University, 1997. Price p/b: $15.00, ISBN 0361 199X. New Phytologist 1998; 138: 743-750.

Friedl MA, Strahler AH, Hodges J. Hall, G.J. Collatz, B.W. Meeson, S.O. Los, E.Brown De Colstoun, and D.R. Landis. 2010. ISLSCP II MODIS (Collection 4) IGBP Land Cover, 2000-2001. ORNL DAAC, Oak Ridge, Tennessee, USA. https://doi.org/10.3334/ORNLDAAC/968

Fu D, Millet DB, Wells KC, Payne VH, Yu S, Guenther A, et al. Direct retrieval of isoprene from satellite-based infrared measurements. Nature Communications 2019; 10: 3811.

Fuentes JD, Gu L, Lerdau M, Atkinson R, Baldocchi D, Bottenheim JW, et al. Biogenic Hydrocarbons in the Atmospheric Boundary Layer: A Review. Bulletin of the American Meteorological Society 2000; 81: 1537-1575.

GDAL/OGR contributors (2020). GDAL/OGR Geospatial Data Abstraction software Library. Open Source Geospatial Fundation. URL https://gdal.org. Accessed 2019-06-09

Ghude SD, Pfister GG, Jena C, van der A RJ, Emmons LK, Kumar R. Satellite constraints of nitrogen oxide (NOx) emissions from India based on OMI observations and WRF-Chem simulations. Geophysical Research Letters 2013; 40: 423-428.

Ghude SD, Bhat GS, Prabhakaran T, Jenamani RK, Chate DM, Safai PD, Karipot AK, Konwar M, Pithani P, Sinha V, Rao PSP, Dixit SA, Tiwari S, Todekar K, Varpe S, Srivastava AK, Bisht DS, Murugave P, Ali K, Mina U. Winter fog experiment over the Indo-Gangetic plains of India. Current Science 2017; 112: 767-784.

Giglio L, Descloitres J, Justice CO, Kaufman YJ. An Enhanced Contextual Fire Detection Algorithm for MODIS. Remote Sensing of Environment 2003; 87: 273-282.

Ginoux P, Chin M, Tegen I, Prospero JM, Holben B, Dubovik O, et al. Sources and distributions of dust aerosols simulated with the GOCART model. Journal of Geophysical Research: Atmospheres 2001; 106: 20255-20273.

Giorgetta MA, Jungclaus J, Reick CH, Legutke S, Bader J, Böttinger M, Brovkin V, Crueger T, Esch M, Fieg K, Glushak K, Gayler V, Haak H, Hollweg H-D, Ilyina T, Kinne S, Kornblueh L, Matei D, Mauritsen T, Mikolajewicz U, Mueller W, Notz D, Pithan F, Raddatz T, Rast S, Redler R, Roeckner E, Schmidt H, Schnur R, Segschneider J, Six KD, Stockhause M, Timmreck C, Wegner J, Widmann H, Wieners K-H, Claussen M, Marotzke J, Stevens B. Climate and carbon cycle changes from 1850 to 2100 in MPI-ESM simulations for the Coupled Model Intercomparison Project phase 5. Journal of Advances in Modeling Earth Systems 2013; 5: 572-597.

Goldstein AH, Galbally IE. Known and Unexplored Organic Constituents in the Earth's Atmosphere. Environmental Science & Technology 2007; 41: 1514-1521.

Golfam, P., Ashofteh, P. & Loáiciga, H.A. Evaluation of the VIKOR and FOWA Multi-Criteria Decision Making Methods for Climate-Change Adaptation of Agricultural Water Supply. Water Resour Manage 33, 2867–2884 (2019).

Goll DS, Winkler AJ, Raddatz T, Dong N, Prentice IC, Ciais P, Brovkin V. Carbon–nitrogen interactions in idealized simulations with JSBACH (version 3.10). Geosci. Model Dev. 2017; 10: 2009-2030.

Grell GA, Dévényi D. A generalized approach to parameterizing convection combining ensemble and data assimilation techniques. Geophysical Research Letters 2002; 29: 38-1-38-4.

Grell GA, Peckham SE, Schmitz R, McKeen SA, Frost G, Skamarock WC, et al. Fully coupled "online" chemistry within the WRF model. Atmospheric Environment 2005; 39: 6957-6975.

Guenther A, Baugh W, Davis K, Hampton G, Harley P, Klinger L, et al. Isoprene fluxes measured by enclosure, relaxed eddy accumulation, surface layer gradient, mixed layer gradient, and mixed layer mass balance techniques. Journal of Geophysical Research: Atmospheres 1996; 101: 18555-18567.

Guenther A, Hewitt CN, Erickson D, Fall R, Geron C, Graedel T, et al. A global model of natural volatile organic compound emissions. Journal of Geophysical Research: Atmospheres 1995; 100: 8873-8892.

Guenther A, Karl T, Harley P, Wiedinmyer C, Palmer PI, Geron C. Estimates of global terrestrial isoprene emissions using MEGAN (Model of Emissions of Gases and Aerosols from Nature). Atmos. Chem. Phys. 2006; 6: 3181-3210.

Guenther AB, Jiang X, Heald CL, Sakulyanontvittaya T, Duhl T, Emmons LK, et al. The Model of Emissions of Gases and Aerosols from Nature version 2.1 (MEGAN2.1): an extended and updated framework for modeling biogenic emissions. Geosci. Model Dev. 2012; 5: 1471-1492.

Guenther AB, Monson RK, Fall R. Isoprene and monoterpene emission rate variability: Observations with eucalyptus and emission rate algorithm development. Journal of Geophysical Research: Atmospheres 1991; 96: 10799-10808.

Guenther AB, Zimmerman PR, Harley PC, Monson RK, Fall R. Isoprene and monoterpene emission rate variability: Model evaluations and sensitivity analyses. Journal of Geophysical Research: Atmospheres 1993; 98: 12609-12617.

Haagen-Smit AJ. Chemistry and Physiology of Los Angeles Smog. Industrial & Engineering Chemistry 1952; 44: 1342-1346.

Hakkim H, Sinha V, Chandra BP, Kumar A, Mishra AK, Sinha B, et al. Volatile organic compound measurements point to fog-induced biomass burning feedback to air quality in the megacity of Delhi. Science of The Total Environment 2019; 689: 295-304.

Hansen MC, Defries RS, Townshend JRG, Sohlberg R. Global land cover classification at 1 km spatial resolution using a classification tree approach. International Journal of Remote Sensing 2000; 21: 1331-1364.

Harley PC, Litvak ME, Sharkey TD, Monson RK. Isoprene Emission from Velvet Bean Leaves (Interactions among Nitrogen Availability, Growth Photon Flux Density, and Leaf Development). Plant Physiology 1994; 105: 279-285.

Hathaway MD. Agroecology and permaculture: addressing key ecological problems by rethinking and redesigning agricultural systems. Journal of Environmental Studies and Sciences 2016; 6: 239-250.

Heald CL, Wilkinson MJ, Monson RK, Alo CA, Wang G, Guenther A. Response of isoprene emission to ambient CO2 changes and implications for global budgets. Global Change Biology 2009; 15: 1127-1140

Hewitt CN, Ashworth K, Boynard A, Guenther A, Langford B, MacKenzie AR, et al. Ground

level ozone influenced by circadian control of isoprene emissions. Nature Geosci 2011; 4: 671-674.

He C, Murray F, Lyons T. Monoterpene and isoprene emissions from 15 Eucalyptus species in Australia - The Study of Uncertainties in Physical Measurements. Atmospheric Environment 2000; 34(4): 645-655.

Hersbach H, Bell B, Berrisford P, Hirahara S, Horányi A, Muñoz-Sabater J, Nicolas J, Peubey C, Radu R, Schepers D, Simmons A, Soci C, Abdalla S, Abellan X, Balsamo G, Bechtold P, Biavati G, Bidlot J, Bonavita M, De Chiara G, Dahlgren P, Dee D, Diamantakis M, Dragani R, Flemming J, Forbes R, Fuentes M, Geer A, Haimberger L, Healy S, Hogan RJ, Hólm E, Janisková M, Keeley S, Laloyaux P, Lopez P, Lupu C, Radnoti G, de Rosnay P, Rozum I, Vamborg F, Villaume S, Thépaut J-N. The ERA5 Global Reanalysis. Quarterly Journal of the Royal Meteorological Society 2020; doi: 10.1002/qj.3803

Holdsworth AM, Rees T, Monahan AH. Parameterization Sensitivity and Instability Characteristics of the Maximum Sustainable Heat Flux Framework for Predicting Turbulent Collapse. Journal of the Atmospheric Sciences 2016; 73: 3527-3540.

Holzinger R, Warneke C, Hansel A, Jordan A, Lindinger W, Scharffe DH, et al. Biomass burning as a source of formaldehyde, acetaldehyde, methanol, acetone, acetonitrile, and hydrogen cyanide. Geophys. Res. Lett. 1999; 26: 1161-1164.

Hong S-Y, Noh Y, Dudhia J. A New Vertical Diffusion Package with an Explicit Treatment of Entrainment Processes. Monthly Weather Review 2006; 134: 2318-2341.

Hu X-M, Nielsen-Gammon JW, Zhang F. Evaluation of Three Planetary Boundary Layer Schemes in the WRF Model. Journal of Applied Meteorology and Climatology 2010; 49: 1831-1844.

Jain SK, Singh P. Economic analysis of industrial Agroforestry: poplar (Populus deltoides) in Uttar Pradesh (India). Agroforestry Systems 2000; 49: 255-273.

Ito A, Penner JE. Global estimates of biomass burning emissions based on satellite imagery for the year 2000. Journal of Geophysical Research: Atmospheres 2004; 109.

Jacob DJ, Field BD, Jin EM, Bey I, Li Q, Logan JA, et al. Atmospheric budget of acetone. Journal of Geophysical Research: Atmospheres 2002; 107: ACH 5-1-ACH 5-17.

Janjic ZI. The surface layer in the NCEP Eta Model," American Meteorological Society 1996; Proceedings of the 11th Conference on Numerical Weather Prediction: 354–355.

Janjić ZI. The Step-Mountain Eta Coordinate Model: Further Developments of the Convection, Viscous Sublayer, and Turbulence Closure Schemes. Monthly Weather Review 1994; 122: 927-945.

Janssens-Maenhout G, Crippa M, Guizzardi D, Dentener F, Muntean M, Pouliot G, et al. HTAP_v2.2: a mosaic of regional and global emission grid maps for 2008 and 2010 to study hemispheric transport of air pollution. Atmos. Chem. Phys. 2015; 15: 11411-11432.

Jardine K, Karl T, Lerdau M, Harley P, Guenther A, Mak JE. Carbon isotope analysis of acetaldehyde emitted from leaves following mechanical stress and anoxia. Plant Biology 2009; 11: 591-597.

Jeffries H, Kamens R, Sexton K. Early history and rationale for outdoor chamber work at the University of North Carolina. Environmental Chemistry 2013; 10: 349.

Jones CE, Hopkins JR, Lewis AC. In situ measurements of isoprene and monoterpenes within a south-east Asian tropical rainforest. Atmos. Chem. Phys. 2011; 11: 6971-6984.

Kalogridis C, Gros V, Sarda-Esteve R, Langford B, Loubet B, Bonsang B, et al. Concentrations and fluxes of isoprene and oxygenated VOCs at a French Mediterranean oak forest. Atmos. Chem. Phys. 2014; 14: 10085-10102.

Karl T, Guenther A, Turnipseed A, Tyndall G, Artaxo P, Martin S. Rapid formation of isoprene photo-oxidation products observed in Amazonia. Atmos. Chem. Phys. 2009; 9: 7753-7767.

Karl T, Potosnak M, Guenther A, Clark D, Walker J, Herrick JD, et al. Exchange processes of volatile organic compounds above a tropical rain forest: Implications for modeling tropospheric chemistry above dense vegetation. J. Geophys. Res. 2004; 109: D18306.

Karl TG, Christian TJ, Yokelson RJ, Artaxo P, Hao WM, Guenther A. The Tropical Forest and Fire Emissions Experiment: method evaluation of volatile organic compound emissions measured by PTR-MS, FTIR, and GC from tropical biomass burning. Atmos. Chem. Phys. 2007; 7: 5883-5897.

Kaufman YJ, Justice CO, Flynn LP, Kendall JD, Prins EM, Giglio L, et al. Potential global fire monitoring from EOS-MODIS. Journal of Geophysical Research: Atmospheres 1998; 103: 32215-32238.

Ke Y, Leung LR, Huang M, Coleman AM, Li H, Wigmosta MS. Development of high resolution land surface parameters for the Community Land Model. Geosci. Model Dev. 2012; 5: 1341-1362.

Kesselmeier J. Exchange of Short-Chain Oxygenated Volatile Organic Compounds (VOCs) between Plants and the Atmosphere: A Compilation of Field and Laboratory Studies. Journal of Atmospheric Chemistry, v.39, 219-233 (2001) 2001; 39.

Kesselmeier J, Staudt M. Biogenic Volatile Organic Compounds (VOC): An Overview on Emission, Physiology and Ecology. Journal of Atmospheric Chemistry 1999; 33: 23-88.

Khan A, Whelan M, Rhew R. Effects of temperature and soil moisture on methyl halide and chloroform fluxes from drained peatland pasture soils. Journal of environmental monitoring : JEM 2011; 14: 241-9.

Kinnee E, Geron C, Pierce T. United States land use inventory for estimating biogenic ozone precursor emissions. Ecological Applications 1997; 7: 46-58.

Kirstine W, Galbally I, Ye Y, Hooper M. Emissions of volatile organic compounds (primarily oxygenated species) from pasture. Journal of Geophysical Research: Atmospheres 1998; 103: 10605-10619.

Klemp JB, Skamarock WC, Dudhia J. Conservative Split-Explicit Time Integration Methods for the Compressible Nonhydrostatic Equations. Monthly Weather Review 2007; 135: 2897-2913.

Knoke T, Bendix J, Pohle P, Hamer U, Hildebrandt P, Roos K, Gerique A, Sandoval ML, Breuer L, Tischer A, Silva B, Calvas B, Aguirre N, Castro LM, Windhorst D, Weber M, Stimm B, Günter S, Palomeque X, Mora J, Mosandl R, Beck E. Afforestation or intense pasturing improve the ecological and economic value of abandoned tropical farmlands. Nature Communications 2014; 5: 5612.

Knudsen JT, Eriksson R, Gershenzon J, Ståhl B. Diversity and distribution of floral scent. The Botanical Review 2006; 72: 1.

Kohli RK, Singh HP, Batish DR. An inventory of multipurpose avenue trees of urban Chandigarh, India. In: Hansen M; Burk, T (eds.) Integrated tools for natural resources inventories in the 21st century, 2000, 697-704.

Kroll JH, Ng NL, Murphy SM, Flagan RC, Seinfeld JH. Secondary Organic Aerosol Formation from Isoprene Photooxidation. Environmental Science & Technology 2006; 40: 1869-1877.

Kuhn U, Andreae MO, Ammann C, Araújo AC, Brancaleoni E, Ciccioli P, et al. Isoprene and monoterpene fluxes from Central Amazonian rainforest inferred from tower-based and airborne measurements, and implications on the atmospheric chemistry and the local carbon budget. Atmos. Chem. Phys. 2007; 7: 2855-2879.

Kumar R, Barth MC, Madronich S, Naja M, Carmichael GR, Pfister GG, et al. Effects of dust aerosols on tropospheric chemistry during a typical pre-monsoon season dust storm in northern India. Atmos. Chem. Phys. 2014a; 14: 6813-6834.

Kumar R, Naja M, Pfister GG, Barth MC, Wiedinmyer C, and Brasseur CP. Simulations over South Asia using the Weather Research and Forecasting model with Chemistry (WRF-Chem): chemistry evaluation and initial results. Geosci. Model Dev. 2012, 5, 619–648, https://doi.org/10.5194/gmd-5-619-2012.

Kumar R, Barth MC, Pfister GG, Naja M, Brasseur GP. WRF-Chem simulations of a typical pre-monsoon dust storm in northern India: influences on aerosol optical properties and radiation budget. Atmos. Chem. Phys. 2014b; 14: 2431-2446.

Kumar V, Sarkar C, Sinha V. Influence of post-harvest crop residue fires on surface ozone mixing ratios in the N.W. IGP analyzed using 2 years of continuous in situ trace gas measurements. Journal of Geophysical Research: Atmospheres 2016a; 121: 3619-3633.

Kumar V, Sarkar C, Sinha V. Influence of post-harvest crop residue fires on surface ozone mixing ratios in the N.W. IGP analyzed using 2 years of continuous in situ trace gas measurements. Journal of Geophysical Research: Atmospheres 2016b; 121: 2015JD024308.

Kumar V, Sinha V. VOC–OHM: A new technique for rapid measurements of ambient total OH reactivity and volatile organic compounds using a single proton transfer reaction mass spectrometer. International Journal of Mass Spectrometry 2014; 374: 55-63.

Kuyah S, Whitney CW, Jonsson M, Sileshi GW, Öborn I, Muthuri CW, Luedeling E. Agroforestry delivers a win-win solution for ecosystem services in sub-Saharan Africa. A meta-analysis. Agronomy for Sustainable Development 2019; 39: 47 doi:10.1007/s13593-019-0589-8.

Lakoff G, Johnson M. The Metaphorical Structure of the Human Conceptual System. Cognitive Science 1980; 4: 195-208.

Lamb B, Pierce T, Baldocchi D, Allwine E, Dilts S, Westberg H, et al. Evaluation of forest canopy models for estimating isoprene emissions. Journal of Geophysical Research: Atmospheres 1996; 101: 22787-22797.

Langford B, Misztal PK, Nemitz E, Davison B, Helfter C, Pugh TAM, et al. Fluxes and concentrations of volatile organic compounds from a South-East Asian tropical rainforest. Atmos. Chem. Phys. 2010; 10: 8391-8412.

Laprise R. The Euler Equations of Motion with Hydrostatic Pressure as an Independent Variable. Monthly Weather Review 1992; 120: 197-207.

Lasco RD, Delfino RJP, Catacutan DC, Simelton ES, Wilson DM. Climate risk adaptation by smallholder farmers: the roles of trees and agroforestry. Current Opinion in Environmental Sustainability 2014; 6: 83-88.

Latifovic R, Zhu Z-L. Land cover mapping of North and Central America—Global Land Cover 2000. Remote Sensing of Environment 2004; 89: 116-127.

Lawrence MG, Lelieveld J. Atmospheric pollutant outflow from southern Asia: a review. Atmos. Chem. Phys. 2010; 10: 11017-11096.

Lawrence DM, Oleson KW, Flanner MG, Thornton PE, Swenson SC, Lawrence PJ, Zeng X, Yang Z-L, Levis S, Sakaguchi K, Bonan GB, Slater AG. Parameterization improvements and functional and structural advances in Version 4 of the Community Land Model. Journal of Advances in Modeling Earth Systems 2011; 3; M03001, doi: 10.1029/2011MS000045.

Lawrence PJ, Chase TN. Representing a new MODIS consistent land surface in the Community Land Model (CLM 3.0). Journal of Geophysical Research: Biogeosciences 2007; 112: G01023, doi:10.1029/2006JG000168.

Lee M, Heikes BG, Jacob DJ, Sachse G, Anderson B. Hydrogen peroxide, organic hydroperoxide, and formaldehyde as primary pollutants from biomass burning. Journal of Geophysical Research: Atmospheres 1997; 102: 1301-1309.

Lelieveld J, Gromov S, Pozzer A, Taraborrelli D. Global tropospheric hydroxyl distribution, budget and reactivity. Atmos. Chem. Phys. 2016; 16: 12477-12493.

Lelieveld J, Butler TM, Crowley JN, Dillon TJ, Fischer H, Ganzeveld L, et al. Atmospheric oxidation capacity sustained by a tropical forest. Nature 2008; 452: 737-740.

Lewis SL, Wheeler CE, Mitchard ETA, Koch A. Restoring natural forests is the best way to remove atmospheric carbon. Nature 2019; 568: 25-28.

Li W, MacBean N, Ciais P, Defourny P, Lamarche C, Bontemps S, Houghton RA, Peng S. Gross and net land cover changes in the main plant functional types derived from the annual ESA CCI land cover maps (1992–2015). Earth Syst. Sci. Data 2018; 10: 219-234.

Li Z, Ratliff EA, Sharkey TD. Effect of Temperature on Postillumination Isoprene Emission in Oak and Poplar. Plant Physiology 2011; 155: 1037-1046.

Liu YJ, Herdlinger-Blatt I, McKinney KA, Martin ST. Production of methyl vinyl ketone and methacrolein via the hydroperoxyl pathway of isoprene oxidation. Atmos. Chem. Phys. 2013; 13: 5715-5730.

Loveland TR, Reed BC, Brown JF, Ohlen DO, Zhu Z, Yang L, Merchant JW. Development of a global land cover characteristics database and IGBP DISCover from 1 km AVHRR data. International Journal of Remote Sensing 2000; 21: 1303-1330.

Macdonald RC, Fall R. Acetone emission from conifer buds. Phytochemistry 1993a; 34: 991-994.

MacDonald RC, Fall R. Detection of substantial emissions of methanol from plants to the atmosphere. Atmospheric Environment. Part A. General Topics 1993b; 27: 1709-1713.

Madronich S. Photodissociation in the atmosphere: 1. Actinic flux and the effects of ground reflections and clouds. Journal of Geophysical Research: Atmospheres 1987; 92: 9740-9752.

Mahto SS, Mishra V. Does ERA-5 Outperform Other Reanalysis Products for Hydrologic Applications in India? Journal of Geophysical Research: Atmospheres 2019; 124: 9423-9441.

Makkonen R, Asmi A, Kerminen VM, Boy M, Arneth A, Guenther A, Kulmala M. BVOC-aerosol-climate interactions in the global aerosol-climate model ECHAM5.5-HAM2. Atmos. Chem. Phys. 2012; 12: 10077-10096.

Michoud V, Hansen RF, Locoge N, Stevens PS, Dusanter S. Detailed characterizations of the new Mines Douai comparative reactivity method instrument via laboratory experiments and modeling. Atmos. Meas. Tech. 2015; 8: 3537-3553.

Monson RK, Holland EA. Biospheric trace gas fluxes and their control over tropospheric chemistry. Annual Review of Ecology and Systematics 2001; 32: 547-576.

Marticorena B, Bergametti G. Modeling the atmospheric dust cycle: 1. Design of a soil-derived dust emission scheme. Journal of Geophysical Research: Atmospheres 1995; 100: 16415-16430.

Millet DB, Guenther A, Siegel DA, Nelson NB, Singh HB, de Gouw JA, et al. Global atmospheric budget of acetaldehyde: 3-D model analysis and constraints from in-situ and satellite observations. Atmos. Chem. Phys. 2010; 10: 3405-3425.

Mills G, Pleijel H, Malley CS, Sinha B, Cooper OR, Schultz MG, Neufeld HS, Simpson D, Sharps K, Feng Z, Gerosa G, Harmens H, Kobayashi K, Saxena P, Paoletti E, Sinha V, Xu X. Tropospheric Ozone Assessment Report: Present-day tropospheric ozone distribution and trends relevant to vegetation. Elementa Science of the Anthropocene 2018, 6: 47. DOI: https://doi.org/10.1525/elementa.302.

Mishra AK, Sinha V. Emission drivers and variability of ambient isoprene, formaldehyde and acetaldehyde in north-west India during monsoon season. Environmental Pollution 2020; 267: 115538.

Mishra AK, Sinha B, Kumar R, Barth M, Hakkim H, Kumar V, et al. Cropland trees need to be included for accurate model simulations of land-atmosphere heat fluxes, temperature, boundary layer height, and ozone. Science of The Total Environment 2021; 751: 141728.

Misztal PK, Nemitz E, Langford B, Di Marco CF, Phillips GJ, Hewitt CN, et al. Direct ecosystem fluxes of volatile organic compounds from oil palms in South-East Asia. Atmos. Chem. Phys. 2011; 11: 8995-9017.

Mitchell D, Heaviside C, Schaller N, Allen M, Ebi KL, Fischer EM, Gasparrini A, Harrington L, Kharin V, Shiogama H, Sillmann J, Sippel S, Vardoulakis S. Extreme heat-related mortality avoided under Paris Agreement goals. Nature Climate Change 2018; 8: 551-553.

Mlawer EJ, Taubman SJ, Brown PD, Iacono MJ, Clough SA. Radiative transfer for inhomogeneous atmospheres: RRTM, a validated correlated-k model for the longwave. Journal of Geophysical Research: Atmospheres 1997; 102: 16663-16682.

Monson RK, Holland EA. Biospheric trace gas fluxes and their control over tropospheric chemistryY. Annual Review of Ecology and Systematics 2001; 32: 547-576.

Morrison H, Curry JA, Khvorostyanov VI. A New Double-Moment Microphysics Parameterization for Application in Cloud and Climate Models. Part I: Description. Journal of the Atmospheric Sciences 2005; 62: 1665-1677.

Nair P, Mohan Kumar B, Nair V. Agroforestry as a strategy for carbon sequestration. Journal of Plant Nutrition and Soil Science 2009; 172: 10-23.

Niinemets Ü, Tenhunen JD, Harley PC, Steinbrecher R. A model of isoprene emission based on energetic requirements for isoprene synthesis and leaf photosynthetic properties for Liquidambar and Quercus. Plant, Cell & Environment 1999; 22: 1319-1335.

Ojha N, Pozzer A, Rauthe-Schöch A, Baker AK, Yoon J, Brenninkmeijer CAM, et al. Ozone and carbon monoxide over India during the summer monsoon: regional emissions and transport. Atmos. Chem. Phys. 2016; 16: 3013-3032.

Olauson, J.: ERA5: The new champion of wind power modelling?, Renewable Energy, 126, 322-331, 10.1016/j.renene.2018.03.056, 2018.

Pallavi, Sinha B, Sinha V. Source apportionment of volatile organic compounds in the northwest Indo-Gangetic Plain using a positive matrix factorization model. Atmos. Chem. Phys. 2019; 19: 15467-15482.

Palmer PI, Abbot DS, Fu TM, Jacob DJ, Chance K, Kurosu TP, et al. Quantifying the seasonal and interannual variability of North American isoprene emissions using satellite observations of the formaldehyde column. Journal of Geophysical Research: Atmospheres 2006; 111.

Park J-H, Goldstein AH, Timkovsky J, Fares S, Weber R, Karlik J, et al. Active Atmosphere-Ecosystem Exchange of the Vast Majority of Detected Volatile Organic Compounds. Science 2013; 341: 643-647.

Park RJ, Hong SK, Kwon HA, Kim S, Guenther A, Woo JH, et al. An evaluation of ozone dry deposition simulations in East Asia. Atmos. Chem. Phys. 2014; 14: 7929-7940.

Parrish D, Ryerson T, Mellqvist J, Johansson J, Fried A, Richter D, et al. Primary and secondary sources of formaldehyde in urban atmospheres: Houston Texas region. Atmospheric Chemistry and Physics Discussions 2011; 11.

Pawar H, Garg S, Kumar V, Sachan H, Arya R, Sarkar C, et al. Quantifying the contribution of long-range transport to particulate matter (PM) mass loadings at a suburban site in the north-western Indo-Gangetic Plain (NW-IGP). Atmos. Chem. Phys. 2015; 15: 9501-9520.

Pegoraro E, Rey A, Bobich EG, Barron-Gafford G, Grieve KA, Malhi Y, et al. Effect of elevated CO2 concentration and vapour pressure deficit on isoprene emission from leaves of Populus deltoides during drought. Functional Plant Biology 2004; 31: 1137-1147.

Peng J, Dan L. The Response of the Terrestrial Carbon Cycle Simulated by FGOALS-AVIM to Rising CO2, In: Zhou T., Yu Y., Liu Y., Wang B. (eds) Flexible Global Ocean-Atmosphere-Land System Model. Springer Earth System Sciences. Springer, Berlin, Heidelberg, 2014.

Petron G, Harley P, Greenberg J, Guenther A. Seasonal temperature influence isoprene emission. Geophysical Research Letters 2001; 28: 1707-1710.

Pfister, G. G., S. Walters, L. K. Emmons, D. P. Edwards, and J. Avise. Quantifying the contribution of inflow on surface ozone over California during summer 2008, J. Geophys.Res. Atmos., 118, 12,282–12,299, doi:10.1002/2013JD020336, 2013.

Phillips NA. A coordinate system having some special advantages for Numerical Forecasting. Journal of Meteorology 1957; 14: 184-185.

Pierce T, Geron C, Bender L, Dennis R, Tonnesen G, Guenther A. Influence of increased isoprene emissions on regional ozone modeling. Journal of Geophysical Research: Atmospheres 1998; 103: 25611-25629.

Pongratz J, Reick C, Raddatz T, Claussen M. A reconstruction of global agricultural areas and land cover for the last millennium. Global Biogeochemical Cycles 2008; 22: GB3018, doi:10.1029/2007GB003153.

Poulter B, MacBean N, Hartley A, Khlystova I, Arino O, Betts R, Bontemps S, Boettcher M, Brockmann C, Defourny P, Hagemann S, Herold M, Kirches G, Lamarche C, Lederer D, Ottlé C, Peters M, Peylin P. Plant functional type classification for earth system models: results from the European Space Agency's Land Cover Climate Change Initiative. Geosci. Model Dev. 2015; 8: 2315-2328.

Pugh TAM, MacKenzie AR, Langford B, Nemitz E, Misztal PK, Hewitt CN. The influence of small-scale variations in isoprene concentrations on atmospheric chemistry over a tropical rainforest. Atmos. Chem. Phys. 2011; 11: 4121-4134.

Raju A, Parekh A, Chowdary JS, Gnanaseelan C. Assessment of the Indian summer monsoon in the WRF regional climate model. Climate Dynamics 2015; 44: 3077-3100.

Rasmussen RA. Isoprene: identified as a forest-type emission to the atmosphere. Environmental Science & Technology 1970; 4: 667-671.

Rasmussen RA. What Do the Hydrocarbons from Trees Contribute to Air Pollution? Journal of the Air Pollution Control Association 1972; 22: 537-543.

Rasulov B, Bichele I, Laisk A, Niinemets Ü. Competition between isoprene emission and pigment synthesis during leaf development in aspen. Plant, cell & environment 2014; 37: 724-741.

Reij C, Garrity D. Scaling up farmer-managed natural regeneration in Africa to restore degraded landscapes. Biotropica 2016; 48: 834-843.

Research Data Archive at the National Center for Atmospheric Research, Computational and Information Systems Laboratory. National Centers for Environmental Prediction/National Weather Service/NOAA/U.S. Department of Commerce: NCEP FNL Operational Model Global Tropospheric Analyses, continuing from July 1999, Research Data Archive at the National Center for Atmospheric Research, Computational and Information Systems Laboratory, https://doi.org/10.5065/D6M043C6, 2000: Accessed on 11/12/2017.

Rinne HJI, Guenther AB, Greenberg JP, Harley PC. Isoprene and monoterpene fluxes measured above Amazonian rainforest and their dependence on light and temperature. Atmospheric Environment 2002; 36: 2421-2426.

Rodell M, Famiglietti JS, Wiese DN, Reager JT, Beaudoing HK, Landerer FW, Lo MH. Emerging trends in global freshwater availability. Nature 2019; 557-659.

Rodell M, Velicogna I, Famiglietti JS. Satellite-based estimates of groundwater depletion in India. Nature 2009; 460: 999-1002.

Roe S, Streck C, Obersteiner M, Frank S, Griscom B, Drouet L, Fricko O, Gusti M, Harris N, Hasegawa T, Hausfather Z, Havlík P, House J, Nabuurs G-J, Popp A, Sánchez MJS, Sanderman J, Smith P, Stehfest E, Lawrence D. Contribution of the land sector to a 1.5 °C world. Nature Climate Change 2019; 9: 817-828.

Salam MA, Noguchi T, Koike M. Understanding why farmers plant trees in the homestead agroforestry in Bangladesh. Agroforestry Systems 2000; 50: 77-93.

Sanadze G. The nature of gaseous substances emitted by leaves of Robinia pseudoacacia. Soobshcheniya Akademi Nauk Gruzinskoj 1957; 27: 747–750.

Sanadze GA. Biogenic Isoprene (A Review). Russian Journal of Plant Physiology 2004; 51: 729-741.

Sander SP, Finlayson-Pitts B, Friedl RR, Golden DM, Huie R, Keller-Rudek H, et al. Chemical Kinetics and Photochemical Data for Use in Atmospheric Studies, Evaluation No. 15, 2006.

Sarkar C, Kumar V, Sinha V. Massive emissions of carcinogenic benzenoids from paddy residue burning in North India. Current Science 2013; 104: 1703-1706.

Sarkar C, Sinha V, Kumar V, Rupakheti M, Panday A, Mahata KS, et al. Overview of VOC emissions and chemistry from PTR-TOF-MS measurements during the SusKat-ABC campaign: high acetaldehyde, isoprene and isocyanic acid in wintertime air of the Kathmandu Valley. Atmos. Chem. Phys. 2016; 16: 3979-4003.

Sato H, Itoh A, Kohyama T. SEIB–DGVM: A new Dynamic Global Vegetation Model using a spatially explicit individual-based approach. Ecological Modelling 2007; 200: 279-307.

Schade GW, Goldstein AH. Seasonal measurements of acetone and methanol: Abundances and implications for atmospheric budgets. Global Biogeochemical Cycles 2006; 20.

Schnitzler J-P, Louis S, Behnke K, Loivamäki M. Poplar volatiles – biosynthesis, regulation and (eco)physiology of isoprene and stress-induced isoprenoids. Plant Biology 2010; 12: 302-316.

Schmidt GA, Kelley M, Nazarenko L, Ruedy R, Russell GL, Aleinov I, Bauer M, Bauer SE, Bhat MK, Bleck R, Canuto V, Chen Y-H, Cheng Y, Clune TL, Del Genio A, de Fainchtein R, Faluvegi G, Hansen JE, Healy RJ, Kiang NY, Koch D, Lacis AA, LeGrande AN, Lerner J, Lo KK, Matthews EE, Menon S, Miller RL, Oinas V, Oloso AO, Perlwitz JP, Puma MJ, Putman WM, Rind D, Romanou A, Sato M, Shindell DT, Sun S, Syed RA, Tausnev N, Tsigaridis K, Unger N, Voulgarakis A, Yao M-S, Zhang J. Configuration and assessment of the GISS ModelE2 contributions to the CMIP5 archive. Journal of Advances in Modeling Earth Systems 2014; 6: 141-184.

Schultz MG, Stadtler S, Schröder S, Taraborrelli D, Franco B, Krefting J, Henrot A, Ferrachat S, Lohmann U, Neubauer D, Siegenthaler-Le Drian C, Wahl S, Kokkola H, Kühn T, Rast S, Schmidt H, Stier P, Kinnison D, Tyndall GS, Orlando JJ, Wespes C. The chemistry–climate model ECHAM6.3-HAM2.3-MOZ1.0. Geosci. Model Dev. 2018; 11: 1695-1723.

Seco R, Peñuelas J, Filella I. Formaldehyde emission and uptake by Mediterranean trees Quercus ilex and Pinus halepensis. Atmospheric Environment 2008; 42: 7907-7914.

Seinfeld JH, Pandis SN. Atmospheric Chemistry and Physics: John Wiley and Sons, New York., (1998)

Sexton JO, Song X-P, Feng M, Noojipady P, Anand A, Huang C, Kim D-H, Collins KM, Channan S, DiMiceli C, Townshend JR. Global, 30-m resolution continuous fields of tree cover: Landsat-based rescaling of MODIS vegetation continuous fields with lidar-based estimates of error. International Journal of Digital Earth 2013; 6: 427-448.

Sharkey. Isoprene emission from plants. Annual Review of Plant Physiology and Plant Molecular Biology 2001; 52: 407-436.

Sharkey TD, Singsaas EL. Why plants emit isoprene. Nature 1995; 374: 769-769.

Sharkey TD, Wiberley AE, Donohue AR. Isoprene Emission from Plants: Why and How. Annals of Botany 2008; 101: 5-18.

Sharma G, Sinha B, Jangra P, Hakkim H, Chandra BP, Sharma A, et al. Gridded emissions of municipal waste burning in India. Environmental Science & Technology 2019; 53.

Silva RA, West JJ, Lamarque J-F, Shindell DT, Collins WJ, Faluvegi G, Folberth GA, Horowitz LW, Nagashima T, Naik V, Rumbold Steven T, Sudo K, Takemura T, Bergmann D, Cameron-Smith P, Doherty RM, Josse B, MacKenzie IA, Stevenson David S, Zeng G. Future global mortality from changes in air pollution attributable to climate change. Nature Climate Change 2017; 7: 647-651.

Simonaitis R, Meagher JF, Bailey EM. Evaluation of the condensed carbon bond (CB-IV) mechanism against smog chamber data at low VOC and NOx concentrations. Atmospheric Environment 1997; 31: 27-43.

Sinha B, Singh Sangwan K, Maurya Y, Kumar V, Sarkar C, Chandra BP, et al. Assessment of crop yield losses in Punjab and Haryana using 2 years of continuous in situ ozone measurements. Atmos. Chem. Phys. 2015; 15: 9555-9576.

Sinha V, Hakkim H, Kumar V. Advances in Identification and Quantification of Non-methane Volatile Organic Compounds Emitted from Biomass Fires through Laboratory Fire Experiments. Advances in atmospheric Chemistry Volume 2, :Organic Oxidation and Multiphase Chemistry, chapter 3 2019.

Sinha V, Kumar V, Sarkar C. Chemical composition of pre-monsoon air in the Indo-Gangetic Plain measured using a new air quality facility and PTR-MS: high surface ozone and strong influence of biomass burning. Atmos. Chem. Phys. 2014; 14: 5921-5941.

Sitch S, Smith B, Prentice IC, Arneth A, Bondeau A, Cramer W, Kaplan JO, Levis S, Lucht W, Sykes MT, Thonicke K, Venevsky S. Evaluation of ecosystem dynamics, plant geography and terrestrial carbon cycling in the LPJ dynamic global vegetation model. Global Change Biology 2003; 9: 161-185.

Skamarock WC, Klemp JB, Dudhia J, Gill DO, Barker DM, Duda MG, et al. A Description of the Advanced Research WRF Version 3. NCAR TECHNICAL NOTE 2008; NCAR/TN–475+STR.

Skamarock WC, Weisman ML. The Impact of Positive-Definite Moisture Transport on NWP Precipitation Forecasts. Monthly Weather Review 2009; 137: 488-494.

Song XP, Hansen MC, Stehman SV, Potapov PV, Tyukavina A, Vermote EF, Townshend JR. Global land change from 1982 to 2016. Nature 2018; 560: 639-643.

Sprengnether M, Demerjian KL, Donahue NM, Anderson JG. Product analysis of the OH oxidation of isoprene and 1,3-butadiene in the presence of NO. Journal of Geophysical Research: Atmospheres 2002; 107: ACH 8-1-ACH 8-13.

Stauffer DR, Seaman NL. Use of Four-Dimensional Data Assimilation in a Limited-Area Mesoscale Model. Part I: Experiments with Synoptic-Scale Data. Monthly Weather Review 1990; 118: 1250-1277.

Stavrakou T, Müller JF, Bauwens M, De Smedt I, Van Roozendael M, Guenther A, et al. Isoprene emissions over Asia 1979–2012: impact of climate and land-use changes. Atmos. Chem. Phys. 2014; 14: 4587-4605.

Stensrud DJ. Parameterization Schemes: Keys to Understanding Numerical Weather Prediction Models. Cambridge: Cambridge University Press, 2007.

Stockwell WR, Middleton P, Chang JS, Tang X. The second generation regional acid deposition model chemical mechanism for regional air quality modeling. Journal of Geophysical Research: Atmospheres 1990; 95: 16343-16367.

Sulzman CA, Lawrence MG. Automatic Coding of chemistry solvers in WRF-Chem using KPP 7th WRF Users Workshop, Boulder, Colorado USA 2006.

T P Murrells, N R Passant, G Thistlethwaite, A Wagner, Y Li, T Bush, et al. UK Emissions of Air Pollutants 1970 to 2008. UK Emissions Inventory Team August,2010.

Tai A, Val Martin M, Heald C. Threat to future global food security from climate change and ozone air pollution. Nature Climate Change 2014; 4: 817-821.

Tani A, Ohno T, Saito T, Ito S, Yonekura T, Miwa M. Effects of ozone on isoprene emission from two major Quercus species native to East Asia. Journal of Agricultural Meteorology 2017; 73: 195-202.

Tie X, Madronich S, Walters S, Zhang R, Rasch P, Collins W. Effect of clouds on photolysis and oxidants in the troposphere. Journal of Geophysical Research: Atmospheres 2003; 108.

Tsoar H. Bagnold, R.A. 1941: The physics of blown sand and desert dunes. London: Methuen. Progress in Physical Geography: Earth and Environment 1994; 18: 91-96.

Uma KN, Das SS, Ratnam MV, Suneeth KV. Assessment of vertical air motion among reanalyses and qualitative comparison with direct VHF radar measurements over the two tropical stations. Atmos. Chem. Phys. Discuss. 2020; 2020: 1-31

van der Werf GR, Randerson JT, Giglio L, Collatz GJ, Kasibhatla PS, Arellano Jr AF. Interannual variability in global biomass burning emissions from 1997 to 2004. Atmos. Chem. Phys. 2006; 6: 3423-3441.

van Stratum BJH, Vilà-Guerau de Arellano J, Ouwersloot HG, van den Dries K, van Laar TW, Martinez M, Lelieveld J, Diesch JM, Drewnick F, Fischer H, Hosaynali Beygi Z, Harder H, Regelin E, Sinha V, Adame JA, Sörgel M, Sander R, Bozem H, Song W, Williams J, Yassaa N. Case study of the diurnal variability of chemically active species with respect to boundary layer dynamics during DOMINO. Atmos. Chem. Phys. 2012; 12: 5329-5341.

Varshney CK, Singh AP. Isoprene emission from Indian trees. Journal of Geophysical Research: Atmospheres 2003; 108: n/a-n/a.

Velikova V, Fares S, Loreto F. Isoprene and nitric oxide reduce damages in leaves exposed to oxidative stress. Plant, Cell & Environment 2008; 31: 1882-1894.

Vickers CE, Possell M, Cojocariu CI, Velikova VB, Laothawornkitkul J, Annette R, et al. Isoprene synthesis protects transgenic tobacco plants from oxidative stress. Plant, Cell & Environment 2009; 32: 520-531.

Vlasenko A, Macdonald AM, Sjostedt SJ, Abbatt JPD. Formaldehyde measurements by Proton transfer reaction – Mass Spectrometry (PTR-MS): correction for humidity effects. Atmos. Meas. Tech. 2010; 3: 1055-1062.

Volodin EM, Dianskii NA, Gusev AV. Simulating present-day climate with the INMCM4.0 coupled model of the atmospheric and oceanic general circulations. Izvestiya, Atmospheric and Oceanic Physics 2010; 46: 414-431.

Wang Y, Bakker F, de Groot R, Wortche H, Leemans R. Effects of urban trees on local outdoor microclimate: synthesizing field measurements by numerical modelling. Urban Ecosystems 2015; 18: 1305-1331.

Wang YP, Lu XJ, Wright IJ, Dai YJ, Rayner PJ, Reich PB. Correlations among leaf traits provide a significant constraint on the estimate of global gross primary production. Geophysical Research Letters 2012; 39, L19405, doi:10.1029/2012GL053461.

Wagner A, Heinzeller D, Wagner S, Rummler T, Kunstmann H. Explicit Convection and Scale-Aware Cumulus Parameterizations: High-Resolution Simulations over Areas of Different Topography in Germany. Monthly Weather Review 2018; 146: 1925-1944.

Warneke C, Veres P, Holloway JS, Stutz J, Tsai C, Alvarez S, et al. Airborne formaldehyde measurements using PTR-MS: calibration, humidity dependence, inter-comparison and initial results. Atmos. Meas. Tech. 2011; 4: 2345-2358.

Watanabe S, Hajima T, Sudo K, Nagashima T, Takemura T, Okajima H, Nozawa T, Kawase H, Abe M, Yokohata T, Ise T, Sato H, Kato E, Takata K, Emori S, Kawamiya M. MIROC-ESM 2010: model description and basic results of CMIP5-20c3m experiments. Geosci. Model Dev. 2011; 4: 845-872.

Weerakoon W, Maruyama A, Ohba K. Impact of Humidity on Temperature-Induced Grain Sterility in Rice (Oryza sativa L). Journal of Agronomy and Crop Science 2008; 194: 135-140.

Went FW. Blue hazes in the atmosphere. ” Nature, 1960; 187, no. , pp. : 641–643.

Wesely ML. Parameterization of surface resistances to gaseous dry deposition in regional-scale numerical models. Atmospheric Environment (1967) 1989; 23: 1293-1304.

Wicker LJ, Skamarock WC. Time-Splitting Methods for Elastic Models Using Forward Time Schemes. Monthly Weather Review 2002; 130: 2088-2097.

Wiedinmyer C, Akagi SK, Yokelson RJ, Emmons LK, Al-Saadi JA, Orlando JJ, et al. The Fire INventory from NCAR (FINN): a high resolution global model to estimate the emissions from open burning. Geosci. Model Dev. 2011; 4: 625-641.

Williams J, Pöschl U, Crutzen PJ, Hansel A, Holzinger R, Warneke C, et al. An Atmospheric Chemistry Interpretation of Mass Scans Obtained from a Proton Transfer Mass Spectrometer Flown over the Tropical Rainforest of Surinam. Journal of Atmospheric Chemistry 2001; 38: 133-166.

Williams J, Warneck P. The Atmospheric Chemist´s Companion, 2012.

Winters AJ, Adams MA, Bleby TM, Rennenberg H, Steigner D, Steinbrecher R, et al. Emissions of isoprene, monoterpene and short-chained carbonyl compounds from Eucalyptus spp. in southern Australia. Atmospheric Environment 2009; 43: 3035-3043.

Wolfe GM, Kaiser J, Hanisco TF, Keutsch FN, de Gouw JA, Gilman JB, et al. Formaldehyde production from isoprene oxidation across NOx regimes. Atmos. Chem. Phys. 2016; 16: 2597-2610.

Wu T, Song L, Li W, Wang Z, Zhang H, Xin X, Zhang Y, Zhang L, Li J, Wu F, Liu Y, Zhang F, Shi X, Chu M, Zhang J, Fang Y, Wang F, Lu Y, Liu X, Wei M, Liu Q, Zhou W, Dong M, Zhao Q, Ji J, Li L, Zhou M. An overview of BCC climate system model development and application for climate change studies. Journal of Meteorological Research 2014; 28: 34-56.

Wu Z, Schwede DB, Vet R, Walker JT, Shaw M, Staebler R, et al. Evaluation and Intercomparison of Five North American Dry Deposition Algorithms at a Mixed Forest Site. Journal of Advances in Modeling Earth Systems 2018; 10: 1571-1586.

Xu C, McDowell NG, Fisher RA, Wei L, Sevanto S, Christoffersen BO, Weng E, Middleton RS. Increasing impacts of extreme droughts on vegetation productivity under climate change. Nature Climate Change 2019; 9: 948-953.

Xavier C, Rusanen A, Zhou P, Dean C, Pichelstorfer L, Roldin P, et al. Aerosol mass yields of selected biogenic volatile organic compounds – a theoretical study with nearly explicit gas-phase chemistry. Atmos. Chem. Phys. 2019; 19: 13741-13758.

Yáñez-Serrano AM, Nölscher AC, Williams J, Wolff S, Alves E, Martins GA, et al. Diel and seasonal changes of biogenic volatile organic compounds within and above an Amazonian rainforest. Atmos. Chem. Phys. 2015; 15: 3359-3378.

Yokelson RJ, Burling IR, Gilman JB, Warneke C, Stockwell CE, de Gouw J, et al. Coupling field and laboratory measurements to estimate the emission factors of identified and unidentified trace gases for prescribed fires. Atmos. Chem. Phys. 2013; 13: 89-116.

Yu L, Wang J, Clinton N, Xin Q, Zhong L, Chen Y, Gong P. FROM-GC: 30 m global cropland extent derived through multisource data integration. International Journal of Digital Earth 2013; 6: 521-533.

Yuan X, Wood EF, Luo L, Pan M. A first look at Climate Forecast System version 2 (CFSv2) for hydrological seasonal prediction. Geophysical Research Letters 2011; 38.

Yue X, Unger N. Ozone vegetation damage effects on gross primary productivity in the United States. Atmos. Chem. Phys. 2014; 14: 9137-9153.

Zannoni N, Dusanter S, Gros V, Sarda Esteve R, Michoud V, Sinha V, et al. Intercomparison of two comparative reactivity method instruments inf the Mediterranean basin during summer 2013. Atmos. Meas. Tech. 2015; 8: 3851-3865.

Zaveri RA, Peters LK. A new lumped structure photochemical mechanism for large-scale applications. Journal of Geophysical Research: Atmospheres 1999; 104: 30387-30415.

Zhang Y, Fu R, Yu H, Qian Y, Dickinson R, Silva Dias MAF, et al. Impact of biomass burning aerosol on the monsoon circulation transition over Amazonia. Geophysical Research Letters 2009; 36.

Zhou T, Wang B, Yu Y, Liu Y, Zheng W, Li L, Wu B, Lin P, Guo Z, Man W, Bao Q, Duan A, Liu H, Chen X, He B, Li J, Zou L, Wang X, Zhang L, Sun Y, Zhang W. The FGOALS climate system model as a modeling tool for supporting climate sciences: An overview. Earth and Planetary Physics 2018; 2: 276-291.

Zhu D, Peng SS, Ciais P, Viovy N, Druel A, Kageyama M, Krinner G, Peylin P, Ottlé C, Piao SL, Poulter B, Schepaschenko D, Shvidenko A. Improving the dynamics of Northern Hemisphere high-latitude vegetation in the ORCHIDEE ecosystem model. Geosci. Model Dev. 2015; 8: 2263-2283.

Zilitinkevich S. Non-local turbulent transport pollution dispersion aspects of coherent structure of convective flows , Air Pollution III, Air pollution theory and simulation. Computational Mechanics 1995; 1: 53-60 .

Zomer RJ, Neufeldt H, Xu J, Ahrends A, Bossio D, Trabucco A, van Noordwijk M, Wang M. Global Tree Cover and Biomass Carbon on Agricultural Land: The contribution of agroforestry to global and national carbon budgets. Sci Rep 2016; 6: 29987.

Appendix 1

WRF-Chem: Technical details

The schematic in Figure 1 shows the different sets of processes, data sets and programs involved in the WRF-Chem modeling system.

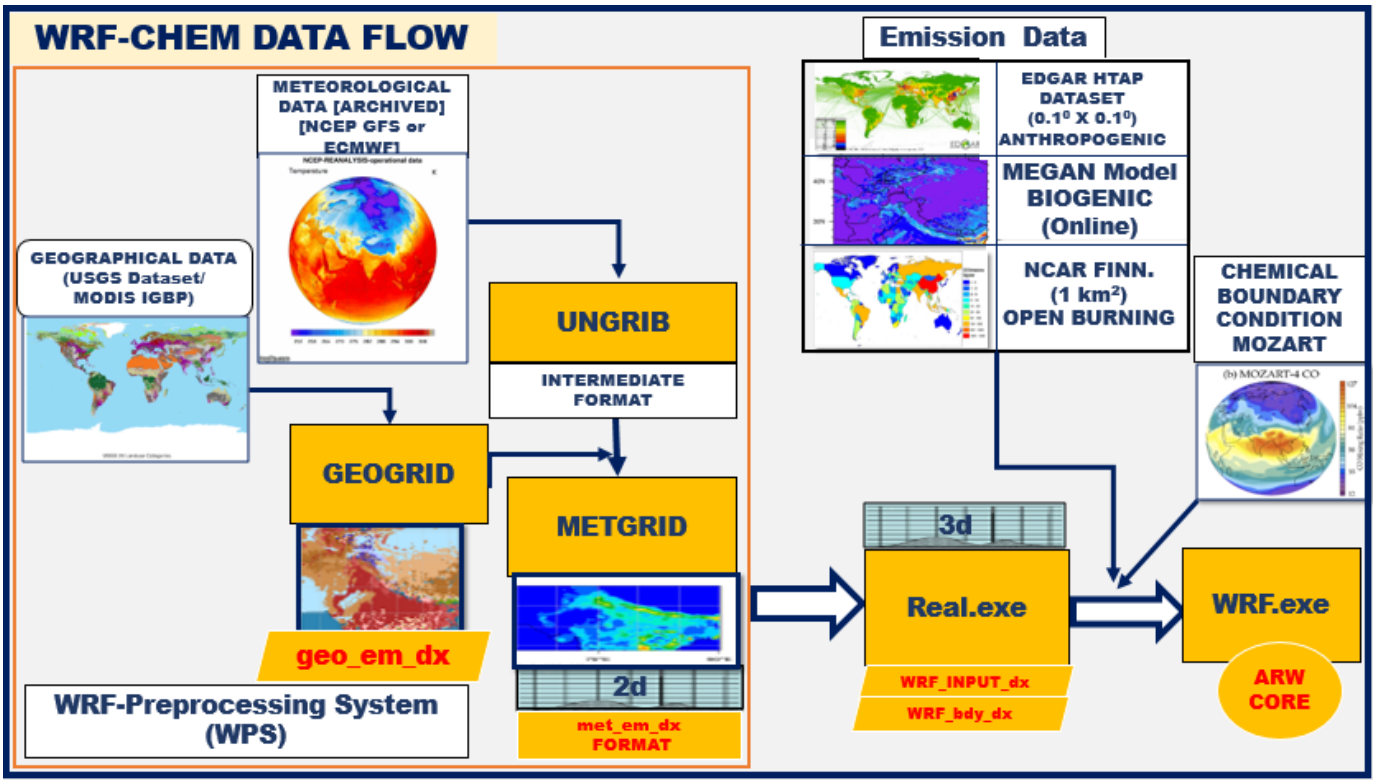

Figure 1 Schematic showing the data flow in WRF-Chem Model with its different components (Source: WRF-Chem model user guide).

The WRF pre-processing system

The first set of processes involves setting up the WRF pre-processing system which has the main objective to define the model domain it's latitudinal and longitudinal extent with the horizontal resolution, preparing the input land-use land surface data along with meteorological data for the next step. The schematic in Figure 2 shows the working of the WRF pre-processing system with the different programs and flow of data. The WPS is composed of three programs (1) Geogrid (2) Ungrib (3) Metgrid. All the three programs read parameters from the common Namelist.wps input file which has pre-defined sub-sections for each of the three above programs. The image in the

Figure 3 is displaying the Namelist.wps file used in this study with different components to control different programs in WRF pre-processing system (WPS).

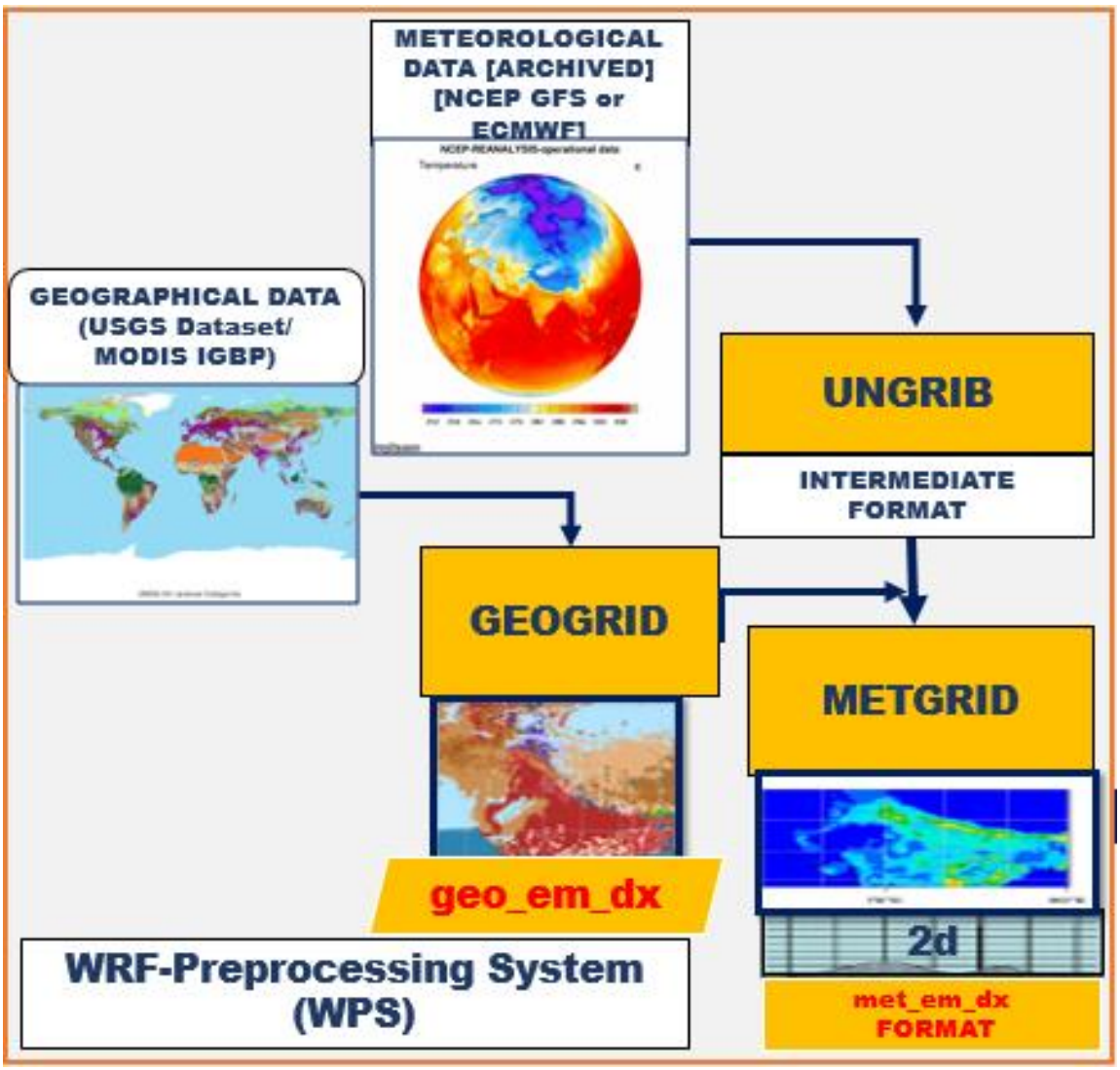

Figure 2 Schematic showing the data flow in WRF pre-processing System (WPS) (Source: WRF-Chem model user guide).

As discussed above in the schematic of WRF Pre-processing System the three main programs are controlled by the Namelist.wps file which has different parts. The first part of the Namelist.wps file defines the model core (wrf_core) in case of WRF-Chem the core used is ARW (Advanced WRF) as shown in Figure 3 which is followed by defining the number of domains that has to be set for the model simulation (max_dom) which in this study was set to 1, WRF model gives an option of setting up multiple domains with different set of resolutions to increase computational

efficiency, a technique called as nesting which will be discussed with an example later in this appendix. The next part of the Namelist.wps defines the start date and end date of the model simulation (start_date and end_date), followed by interval seconds which is the duration of global meteorological data and its time intervals (21600 seconds) as the global meteorological data used in this study (NCEP FNL dataset) is at a six hourly interval which is used as the boundary condition. The io_form_geogrid is the output format of the WRF data from Geogrid program where 2 stands for Netcdf format.

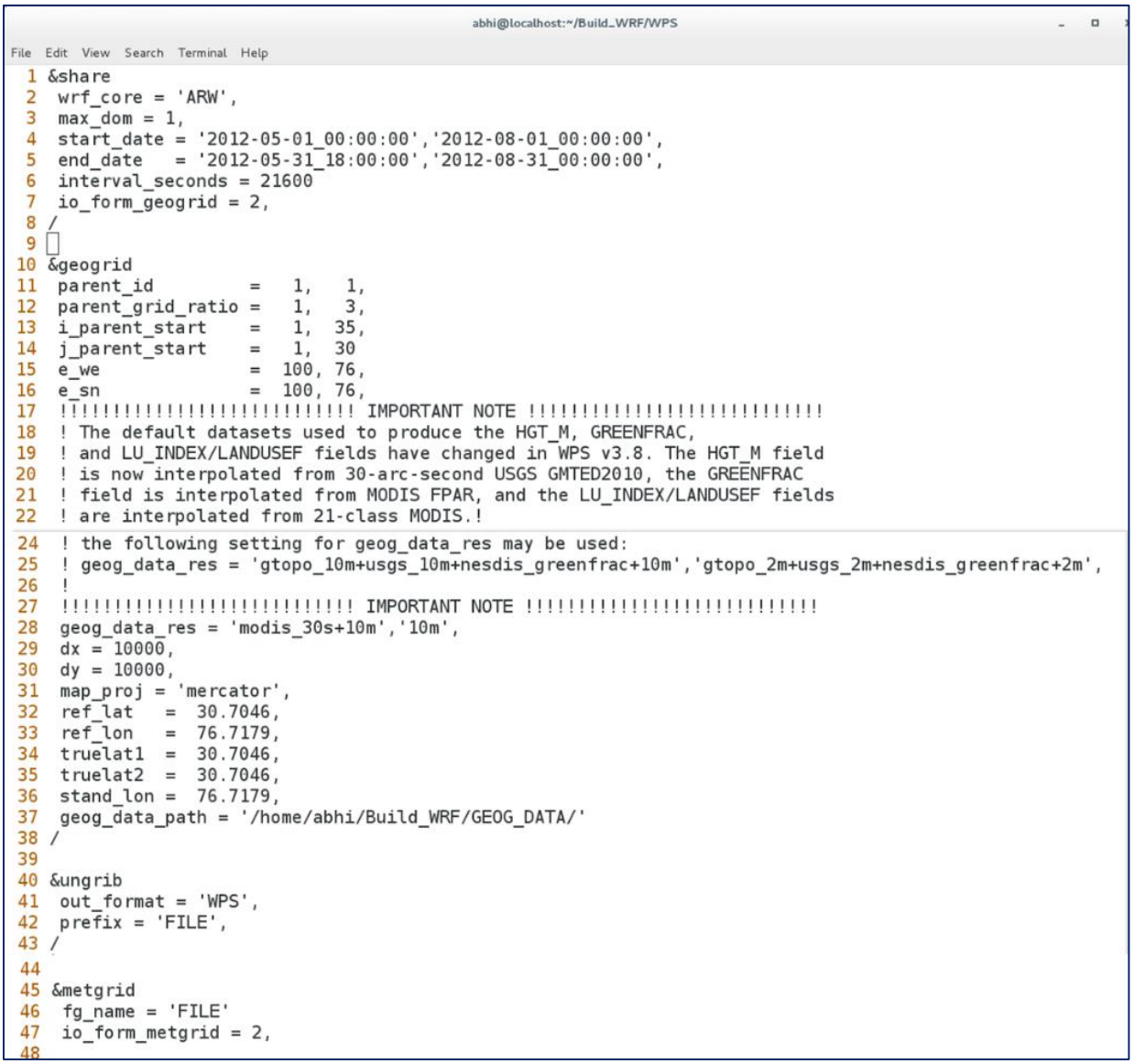

Figure 3 Image displaying the Namelist.wps file used in this study with different components to control different programs in WRF Pre-processing System (WPS).

The &geogrid part of the Namelist.wps part defines the modeling domain, parent_id, parent_grid_ratio, j_parent_start and j_parent_start is the respective id of that domain which is mainly used while nesting the model. The next two parameter e_we and e_sn define the number of grid points selected in east west and north-south direction. The other parameters which define the domain extent and properties are dx and dy which defines the required model horizontal resolution (10000 m / 10 km was the resolution set in this study), ref_lat and ref_lon defines where is the center of the model domain on earth's surface. After setting up the different parameters for the modeling domain under the geogrid program, static terrestrial data is mapped on the domain. The location of this data is defined in the parameter geog_data_path in the Namelist.wps file. In this study 20-category MODIS land-cover classification of the international geosphere-biosphere programme (Friedl et al., 2010) was used. Table 1 lists the different classes of land-use land cover classes used by MODIS land-cover classification in the current model setup.

Table 1 List of IGBP-Modified MODIS 20-category Land Use Categories.

Land Use Category	*Land Use Description*
1	Evergreen Needleleaf Forest
2	Evergreen Broadleaf Forest
3	Deciduous Needleleaf Forest
4	Deciduous Broadleaf Forest
5	Mixed Forests
6	Closed Shrublands
7	Open Shrublands
8	Woody Savannas
9	Savannas
10	Grasslands
11	Permanent Wetlands
12	Croplands
13	Urban and Built-Up
14	Cropland/Natural Vegetation Mosaic
15	Snow and Ice
16	Barren or Sparsely Vegetated
17	Water
18	Wooded Tundra
19	Mixed Tundra
20	Barren Tundra

The next program in the WRF pre-processing system after defining the modeling domain is ingestion of global meteorology data in the regional modeling domain. This begins with the Ungrib program where the gridded binary data (GRIB format) which is basically an output of some other global or regional model is accessed. In this study NCEP Final analysis (FNL) data from (GFS) global forecasting system at 1˚ spatial resolution and 6 hourly temporal resolution (https://rda.ucar.edu/datasets/ds083.2/) has been used for initialization of the model. The variable Table (Vtable.GFS) is used by the Ungrib program which enables the Ungrib program to extract

winds, temperature, humidity, surface pressure, sea level pressure, soil and landscape properties from the global dataset. The final step of the WRF Pre-processing System is running the Metgrid program in which all the interpolated terrestrial data and gridded meteorological dataset is combined in one output file followed by horizontal interpolation of the meteorological data into the modeling domain, it is worth noting that at this point all the data structure is 2-dimensional and is ready to be used by real data initialization program, which for WRF-Chem modeling is divided in two parts and will be discussed in the next sections.

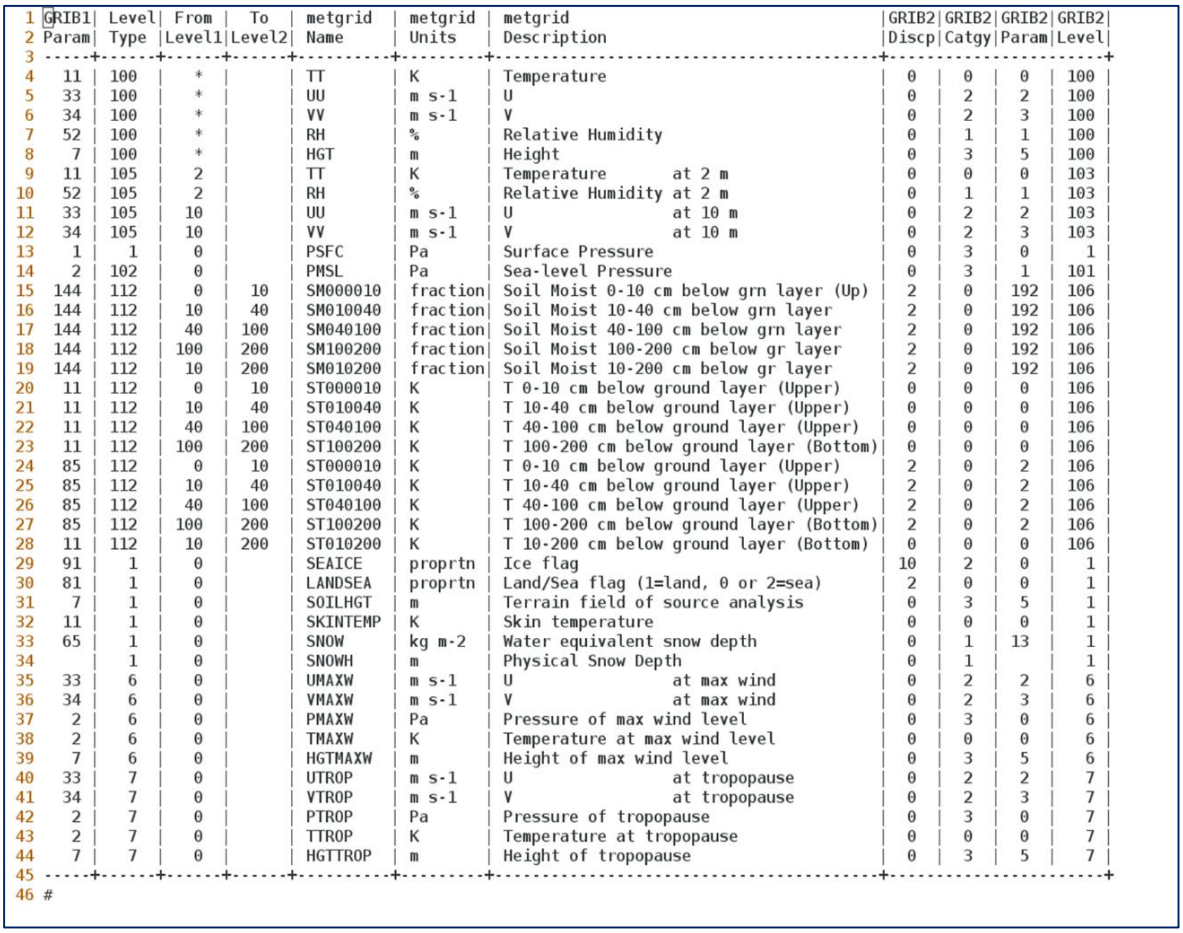

GRIB1 Param	Level Type	From Level1	To Level2	metgrid Name	metgrid Units	metgrid Description	GRIB2 Discp	GRIB2 Catgy	GRIB2 Param	GRIB2 Level
11	100	*		TT	K	Temperature	0	0	0	100
33	100	*		UU	m s-1	U	0	2	2	100
34	100	*		VV	m s-1	V	0	2	3	100
52	100	*		RH	%	Relative Humidity	0	1	1	100
7	100	*		HGT	m	Height	0	3	5	100
11	105	2		TT	K	Temperature at 2 m	0	0	0	103
52	105	2		RH	%	Relative Humidity at 2 m	0	1	1	103
33	105	10		UU	m s-1	U at 10 m	0	2	2	103
34	105	10		VV	m s-1	V at 10 m	0	2	3	103
1	1	0		PSFC	Pa	Surface Pressure	0	3	0	1
2	102	0		PMSL	Pa	Sea-level Pressure	0	3	1	101
144	112	0	10	SM000010	fraction	Soil Moist 0-10 cm below grn layer (Up)	2	0	192	106
144	112	10	40	SM010040	fraction	Soil Moist 10-40 cm below grn layer	2	0	192	106
144	112	40	100	SM040100	fraction	Soil Moist 40-100 cm below grn layer	2	0	192	106
144	112	100	200	SM100200	fraction	Soil Moist 100-200 cm below gr layer	2	0	192	106
144	112	10	200	SM010200	fraction	Soil Moist 10-200 cm below gr layer	2	0	192	106
11	112	0	10	ST000010	K	T 0-10 cm below ground layer (Upper)	0	0	0	106
11	112	10	40	ST010040	K	T 10-40 cm below ground layer (Upper)	0	0	0	106
11	112	40	100	ST040100	K	T 40-100 cm below ground layer (Upper)	0	0	0	106
11	112	100	200	ST100200	K	T 100-200 cm below ground layer (Bottom)	0	0	0	106
85	112	0	10	ST000010	K	T 0-10 cm below ground layer (Upper)	2	0	2	106
85	112	10	40	ST010040	K	T 10-40 cm below ground layer (Upper)	2	0	2	106
85	112	40	100	ST040100	K	T 40-100 cm below ground layer (Upper)	2	0	2	106
85	112	100	200	ST100200	K	T 100-200 cm below ground layer (Bottom)	2	0	2	106
11	112	10	200	ST010200	K	T 10-200 cm below ground layer (Bottom)	0	0	0	106
91	1	0		SEAICE	proprtn	Ice flag	10	2	0	1
81	1	0		LANDSEA	proprtn	Land/Sea flag (1=land, 0 or 2=sea)	2	0	0	1
7	1	0		SOILHGT	m	Terrain field of source analysis	0	3	5	1
11	1	0		SKINTEMP	K	Skin temperature	0	0	0	1
65	1	0		SNOW	kg m-2	Water equivalent snow depth	0	1	13	1
	1	0		SNOWH	m	Physical Snow Depth	0	1		1
33	6	0		UMAXW	m s-1	U at max wind	0	2	2	6
34	6	0		VMAXW	m s-1	V at max wind	0	2	3	6
2	6	0		PMAXW	Pa	Pressure of max wind level	0	3	0	6
2	6	0		TMAXW	K	Temperature at max wind level	0	0	0	6
7	6	0		HGTMAXW	m	Height of max wind level	0	3	5	6
33	7	0		UTROP	m s-1	U at tropopause	0	2	2	7
34	7	0		VTROP	m s-1	V at tropopause	0	2	3	7
2	7	0		PTROP	Pa	Pressure of tropopause	0	3	0	7
2	7	0		TTROP	K	Temperature at tropopause	0	0	0	7
7	7	0		HGTTROP	m	Height of tropopause	0	3	5	7

Figure 4 Image displaying the Vatable file used in this study with different variables which are mapped to the regional modeling domain in Ungrib program of the WRF pre-processing system (WPS).

Nesting the WRF model

Nesting is a process where a finer resolution model run can be embedded in a coarser resolution modeling domain and both the simulation domains can get simulated simultaneously as shown in Figure 5. The nested domain basically covers a part of the parent domain and is driven along the

lateral boundary conditions by the parent model. In WRF modeling system the daughter domain can give the feedback during the simulation back to the parent domain or it can be switched off as well. The main advantage of nesting the model is that a uniform high-resolution model domain would be computationally very expensive, so the higher resolution domain will cover only a portion of the parent model and will be therefore computationally less expensive. Additionally, most of the lateral boundary conditions of the model run is at a resolution of 1° and direct downscaling from 100 km to say about 3 km will also lead to downscaling of uncertainty apart from high computational cost. Main need of using the nesting option in the WRF model is to when one needs to study any localized phenomena such as convection, effect of topography on meteorology etc. or when the model input data is at a very coarse resolution (>10 times the fine resolution).

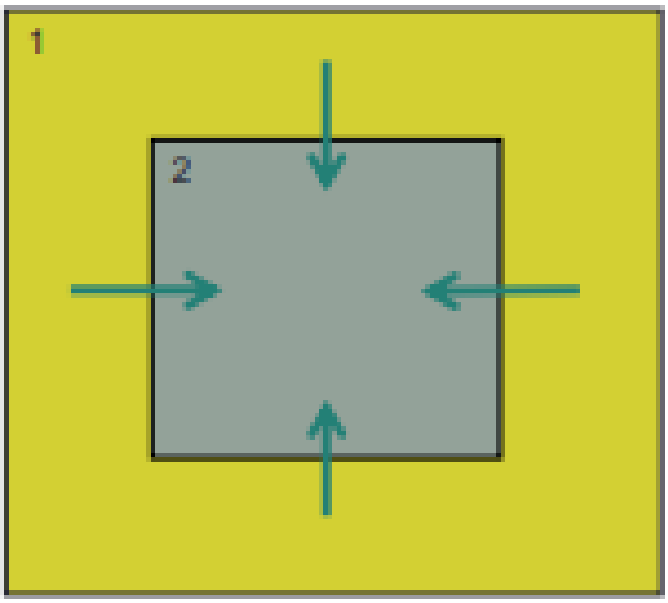

Figure 5 Conceptual Schematic of Model Nesting in WRF modeling setup (Adopted from WRF Training School 2019)-link (https://www2.mmm.ucar.edu/wrf/users/tutorial/201907)

The process of setting up the nesting modeling domain is controlled by the Namelist.wps file which controls the dimension and location of the modeling domain. The main parameters which control the nesting dimensions and are shown in the Figure 6, parent_id represents the domain number of the parent of that particular domain (=1 on second column), parent grid ratio is recommended to be 1:3 or 1:5 for ensuring numerical stability (Skamarock et al., 2008). The i parent and j parent

represent the location of the daughter domain inside the parent domain by defining its location as a Cartesian coordinate system.

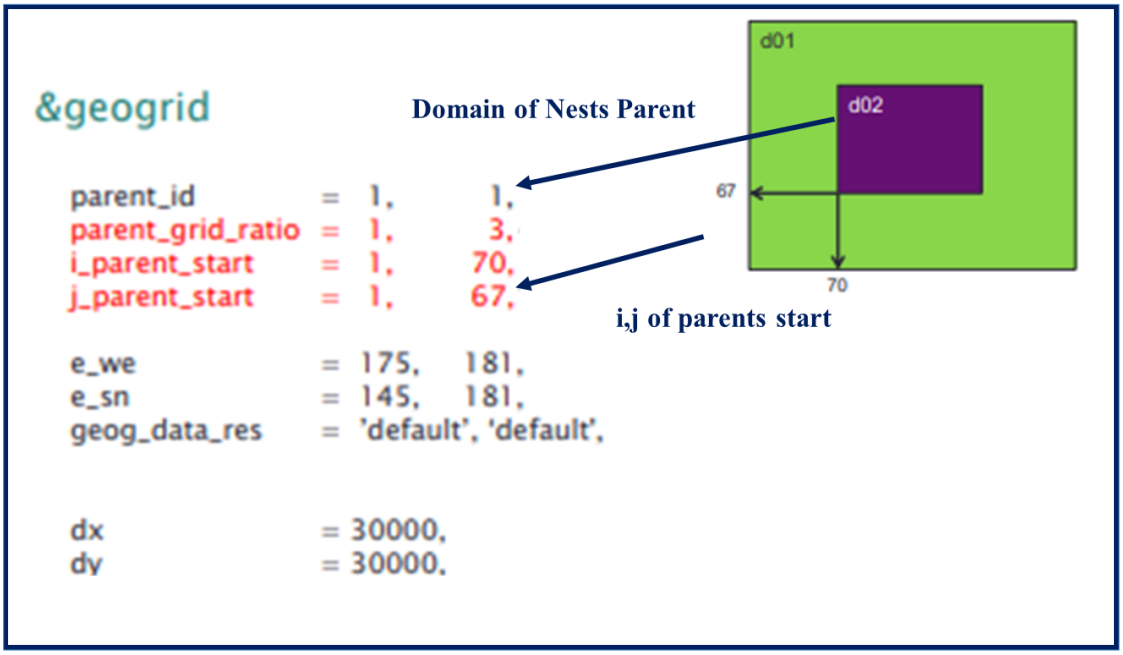

Figure 6 Image displaying a nested modeling namelist test case with details of parameters ((Adopted from WRF Training School 2019)-link (https://www2.mmm.ucar.edu/wrf/users/tutorial/201907)).